Electronic and electrical properties of organic semiconductor/metal nanoparticles structures

Dissertation

zur Erlangung des akademischen Grades
doctor rerum naturalium (Dr. rer. nat.) im Fach Physik

eingereicht an der

Mathematisch-Naturwissenschaftlichen Fakultät
Humboldt-Universität zu Berlin

von

Herrn Dipl.-Phys. Giovanni Ligorio

Präsident der Humboldt-Universität zu Berlin:
Prof. Dr. Jan-Hendrik Olbertz
Dekan der Mathematisch-Naturwissenschaftlichen Fakultät:
Prof. Dr. Elmar Kulke

Gutachter:
1. Prof. Dr. Norbert Koch
2. Prof. Dr. Mats Fahlman
3. Prof. Dr. Alessio Gagliardi

Tag der mündlichen Prüfung: 11.01.2016

Affidavit

I declare that I have authored this thesis independently, that I have not used other sources/resources than the declared once, and that I have explicitly indicated all material which has been quoted either literally or by content from the sources used.

German version:
Ich erkläre an Eides statt, dass ich die vorliegende Arbeit selbstständig verfasst, andere als die angegebenen Quellen/Hilfsmittel nicht benutzt, und die den benutzen Quellen wörtlich und inhaltlich entnommenen Stellen als solche kenntlich gemacht habe.

Berlin - July 31, 2015

Table of contents

List of abbreviations and acronyms

Miscellaneous:

AO	atomic orbital
AuNPs-device	device with embedded AuNPs
DOS	density of states
EA	electron affinity
E_{gap}	optical gap
EIB	electron injection barrier
ε_0	dielectric constant of vacuum
ε_r	relative dielectric constant
GDM	Gaussian disorder model
HIB	hole injection barrier
HOMO	highest occupied molecular orbital
HRS	high resistance state
IE	ionization energy
ILC	injection limited current
IMFP	inelastic mean free path
J	current density
LRS	low resistance state
LUMO	lowest unoccupied molecular orbital
MNP	metal nanoparticle

MO	molecular orbital
NDR	negative differential resistence
NVM	non-volatile memory
R-NVM	resistance non-volatile memory
Ref-device	device without embedded AuNPs
SCLC	space charge limited current
U	applied bias
UHV	ultra-high vacuum
VL	vacuum level

Experimental techniques:

AFM	atomic force microscopy
C-AFM	conductive atomic force microscopy
GLAD	glancing angle deposition
I-U	current vs. voltage
J-U	current density vs. voltage
PES	photoelectron spectroscopy
SEM	scanning electron microscopy
TEM	transmission electron microscopy
UHV	ultra-high vacuum
UPS	ultraviolet photoelectron spectroscopy
UV-VIS	ultraviolet-visible spectroscopy
XPS	X-Ray photoelectron spectroscopy

Materials:

α-NPD	4,4-bis[N-(1-naphthyl)-N-phenyl-amino]diphenyl
AuNP/AgNP	gold nanoparticle/silver nanoparticle
Alq_3	tris(8-hydroxyquinolinato)aluminum
AuNP	gold nanoparticle
ITO	indium tin oxide
MoO_3	molybdenum trioxide
PEDOT:PSS	poly(3,4-ethylenedioxy-thiophene):poly(styrenesulphonic acid)

Abstract

The increasing need to store digital information triggers the exploration of new materials for future non-volatile memory (NVM) technologies. For instance, metal nanoparticles (MNPs) embedded into organic semiconductors (conjugated small molecules or polymers) are suitable for memory applications because they were found to display bistable resistive switching. This means, that these devices can be set either to a low conductive state (associated to the logical "0") and a high conductive state (associated to the logical "1") upon electrical conditioning. Different switching models were hitherto developed to explain the fundamental mechanisms at work in resistive NVMs.

Despite intense academic activities in the field of organic NVMs, a consistent rationale for the resistive switching is still missing; mainly, two models have been suggested as explanations. One proposed mechanism is related to the formation/rupture of conductive paths (i.e. filaments) within the device, hence bridging the contacts. The second proposed mechanism is governed by a space-charge field. The current through the device is controlled by the charging/decharging of the embedded MNPs.

The present work explores specifically the role of this space-charge field due to charged MNPs in two-terminal unipolar devices in which the formation of a filament can be excluded. A series of experiments on the electronic and electrical properties of devices were conducted in order to reveal, whether the mechanism based on the space charge field is, indeed, at play in resistance switching.

X-ray and ultraviolet photoelectron spectroscopy provided detailed information about the interaction between gold nanoparticles (AuNPs) and two prototypical organic semiconductors used in optoelectronics, 4,4-bis[N-(1-naphthyl)-N-phenyl-amino]diphenyl (α-NPD) and tris-(8-hydroxyquinoline)-aluminum (Alq_3). In contrast to the organic semiconductor-on-Au systems where only physisorption is observed, the AuNPs-on-organic semiconductor systems exhibit strong chemisorptive character, resulting in the formation of organometallic complexes. The study of the electronic valence structures provided evidence of a space-charge field due to the AuNPs charging (induced by photoemission). Furthermore, it is found that upon illumination with appropriate light AuNPs'charge-neutrality can be dynamically re-established, through electron transfer from excitons.

Devices were built with the same materials investigated by photoemission spectroscopy, and electrical characterization was conducted. Despite the previously demonstrated

ability to optically change the charging state of the AuNPs, the devices (if filament formation can be suppresed) do not display any bistability.This finding provides evidence that the commonly proposed MNPs charging/decharging mechanism can be excluded as cause for electrical bistability in two-terminal devices. Thus, alternative mechanisms such as filament formation must be invoked instead.

In order to explore the scaling of resistive NVMs into the nanometric range, glancing angle deposition technique was employed. The nano-NVMs were electrically characterized and it is proved to manifest resistive bistability, which is explained by filament formation/destruction. Accordingly, these nano-NVMs are appealing as future high-density memory technology.

Kurzfassung

Der zunehmende Bedarf an digitalen Speichermedien macht die Erforschung von neuen Materialien für zukünftige Technologien von persistenten Speichern nötig. Hierfür eignen sich zum Beispiel Metall-Nanopartikeln, die in organischen Halbleiterschichten (konjugierte kleine Moleküle oder Polymere) eingebettet sind. Auf Grund der bistabilen Schaltbarkeit der Leitfähigkeit von Metall-Nanopartikeln lassen sie sich in Abhängigkeit der elektrischen Umgebungsbedingungen entweder in einen niedrig leitenden Zustand (der „0“ Zustand) oder einen hoch leitenden Zustand (der „1“ Zustand) schalten. Bisher wurden verschiedene Modelle entwickelt, um den Schaltmechanismus von Speichern mit einem organischen Matrixmaterial zu erklären, jedoch fehlt bislang ein konsistentes Bild zum Verständnis des Schaltvorgangs. Im Wesentlichen werden bisher zwei Modelle vorgeschlagen: Eine Erklärung basiert auf der Ausbildung bzw. dem Zerreißen von leitenden Pfaden (sogenannten Filamenten) innerhalb des Bauelements, die als überbrückende Kontakte fungieren. Der zweite vorgeschlagene Mechanismus wird durch ein sogenanntes Raumladungsfeld bestimmt. Dabei wird der Strom innerhalb des Bauteils durch das Aufladen bzw. Entladen der eingebetteten Metall-Nanopartikeln kontrolliert.

Die vorliegende Arbeit untersucht die Rolle des Raumladungsfeldes ausgehend von Metall-Nanopartikeln in zweipoligen unipolaren Bauelementen, in denen die Ausbildung von Filamenten ausgeschlossen werden kann. Dazu wurde eine Reihe von Experimenten zur Bestimmung der elektronischen und elektrischen Eigenschaften durchgeführt, um die tatsächliche Rolle des Raumladungsfeldes aufzuklären.

Mit Hilfe von Röntgen- und Ultravioletter Photoelektronenspektroskopie wurde die Wechselwirkung zwischen den Gold-Nanopartikeln und den prototypischen organischen Halbleitern 4,4-Bis[N-(1-naphthyl)-N-phenyl-amino]diphenyl (α-NPD) und Tris-(8-hydroxyquinoline)-aluminium (Alq_3) detailliert untersucht. Im Gegensatz zur Situation eines organischen Halbleiters auf einem Goldsubstrat, bei der ausschließlich Physisorption beobachtet wurde, weist das System „Gold-Nanopartikel auf einer organischem Halbleiterschicht“ einen starken chemisorptiven Charakter auf, der zur Bildung von organometallischen Komplexen führt. Zusätzlich bewies die Untersuchung

der elektronischen Struktur die Existenz eines Raumladungsfeldes, das von den (durch Photoemission) geladenen Gold-Nanopartikeln erzeugt wurde. Weiterhin konnte der Zustand von Ladungsneutralität im Film durch einen lichtinduzierten Elektrontransfer von Excitonen wiederhergestellt werden.

Unter Verwendung der bereits photoelektronenspektroskopisch untersuchten Materialien wurden Bauelemente hergestellt und elektrisch charakterisiert. Trotz der bereits gezeigten Möglichkeit, den Ladungszustand der Gold-Nanopartikeln auch unter Ausschluss des Filament-Bildungsmechanismus lichtinduziert zu verändern, wiesen die Bauteile keine Bistabilität auf. Dieses Ergebnis zeigt, dass der allgemein vorgeschlagene Mechanismus bezüglich der Aufladung bzw. Entladung von Metall-Nanopartikeln als Ursache für die elektrische Bistabiliät in einem zweipoligen Bauteil ausgeschlossen werden kann. Stattdessen stützt dieses Ergebnis den alternativen Mechanismus der Filamentbildung.

Zur Untersuchung der Skalierbarkeit der permanenten ohm'schen Speicher im Nanometerbereich, wurden die Strukturen durch das Abscheiden der Materialien bei streifendem Einfall (GLAD) präpariert. Die entsprechenden Nano-Speicher wurden elektrisch charakterisiert und zeigten Bistabilität, was auch hier durch die Ausbildung bzw. Zerstörung von Filamenten erklärt wurde. Folglich sind diese Nano-Speicher besonders attraktiv für zukünftige Technologien in Hinblick auf hohe Speicherdichten.

Introduction

The perpetual need to preserve traces of identity and knowledge has driven humankind to search for external support for the storage of information. The human ability to store ideas and concepts by means of representation has led to the development of suitable data storage devices. Several technological revolutions have guided the evolution of writing through history since its invention: beginning with inscriptions on rock or cave walls, then substituted for wood or clay tablets, later developed into papyrus, parchment, and paper, and now electronically-represented bits of information.

Modern data storage devices are realized electronically and are based on the ability to change one physical property between two unambiguous metastable states, which are related to the logical “0” or “1”. Depending on the nature of the bistability, memory devices can be divided into categories, as the scheme in Figure 1 shows. The primary categorical distinction can be carried out according to the volatility of the stored information. Memory storage devices are referred to as volatile memories if the intrinsic data endurance is short, i.e. if the device requires an external power source to maintain data information. Typical examples of volatile memories include random-access memory (RAM). RAM devices allow data to be read and written in roughly the same amount of time, regardless of the order in which they are accessed. In contrast, non-volatile memories (NMVs) can retain stored information even if non-powered. The drawback of this data-storing endurance is, however, the access time: NVMs (like hard disks or flash memorys) are orders of magnitude slower than RAMs [1,2].

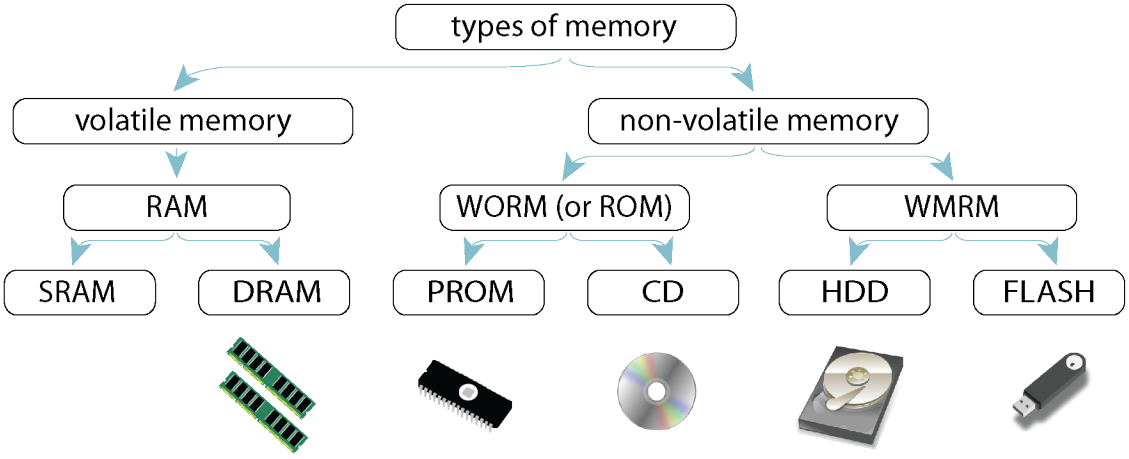

Figure 1. Classification of electronic memory technologies according to volatility and reset ability.

NVM can be categorized according to its reset possibility and is thus divided into write-once read-many (WORM, or simply read-only memory, ROM) and write-many read-many (WMRM). WORMs are used to permanently hold information for future readout, and are therefore used for databases (e.g. CD, DVD, PROM, or electronic labels).

Nowadays, electronic consumer devices are based on WMRM. The specific need required (such as portability, quantity of information, writing/reading speed) primarily determines the choice of technological support. Hard-disk drives (HDDs, based on magnetizing a thin film of ferromagnetic material on a disk), for instance, allow for the storage of a substantial amount of information with a good cost/information-volume ratio. Flash memories have faster data-access times due to their electric programmability with respect to HDDs; however, because the technology is based on metal-oxide-semiconductor field-effect transistors, the cost/information-volume ratio is higher. A schematic of costs per GB vs. data-access time for common consumer devices (such as memory RAM[1], solid-state disk[2], flash USB stick[3], HDD[4])[5] is depicted in Figure 2.a.

[1] Memory RAM - Corsair 8GB (2x 4GB) 1333mhz, 58.99 $.
[2] SSD - Samsung 850 EVO 250GB, 98.99 $.
[3] Flash USB stick - SanDisk Cruzer CZ36 32GB, 14.99 $.
[4] HDD - Western Digital WD10EZEX Blue 1TB, 59.89 $.
[5] Each device considered in this qualitative analysis is the “best seller” for the relative category on www.amazon.com (updated at Mai 2015). Prices from the same website.

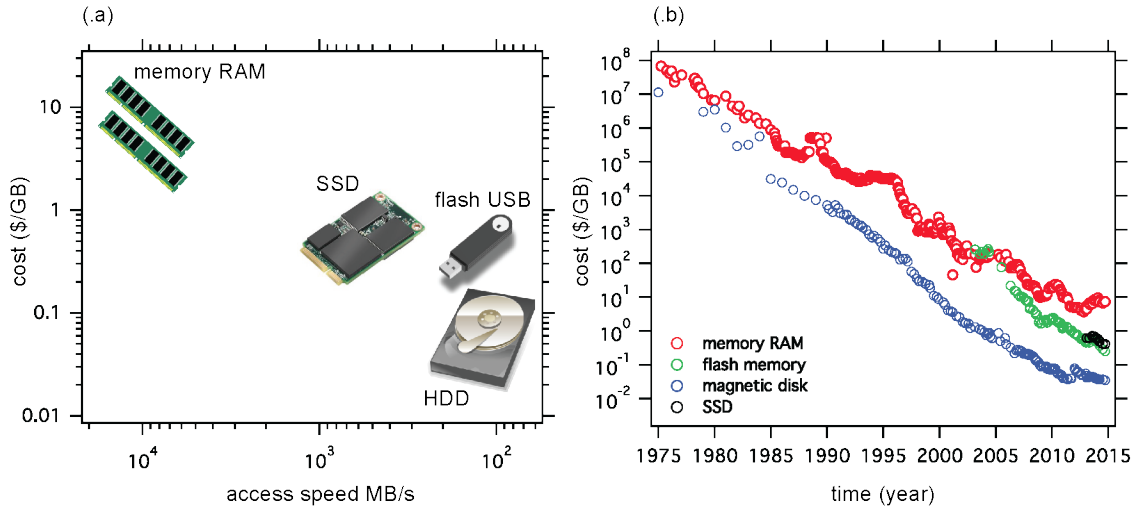

Figure 2. Costs per GB of common consumer devices versus their data-access speed time in (.a). Time evolution of the costs of different memory technologies in (.b).

The graph in Figure 2.b portrays the evolution of computer-memory technology costs with time (original data taken from Ref. [3], modified and updated). Computer storage has experienced a tremendous phase of development over the last fifty years.

As new technology has been brought to the market, prices (as well as the size for a single bit) have continued to decline steadily on a logarithmic scale, as shown in the graph. This evolution is consistent with the empirical law named after (IBM co-founder) Gordon Moore, which observes "*The number of transistors incorporated in a chip will approximately double every 24 months*" [4]. As a corollary, Moore's law forecasts that computing power will dramatically increase – and decrease in relative cost – at an exponential rate. On the other hand, technological improvement faces physical limitations in downscaling, and thus researchers are continuously confronted with the challenge of overcoming such restraints to innovation [5].

This hindrance to information storage has triggered periodic technological revolutions and new materials. The consequent adoption of new memory storage devices permits price reduction (as depicted in the graph in Figure 2.b) and improvement in parameter such as data access time, and information density.

Within the different classes of materials in solid-state physics, organic semiconductors continue to increase their appeal for science and technology. These materials are formed by the aggregation of π–conjugated organic molecules or polymers. Because the possibility to chemically synthesize carbon compounds, and thus *ad hoc* tailor the molecular properties [6,7], the applications in opto-electronics for these materials are

practically unlimited. Organic semiconductors have been extensively studied throughout the past decades and are presently successfully employed in many electronic devices. High-efficiency, very bright, and thin displays based on organic light-emitting devices (OLEDs) have become available for commercial purposes [8,9]. There is also considerable improvement in organic field-effect transistors (OFETs) [10–12] and organic photovoltaic (OPV) devices for low-cost solar energy generation [13,14].

Conjugated organic molecules and conjugated polymers are also promising candidates for future applications of molecular-scale organic NVMs [1,15–18]. In particular, their attractive properties include low-cost fabrication, simplicity in the structure of the device itself, high scalability, low-power operation, multi-layer staking, and large data capacity [17,19–22]. Furthermore, due to their physical properties organic materials are compatible with flexible substrates [23,24], allowing to include memory in flexible logic circuits.

Among the different typology of organic NVMs, resistive switching devices (R-NVMs) are promising for their structure and simple processability [25]. Typical structures of such resistive switching devices are hybrid structures, i.e. metal nanoparticles (MNPs) embedded in an organic layer between two electrodes [15,18]. The act of switching between the high resistance state (HRS) and the low resistance state (LRS) is usually achieved by an electrical stimulus with a specific threshold. The resistance state can be (non-destructively) read by applying a bias below the threshold, and the device does not need electrical power to be maintained in its ON state [16,26–28].

The bistable switching behavior has been observed for a wide range of material combinations (small molecules and polymers, electrodes, NP-metals) and structures; nevertheless, the underlying switching mechanism still remains unclear. In R-NVMs, two different switching mechanisms have been proposed. One reported mechanism highlights the role of a space-charge field, controlling the current flowing in the device [15,29–31]. It has been speculated that switching between conductive states is due to a Coulomb-blockade, related to the charging/decharging of the embedded MNPs under the applied bias [29,30]. A second reported fundamental mechanism is based on filamentary formation/destruction [32,33]. The electrical switching is explained by the formation of highly conductive localized paths (filaments) within the organics. The shortening between the electrodes sets the device into a LRS (or high conductance

state); the rupture of the conductive filament sets the device into a HRS (or low conductance state) [34,35]. Curiously, however, devices with analogous electrical characteristics are typically explained by both (mutually exclusive) switching models.
With the aim of resolving key issues in the fundamental physics of R-NVMs and in order to realize new hybrid organic/inorganic devices, the project HYMEC (short for "Hybrid organic/inorganic Memory elements for integration of Electronic and photonic Circuitry") was launched in 2011 within the FP7-NMP framework research program. Over the project duration of 36 months, the cooperative efforts of nine (academic and non-profit research company) partners[6] have been assembled.

My research has been conducted within the HYMEC project and deals with controlling and understanding the hybrid organic/inorganic hybrid systems. In particular, I tried to rationalize the Coulomb-blockade and the role of metal nanoparticles embedded into conjugated organic materials, in order to address whether *MNPs' charging state is at play in the resistive switching that occurs in actual devices*, as frequently reported in literature [29–31,36,37].
Despite a lack of solid evidence, many authors explain the switching behavior of unipolar R-NVMs by supposing charging/discharging of (above mentioned) nanoparticles-induced space-charge field. In order to investigate this issue, a series of experiments were performed to test the validity of this hypothesis.
The deposition of metal nanoparticles was experimentally performed via direct thermal evaporation of the metal on amorphous organic semiconductor films. X-ray photoemission spectroscopy was employed to compare the different chemical interactions arising at the nanoparticles/molecule interface with respect to the ones at the molecule/metal interface [38].[7]
The electronic structure of the nanoparticles/molecule interface was further investigated via ultraviolet photoemission spectroscopy. It was discovered that, due to photoelectron emission, the positively-charged metal nanoparticles induce space-charge at the interface. Upon illumination with light that could be absorbed by the

[6] Humboldt University of Berlin (Germany), University of Namur (Belgium), University of Cagliari (Italy), University of Tor Vergata (Italy), University of Tübingen (Germany), University of Lodzki (Poland), French national Centre for Scientific Research (Strasbourg, France), Nanotech Center Weiz (Austria), TechOnYou s.r.l. (Cagliari, Italy).
[7] These results are reported in Chapter 4.

organic semiconductors, dynamic charge neutrality of the nanoparticles could be induced through exciton-mediated electron transfer [39].[8]

The know-how acquired in nanoparticle deposition and the novel optical approach to remove space-charge at the hybrid/interface was accordingly employed for devices (with nanoparticles embedded in organic semiconductor) in order to verify the validity of the space-charge field model as the fundamental switching mechanism in R-NVMs. The appropriate materials choice for the electrical contacts (inert materials not subject to ion mass transport) and the careful preconditioning of the devices exclude the formation of metallic filaments. Despite the ability to optically control the charge state of the embedded nanoparticles by means of absorbed light, the devices did not display any bistability [40].[9]

These results provide evidence that the *commonly proposed charging/decharging mechanism can be readily excluded as the fundamental mechanism in unipolar R-NVMs,* and, therefore, alternative mechanisms need to be considered as reasons for bistability. The electronic behavior of these devices (with inert electrodes to avoid filament formation) has been compared with the one of an equivalent device fabricated with electrochemical active metal (Al) as top contact (filament formation is therefore allowed) [41–43]. It was found that the device with Al-electrode (even if the device was fabricated without NPs) displays resistive switching upon proper polarization. Complementing these results, the HYMEC partner Nanotech Center Weiz recently reported on the comparison between prototypical devices, with and without metal nanoparticles [42]. Regardless of the presence of metal nanoparticles, both devices displayed the same current-bias characteristic curves, typical for unipolar R-NVMs. These devices were studied with impedance spectroscopy, showing that their behavior in the LRS (when conductivity is high) is resistive rather than capacitive. This indicates that the formation/rupture of a high conductive path, indeed, most likely represents the mechanism for bistability.

In order to explore the miniaturization of R-NVM devices into the nanometric scale, glancing-angle deposition technique was used for the production of nanomemory elements.[10] The nanoscaled R-NVMs have been electrically characterized with

[8] These results are reported in Chapter 5.
[9] These results are reported in Chapter 6.
[10] These results are presented in Chapter 7.

conductive scanning force microscopy. The ability to set pristine devices (as *it-is* in low conductive state) in high conductive state provides evidences that the working principle based on filament formation/destruction works in the nanoscale. These findings make hybrid R-NVMs highly appealing as future high-density memory technology.

Chapter 1. Fundamentals and background

In this chapter the basic principles of conjugated organic systems and their application within electronic devices will be introduced. Their electronic properties will be overviewed, in particular at the contact with electrodes. The understanding of the electronic structure will be useful to illustrate the electric transport in amorphous films based on the conjugated systems. Finally, memory devices based on these materials, as well as their working principles, will be discussed.

1.1. Organic semiconductors

1.1.1. Electronic structure of organic semiconductor molecules

Organic semiconductors are carbon-based *conjugated* molecules, i.e. systems in which alternating single and double bonds are present between the C atom chains forming the backbone of the molecule. There are two major classes of organic semiconductors: low weight *molecules* and *polymers*. Typical examples of such a chemical configuration are benzene and polyacetylene shown in Figure 1.1.a and Figure 1.1.e.

As known from molecular orbital theory, it is possible to distinguish between two different kinds of molecular bonds:

- σ-*bond* resulting from the accumulation of electron density in regions where atomic orbitals overlap. The overlap may interfere constructively or destructively giving rise to bonding (σ) or anti-bonding (σ*) states.
- π-*bond*, where the overlap of atomic orbitals does not occur between the nuclei but broadside-on instead. This overlap yields bonding (π) or anti-bonding (π*)

states as well. π-orbitals are bound less strongly than σ-orbitals, because their maximum overlap occurs off-axis [44].

A carbon atom has four valence electrons, thus its electronic configuration corresponds to $1s^2\ 2s^2\ 2p^2$ ($1s^{\uparrow\downarrow}\ 2s^{\uparrow\downarrow}\ 2p_x^{\uparrow}\ 2p_y^{\uparrow}\ 2p_z$). In conjugated systems, each C atom has 3 neighbors, with which it forms 3 equivalent coplanar σ-bonds, arising from the overlap of the sp^2 hybridized electron orbitals of two adjacent C atoms (hybridization between electron orbitals 2s, $2p_x$ and $2p_y$, resulting in the electrical configuration $1s^{\uparrow\downarrow}\ 2sp^{2\uparrow}\ 2sp^{2\uparrow}\ 2sp^{2\uparrow}\ 2p_z^{\uparrow}$; see Figure 1.1.b and .f.

The 4th valence orbital ($2p_z$) lies perpendicular to the plane of the sp^2 hybridization. In conjugated systems, the $2p_z$ orbitals' overlap can be extended over all C atoms, which form the backbone of the molecule; therefore, this overlap leads to the formation of a molecular, delocalized π-electron orbital (see Figure 1.1.c and .d see Figure 1.1.g and .h) [45].

A molecule in the ground state has all the bonding orbitals filled with electrons, while the antibonding orbitals are empty. Thus, the *highest occupied molecular orbital* (HOMO) is the π-orbital, while π*-orbital represents the *lowest unoccupied molecular orbital* (LUMO). These two orbitals form the frontier orbitals of the organic semiconductor molecules and are the key to understanding physical characteristics such as electronic and optical properties.

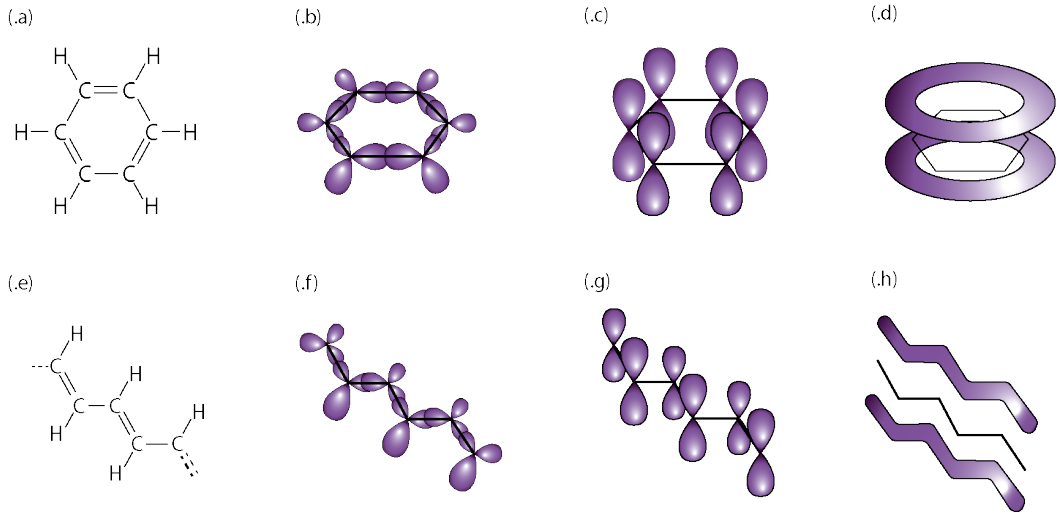

Figure 1.1. Schematic drawing of chemical structure of benzene in (.a) and polyacetylene in (.e). σ-bonds with hybridized sp^2 in (.b) and (.f), respectively. $2p_z$ orbitals in (.e) and (.g). Delocalized π-orbitals in the two conjugated systems in (.d) and (.h).

Excitation processes, i.e. light absorption by a molecule, can induce electron promotion from the HOMO level to the LUMO level (leaving a hole in the HOMO), with consequent formation of *neutral excited states*.

For this reason, the energy difference between HOMO and LUMO is indicated as an *optical gap* (E_{gap}). The π-π* transition is the lowest electronic excitation in conjugated molecules with an E_{gap} typically in the range of 1.5 eV – 3.0 eV, therefore leading to absorption in the light visible range [46].

Organic molecules present a relatively low dielectric constant ($\varepsilon_{\mathrm{r}} \approx 3$), thus Coulomb attraction between the optical promoted electron in the LUMO and hole left in the HOMO is strong (hundreds of meV, much larger than thermal energy at room temperature, $k_{\mathrm{B}}\mathrm{T}$ = 26 meV). This leads to the formation of an electron-hole bound pair called *exciton,* localized on the molecule.

The energy difference from the HOMO or the LUMO to the vacuum level (VL, defined as the energy of an electron at rest that is needed to escape the molecule), are the *ionization energy* (IE) or the *electron affinity* (EA), respectively. Summarizing the definition given above:

$$E_{\mathrm{gap}} = E_{\mathrm{LUMO}} - E_{\mathrm{HOMO}}; \qquad \text{(Eq. 1.1)}$$

$$\mathrm{IE} = E_{\mathrm{HOMO}} - \mathrm{VL}; \qquad \text{(Eq. 1.2)}$$

$$\mathrm{EA} = E_{\mathrm{LUMO}} - \mathrm{VL}. \qquad \text{(Eq. 1.3)}$$

1.1.2. From molecules to solids

Conjugated molecular systems and conjugated polymers can be brought together to form molecular solids. The characteristics of the organic solid depend on the nature of the single molecule forming the solid, as well as on the intermolecular interactions.

In the following section, an overview of the electronic structure evolution from a single atom to an organic solid will be schematically reviewed.

Figure 1.2.a depicts the potential well of a hydrogen-like atom, which originates from its Coulomb potential (the ordinate is the electron energy). The well forms atomic orbitals (AOs), and electrons fill them, starting from the one with the lowest energy (1s). The horizontal line of the schematic corresponds to the vacuum level (VL), at which energy electrons can escape the atom. Figure 1.2.b shows the electronic structure of a polyatomic molecule (made by 3 atoms). The effective potential of an

electron rises by merging the atomic wells (the electron-electron interaction is omitted here for simplicity). Deep AOs are localized in the atomic Coulomb well (in the so-called core levels).

When AOs with higher energy interact, they form broad wells delocalized on the molecule, the molecular orbitals (MOs). The earlier defined HOMO, LUMO, ionization energy (IE), electron affinity (EA), and energy gap (E_{gap}) are depicted in the Figure, with respect to the VL. Figure 1.2.c depicts the electronic structure of an organic solid, in which the molecules interact only by weak interactions. In fact, molecular solids (crystals or amorphous films) are held together by van der Waals bonds. These interactions are based on weak electrical dipole forces between neutral molecules, thus are considerably weaker than covalent bonds found in inorganics. The nature of bonding in organic materials is fundamentally different from that found in inorganics.

The consequences of the weak bonds affect many of the mechanical and thermodynamic properties, such as mechanical hardness or melting point, as well as optical properties and (as it will be discussed in the next section) charge carrier transport.

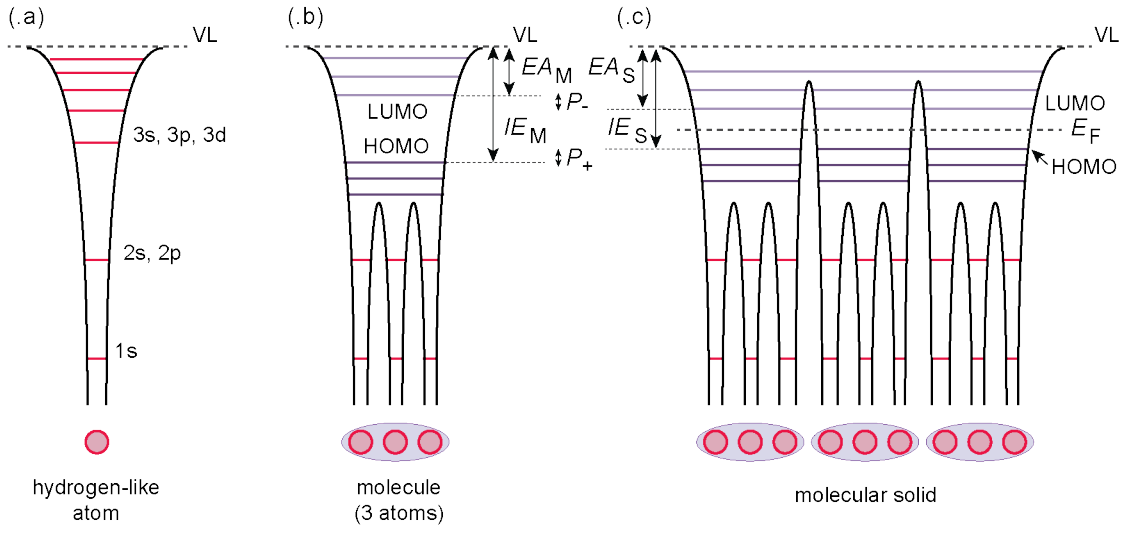

Figure 1.2. Evolution of electronic structures from a hydrogen-like atom (.a) to an organic solid (.c). The difference between molecule's ionization energy (IE) and the electron affinity (EA) in both gas phase and in the molecular solid are depicted. Modified form [47,55].

Furthermore, the weakness of the intermolecular interaction affects the molecular orbitals (π and π*), which are highly localized on individual molecules; and only a small overlap occurs between neighbor molecules in the solid. Therefore the electronic structure of a molecular solid derives from (and approximately preserves) the characteristic of the single constituent molecules. In an organic molecular solid, charge carrier transport involves ionic molecular states rather than energy band transport, which is typical for inorganic solids. In fact, the ionization of a (neutral) molecule M of the solid produces the polarization of the surrounding molecules.

This electronic relaxation of the neighboring molecules screens the charge on the ionized molecule M, leading to a decrease of the ionization energy (IE_S) and an increase of the electron affinity (EA_S) of the solid, with respect to the values of the isolated molecule (in gas phase, reffered as IE_M and EA_M), see Figure 1.2.b vs. Figure 1.2.c.

Figure 1.3 depicts the different environment between molecules in the gas phase and in an organic solid, with the consequent polarization of the neighbor molecules. The difference between *IE* and *EA* in the gas phase and in the solid phase is related to the potential energy of an electron in a Coulomb potential (φ_C) of the cation in vacuum $\left(\varphi_C = {}^{e}/_{4\pi\varepsilon_0 r}\right)$, and the cation in the solid $\left(\varphi_C = {}^{e}/_{4\pi\varepsilon_0\varepsilon_r r}\right)$ [47].

The *electronic polarization energy* (in the order of several hundreds of meV [48,49]) of the positive and negative polaron (P_+ and P_-) is therefore defined, respectively, as

$$P_+ = IE_M - IE_S; \qquad \text{(Eq. 1.4)}$$

$$P_- = EA_S - EA_M. \qquad \text{(Eq. 1.5)}$$

Once the molecules are brought together in the solid, the definition of the energy gap for the single molecule (see (Eq. 1.1) is modified, and therefore the *transport gap* in the solid is defined as

$$E_{transp} = IE_S - EA_S = E_{gap} - (P_+ + P_-). \qquad \text{(Eq. 1.6)}$$

From this relationship, it follows that the aforementioned exciton binding energy in a solid is less than that found in a molecule in the gas phase.

The polarization effect of the surrounding molecules is furthermore influenced by the structural order in the organic solid, i.e. in moving from a molecular crystal to an amorphous organic solid, the local variation of the polarization energies, due to the

different local environments, plays a role in the distribution of the transport sites that lead to a Gaussian distributed density of states [50,51].

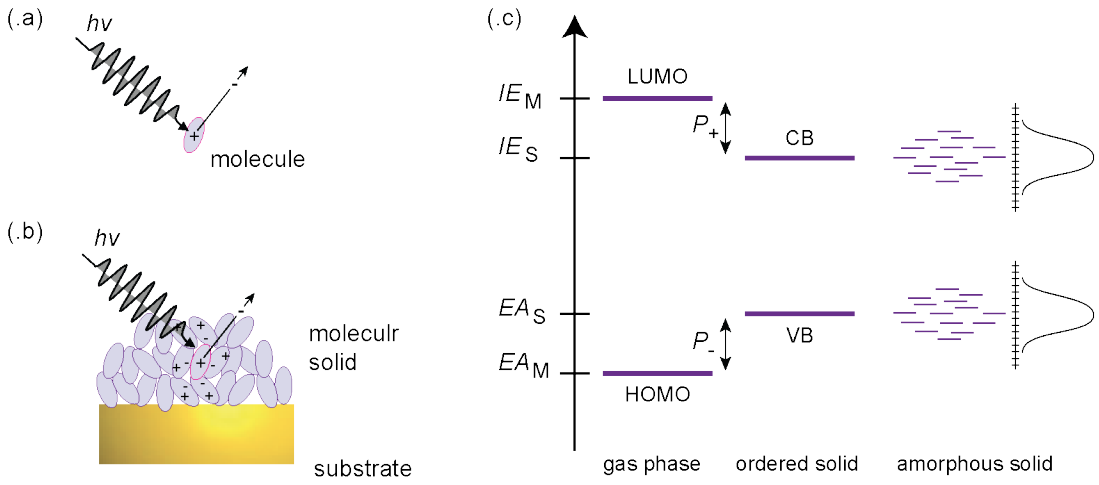

Figure 1.3. The different ionization process as occurring in a molecule M in the gas phase and embedded in a molecular solid (.b), upon photoionization energy *hv*. The polarization of the neighboring molecules is depicted in (.b). Energy levels (.c) of an isolated molecule, an ordered crystal, and an amorphous solid.

1.2. Hybrid organic/inorganic interfaces

In order to build working devices and integrate them into electronic circuits, organic semiconductor films must be put into contact with electrodes that provide sufficient charge injection/extraction. Electrodes made of inorganic materials are usually used in devices; an obvious exception is the so-called *all-organic* family of devices.

There are countless phenomena occurring at the hybrid interface between organic and inorganic to be considered for the production of efficient devices, such as the arrangement of organic molecules on the inorganic substrates, the nature of the interaction between materials, energy alignment at the interface, etc.

In the following section, a schematic review of the main phenomena to play at role in this research will be provided.

1.2.1. Physisorption vs. Chemisorption

For the practical production of devices, the organic materials must be deposited to obtain a thin film. Two categories of techniques are commonly used for the deposition process, depending on the nature of the chosen materials:

- *Thermal deposition*. If the molecules are thermally stable, they can be heated to their sublimation point. In this case, a vacuum environment is needed: vacuum conditions allow the molecular vapor to travel directly toward the target object (substrate), on which it condenses to the solid state and forms a thin film. To guarantee substrate cleanliness and reduce contamination in the growing thin film, Ultra-High Vacuum (UHV) is used (< 10^{-9} mbar). Since no solvents are involved in the formation of the film, the growth process depends entirely on the substrate-absorbate and absorbate-absorbate interactions;
- *Solution processing* requires the absorbate to be diluted in a (volatile) solvent. A physical process is involved to remove the solvent and leave the substrate on the desired thin film. This technique has the clear advantage of being more accessible in terms of time and cost, although cleanliness and repeatability might be important issues of which one must be aware.

Small molecules may be more thermally stable but less soluble than polymers, whereas functional chain-groups can be added, in order to improve the affinity with the solvent.

Depending on the strength of the interaction between the substrate and the absorbate, the bound is usually classified between two extreme cases.

- When weak interactions between molecules and substrate occur, the process is due to physical adsorption, or, in short, *physisorption*. The binding energy in physisorption (10 – 100 meV) is generally lower than the energy needed to break intramolecular bonds, thus the interaction retains the chemical structure, although distortion may occur [52,53]. The leading forces are van der Waals, as well as long-range electrostatic interactions. The origin of these forces are dipole-dipole interactions of polarized or polarizable molecules and substrate surface atoms, i.e. interactions between permanent dipoles, between a permanent dipole with an induced dipole, and between mutually induced dipoles. Analytical description of the three different interactions leads to different expressions for the potential $V(r)$, which scales with the power law $V(r) \propto r^{-6}$ [44].

  Taking into account the repulsion caused by Pauli principle, expressed as a short-range Coulomb potential, the physisorption is often expressed with the *Lennard-Jones potential*:

$$V(r) \propto \left[\left(\frac{r_0}{r}\right)^{12} - \left(\frac{r_0}{r}\right)^{6}\right]; \qquad \text{(Eq. 1.7)}$$

where r_0 is referred to as the *van der Waals radius* and is the position in which the potential is at its minimum.

Strictly speaking, physisorption generally never occurs, because a weak electron density rearrangement will always take place at the interface (e.g. "push-back" effect, see below).

- If the interaction between the substrate surface and the absorbate involves strong interactions (bonding energy is stronger than the covalent intramolecular bonds), new chemical bonds are generated at the interface between the substrate and absorbate. This is referred as chemical adsorption, or *chemisorption*. Chemisorption can occur when small molecules are deposited via thermal sublimation, as well as in solution processing (e.g. self-assembling monolayer [54]). Depending on the strength of the charge transfer, covalent or ionic bonds are found between the surface and the deposited molecules.

Both physisorption and chemisorption affects (with different degrees of intensity) the electron density at the organic/inorganic interface, thus the position of the molecular energy levels with respect to the Fermi level can change with respect to those of a molecule in the gas phase. The consequent energy level alignment at the electrode/molecule (as will be shown in the following sections) is of paramount importance for the fabrication of efficient devices.

1.2.2. Energy level at interfaces

When two materials are brought together to form the electrode interface (e.g. metal with small conjugated molecule film) the prediction of the energy levels arrangement does not (in general) simply follow the properties of the separate constituents [49,55–57]. Figure 1.4.a depicts the energy diagram of a metal (M) and an organic semiconductor (O), where the Fermi level of the metal (E_F) and the frontier orbitals of the molecule (HOMO and LUMO) are indicated respectively, with regards to their vacuum levels (VL_M and VL_O).

In the most simplistic approximation, when both M and O solids come into contact, no rearrangement of respective electric charge distributions occurs. Thus the electronic

structure at the interface follows the simple rule of vacuum level *alignment*, i.e. *Schottky-Mott limit* (mostly valid only for metal/inorganic semiconductor interfaces). According to vacuum level alignment assumption, the *hole-injection barrier* (ϕ_h) is defined as the difference between the ionization energy of the organic material (IE_O) and the metal work function (ϕ_M), while the *electro-injection barrier* (ϕ_e) is defined as the difference between ϕ_M and the electron affinity (EA_O) (as depicted in Figure 1.4.b), i.e.:

$$\phi_h = IE_O - \phi_M; \qquad \text{(Eq. 1.8)}$$

$$\phi_e = \phi_M - EA_O. \qquad \text{(Eq. 1.9)}$$

Practical systems most commonly do not follow the Schottky-Mott limit.

As seen in the previous section, organic molecules – once adsorbed on a substrate surface (even by physisorption) – are affected by interactions that can distort or change the electron distributions. In actual systems, therefore, a dipole layer may be formed at the M/O interface, with the consequent abrupt shift of the electrostatic potential at the interface, thereby leading to a virtual shift Δ of VL [55]. The value of Δ is determined by the magnitude of the interfacial dipole.

This phenomenon is usually referred as *change* (or *modification*) *of the work function* of the substrate.

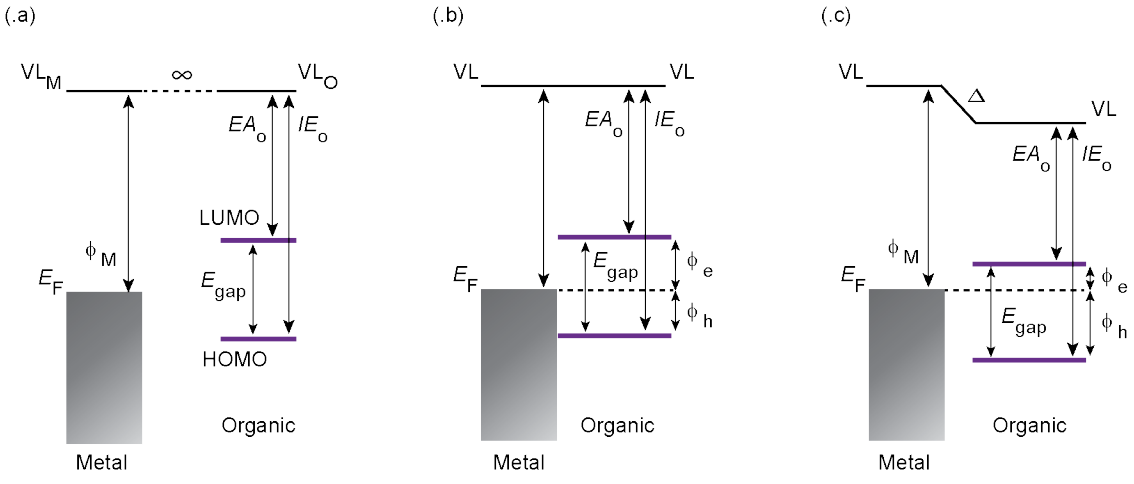

Figure 1.4. The electronic structure of a metal M and an organic solid at infinite distance is depicted in (.a). The M/O contact assuming vacuum level alignment (Schottky-Mott limit) is depicted in (.b), while the case in which the limit is not valid and a dipole Δ is present at the interface is represented in (.c).

The definition of hole-injection barrier and electron-injection barrier is modified from the definition given above and the interface dipole must be taken into account (see Figure 1.4.c), i.e.

$$\phi_h = IE_O - \phi_M - \Delta; \qquad \text{(Eq. 1.10)}$$

$$\phi_e = \phi_M - \Delta - EA_O. \qquad \text{(Eq. 1.11)}$$

The interfacial dipole layer has various origins, which can be categorized as (from weaker to stronger interaction) molecule-induced modification of the metal ϕ_M, charge transfer based on relative values of metal ϕ_M, and the organic IE_0 and EA_0, interfacial chemical reactions [56].

Push-back effect

In an atomically clean metal, the (positive) charge density $p(x)$ of the nuclei drops abruptly at the substrate surface, while the (negative) tail of the electron $n(x)$ spills out from the surface into the vacuum. For the neutrality of the metal solid, the excess of electron density δ^- outside the substrate surface must be compensated for by a deficiency inside the bulk δ^+. The distribution of the (positive and negative) charge densities gives rise to the surface dipole (SD) and the consequent electrostatic potential [47,56,57]. Figure 1.5.a is a cartoon illustrating the atomically clean metal and its positive and negative charge distributions.

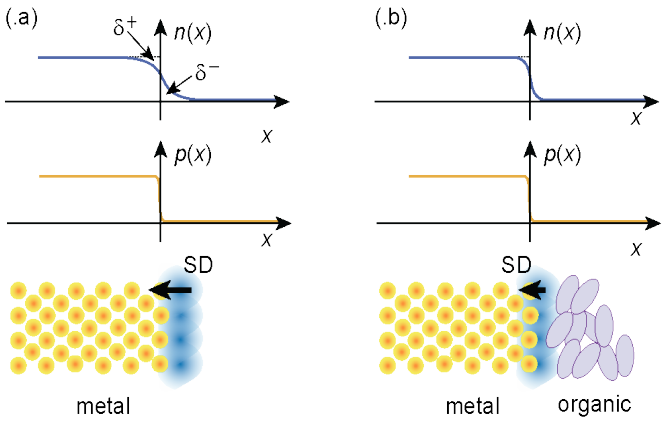

Figure 1.5. Origin of the push-back effect. Atomically clean metal in (.a), and metal with absorbed organic molecules and consequent reduction of the intrinsic surface dipole (SD) originated by the electron density distribution $n(x)$ in (.b).

The total work function ϕ_M depends on the bulk chemical potential (μ), as well as on the electrostatic potential across the surface (ϕ_{SD}), i.e.

$$\phi_M = \mu + \phi_{SD}. \quad \text{(Eq. 1.12)}$$

When molecules are physisorbed, the inner bulk potential is not affected by the weak van der Waals interaction, but the electrostatic potential at the surface can experience a non-negligible change with respect to the atomically clean metal surface.

The molecular electron cloud repulses the tail of the metal electrons extending in the vacuum (push-back effect, or so called pillow effect), lowering the SD and therefore lowering ϕ_M as well (see Figure 1.5.b).

Vacuum level shifts due to the push-back effect are substantially smaller (~ 1 eV) when the surface dipole SD is intrinsically smaller (e.g. oxide-passivated or contaminated metals [58], polymer electrodes [59,60]) with respect to atomically clean metals.

Charge Transfer

Figure 1.4 depicts the specific case, in which the substrate work function ϕ_S has a value within the EA_0 and IE_0 value ($IE_O > \phi_S > EA_O$). If so, assuming that the push-back effect could be neglected and only weak absorption occurs, Schottky-Mott limit is most likely to be valid [47].

More generally, the work function can fall outside the energy gap ($\phi_M > IE_O$ or $EA_O > \phi_S$) of the organic. Stronger interactions between adsorbed molecules and the substrate are then expected, since spontaneous charge transfer between substrate and organic will take place.

When bringing, for instance, an organic material in contact with a substrate with a work function ϕ_S greater than its ionization energy IE_0 (see Figure 1.6.a), a *positive charge-transfer state* is formed in the organic, and electrons will spontaneously flow from the organic into the substrate (see Figure 1.6.b).

The energy formation of the positive charge state (E_{CT+}) is defined as the energy required to remove one electron from the organic producing a fully relaxed state (both electronic and geometrically) [57]. As the electron transfer occurs, the organic at the interface becomes increasingly positive charged, while the substrate becomes increasingly negative. The opposite charge distribution forms an interface dipole (and consequently, an electrostatic potential Δ), which down-shifts the vacuum level (see Figure 1.6.c). The electron transfer occurs as long as equilibrium is not achieved:

where the E_{CT+} together with the potential Δ at the interface is equal to the work function ϕ_M of the substrate. As long as $\phi_S > E_{CT+}$, the work function of the interface will be equal to E_{CT+}, and the Fermi level is pinned to the positive charge-transfer state at the interface.

The reverse is the case when $\phi_S < EA_O$ (see Figure 1.6.d), and electrons will spontaneously transfer from the substrate to the organic with consequent formation of a *negative charge-transfer state* with energy E_{CT-}. The electron flow forms an interface dipole (and consequent potential Δ) that up-shifts the VL. Similarly, the charge transfer process will stop when $\phi_S + \Delta = E_{CT-}$. The Fermi level is therefore pinned to the negative charge-transfer state at the interface (see Figure 1.6.e).

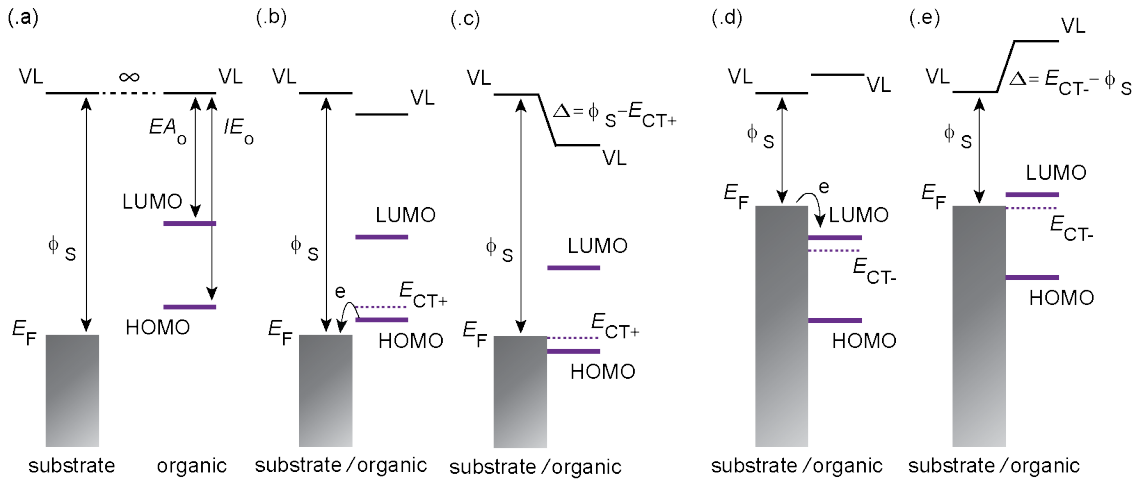

Figure 1.6. Schematic illustration of the energy level alignment when charge transfer occurs between substrate and an adsorbed organic semiconductor, in the case of $\phi_S > IE_O$ (.a, .b and .c), and $\phi_S < EA_O$ (.d and .e).

Covalent Bond

As seen in section 1.2.1, when organic molecules interact strongly enough to chemically interact with the substrate, the adsorption has a chemical character, i.e. the adsorbed molecules form a chemical bond with the substrate. The chemical bond involves a net charge transfer, which affects the energy levels with the downward (or upward) movement of the VL, due to an interfacial dipole-induced potential Δ_{Chem}. Furthermore, a significant change in the electron configuration of both organic and substrate can be unleashed. The direction of the net charge transfer follows the strength of the chemical potentials μ, i.e. electrons move from the material with

greater μ to the one with lower μ. Defining the chemical potential of the metal as $\mu_S = -\phi_S$ and the chemical potential of the organic as $\mu_O = -(EA_O + IE_O)/2$, the total number of transferred electrons δN_e can be written as a function of the two materials' chemical potentials and their specific hardness (η_S, and η_O) [61]

$$\delta N_e \approx \frac{\mu_S - \mu_O}{\eta_S + \eta_O}. \qquad \text{(Eq. 1.13)}$$

Since chemisorption implies a closer configuration between absorbed molecules and the substrate compered to physisorption, the push-back effect is at play and has the effect of down-shifting the VL, due to the substrate induced surface dipole ϕ_{SD} [57,62]. The overall work function-change is therefore a superposition of the physical (ϕ_{SD}) and chemical-induced potential (Δ_{Chem}).

1.2.3. Charge injection at contact

In organic semiconductors (when kept in the dark and not exposed to ionizing radiation), almost no intrinsic charge carriers are available ($< 10^{10}$ cm^{-3}) [51]. Therefore, charge injection through the electrodes is an extremely important parameter for the performance of organic devices. For this reason, both the charge injection and the transport at the organic-metal interface of the organic semiconductor devices have been extensively studied [60,63–65].

When an organic material is brought together with an electrode to form an electrical contact, due to interfacial interactions and the energy level alignment, a hole-injection barrier and an electron-injection barrier are formed. In order to thermally activate the injection, charge carriers must have sufficient kinetic energy to overcome such barriers, or the thickness of the interface barrier must be thin enough to allow tunneling. Since the symmetric conditions remain consistent for both electrons and holes, the following discussion is restricted to electron-injection, for the sake of simplicity. For reasons of geometry, one-dimensional treatment is sufficient.

To calculate the activation energy for an electron injection, the so-called *Schottky* effect must be taken into account: an injected electron at distance *x* from the surface of the metal experiences the influence of the electrostatic potential on the self-generated positive image charge. The image-charge potential is given by [50]

$$\psi_{\text{image}} = \frac{e^2}{16\pi\varepsilon_0\varepsilon_r} \cdot \frac{1}{x} \qquad \text{(Eq. 1.14)}$$

Figure 1.7 depicts the superposition between the potential ψ_{image} with the electric potential given, if an external electric field F (with potential $\psi_F = -\text{e}Fx$) is applied. The initial electron potential barrier at the interface ϕ (given by the difference between the electrode work function ϕ_{E} and the electron affinity EA_{O} of the organic) is lowered by the amount

$$\Delta\psi = \sqrt{\frac{\text{e}^3 F}{4\pi\varepsilon_0\varepsilon_r}}. \qquad \text{(Eq. 1.15)}$$

The potential superposition has a maximum in $x_{\text{m}} = \sqrt{\text{e}/16\pi\varepsilon_0\varepsilon_r F}$, where the potential has a height equal to $\phi_{\text{B}} = \phi - \Delta\psi$.

The current density as a function of the applied field *F,* due to the thermally emitted electrons (referred to as thermionic), is calculated by the *Richardson-Schottky* equation,

$$j_{\text{RS}} = AT^2 \exp\left(\frac{-\phi_{\text{B}}}{k_B T}\right) \qquad \text{(Eq. 1.16)}$$

where *A* is the *Richardson constant* proportional to the electron effective mass *m*.*

As mentioned, the injection can also occur because of the tunneling effect. Ignoring Coulomb effects and considering the mere tunnel through a triangular barrier with height ϕ_{B}, the tunnel current density has been calculated by *Fowler* and *Nordheim*

$$j_{\text{FN}} = \frac{A}{\phi_{\text{B}}}\left(\frac{\text{e}F}{\alpha k_B}\right)^2 \exp\left(\frac{2\alpha{\phi_{\text{B}}}^{3/2}}{3\text{e}F}\right), \qquad \text{(Eq. 1.17)}$$

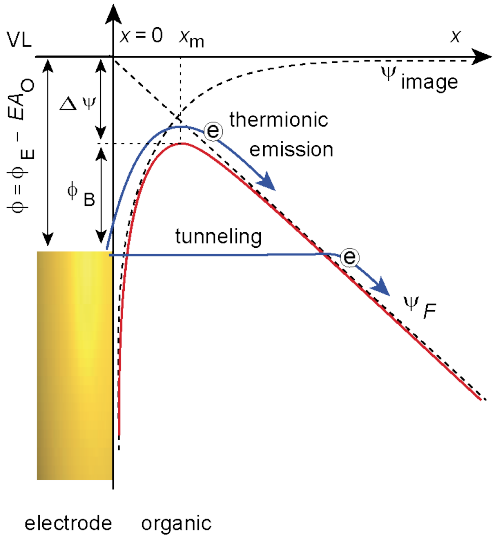

Figure 1.7. The barrier for the injection of an electron from an electrode into an organic semiconductor, under an applied electric field *F*. The barrier ϕ and ϕ_{B} are the height of barriers without and with the image charge. Modified from [46,50].

where α is a constant dependent on the square root of m^*.

1.3. Charge transport in organic conjugated systems

Two distinct electric processes at the organic/electrode junction are responsible for limiting the current in organic semiconductors: the charge-injection, and the space-charge in the bulk. Injection-limited current (ILC) occurs at the electrode interface when the zero-field contact barrier is higher than 0.25-0.30 eV [66,67]. Generally speaking, the ILC regime is affected by many factors, such as external electric field, temperature, and interface dipoles [55,56,68,69]. If ILC does not occur, i.e. one of the electrode contacts has good injection properties and can provide an unlimited carrier reservoir (the contact is referred as *ohmic*), the current is limited by the transport of charge carriers in the material bulk. The resulting carrier transport is referred to as a *space-charge-limited current* (SCLC, see section 1.3.2) [50,70].

The simplest organic device consists of an organic semiconductor film with length d, between two electrodes. Once charge carriers are injected from one of the electrodes into the organic semiconductor, their transport (upon the applied electric field F within the organic material) is determined by the conduction properties of the material itself, and is calculated as

$$j = q\,\varrho(x)\,\mu(x)\,F(x) - qD\frac{d\varrho}{dx}, \qquad \text{(Eq. 1.18)}$$

where x is the distance from the injection electrode, q is the absolute value of the charge carrier, $\varrho(x)$ is the density of the charge carriers, and $\mu(x)$ is the material mobility. The second term is the diffusion carrier term with diffusion constant D.

In the following section, a short overview of the model describing how the transport of the charge carriers occurs in organic semiconductors will be provided.

1.3.1. Hopping transport in organic disordered semiconductor

Since the organic semiconductors chosen for this thesis (as most of the common materials used in organic devices) are amorphous rather than crystalline, the focus will be set on disordered materials.

Because of the absence of a three dimensional periodical lattice structure, charge transport in this kind of system cannot be described by the standard model of band

conduction. The electrical transport mostly occurs by way of *hopping*. As depicted in Figure 1.3.e, amorphous materials are characterized by an energetically inhomogeneous distribution of the localized transport states for the charge carriers (holes and electrons). Due to different energy levels between neighboring molecules, the probability of carrier transport within two molecules (the hopping process) is a function of the energy difference.

The concept of hopping transport was first introduced by E. Conwell and N. Mott in 1956, in order to describe impurity conduction in inorganic semiconductors [71,72]. The hopping transport theory has been further developed by R. Marcus [73]. In his work, he calculated the rate at which a carrier can hop from site *i* to site *j*, both belonging to different chemical species. The hopping rate (ν_{ij}) is calculated with an Arrhenius equation, used to describe temperature-activated processes. In 1960, A. Miller and E. Abrahams proposed a similar model that shows explicitly the contribution of tunneling and thermal activation [74].

In 1993, Bässler adopted the Miller-Abrahams model to describe charge transport in disordered organic solids [75]. Considering that the absorption spectra of disordered organic materials usually have Gaussian profiles [75], the first assumption in this model is a Gaussian distribution of the molecular energy states (or *density of state,* DOS):

$$G_{\mathrm{DOS}}(E) = \frac{1}{(2\pi\sigma_{\mathrm{DOS}})^2}\exp\left(-\frac{(E-E_0)^2}{2{\sigma_{\mathrm{DOS}}}^2}\right), \qquad \text{(Eq. 1.19)}$$

where DOS is assumed to be centered in E_0 and to have a width σ_{DOS}.

The probability ν_{ij} for a carrier hopping from state *i* to state *j* (situated x_i and in x_j and with energy E_i and E_j, respectively) is calculated as

$$\nu_{ij} \approx \exp\left(-2\gamma a\frac{\Delta R_{ij}}{a}\right)\cdot \qquad \text{(Eq. 1.20)}$$

$$\begin{cases} \exp\left(-\dfrac{E_j - E_i - \mathrm{e}F(x_j - x_i)}{k_B T}\right); & \text{if } E_j > E_i + \mathrm{e}F(x_j - x_i) \\ 1; & \text{if } E_j < E_i + \mathrm{e}F(x_j - x_i) \end{cases}$$

where the ratio $\Delta R_{ij}/a$ is the relative jumping distance between molecule *i* and *j*, a is the lattice constant, and γ is the inverse localization radius related to the electronic coupling matrix element between adjacent sites. The expression for the hopping probability does not imply symmetry ($\nu_{ij} \neq \nu_{ji}$), since, while the hopping transport to

a lower energetic state requires no activation energy, the hopping to a more energetic state must be thermally activated to overcome the difference in energy. The carrier transport is schematically illustrated in Figure 1.8.a.

With the Gaussian disorder model (GDM), the charge transport cannot be solved analytically and thus Monte Carlo simulations must be applied [75–77].

The Monte Carlo simulations reveal that carriers with an energy within the DOS (Gaussian distribution centered in E_0 and with width σ_{DOS}) relax to an equilibrium level (positioned at $-{\sigma_{\mathrm{DOS}}}^2/k_BT$) below the center peak, thus energy is required for (the thermal activation of) the hopping in the *transport level* located at $-(5/9){\sigma_{\mathrm{DOS}}}^2/k_BT$.

The result of Bässler yields an (non-Arrhenius like) expression for the mobility μ as a function of T for disordered organic material:

$$\mu(T) \propto \exp\left[-\left(\frac{2\sigma_{\mathrm{DOS}}}{3k_BT}\right)^2\right]. \qquad \text{(Eq. 1.21)}$$

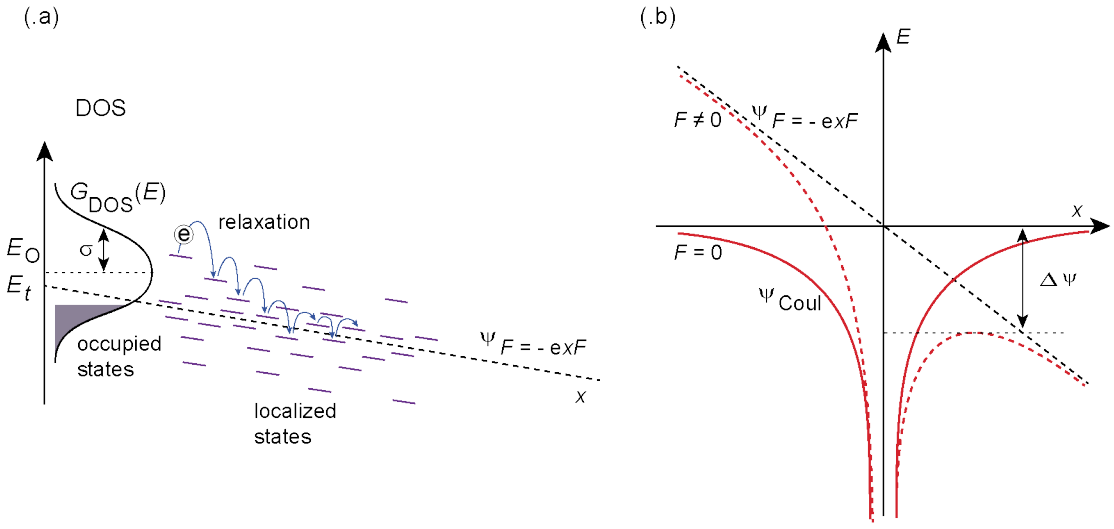

Figure 1.8. Transport process within a disordered organic semiconductor in (.a). The DOS is assumed to be Gaussian distributed (centered in E_0 and with half-width σ), upon an external field F. The hopping process is between localized molecular states either with lower or higher energy. Coulomb potential well in the presence of an electric field F in (.b). Due to the superposition of potentials, the effective potential is reduced by a factor proportional to $\sqrt{F}$.

In addition to temperature dependency, the mobility in organic disordered materials exhibits a characteristic field dependency. The modification, due to the Coulomb potential (ψ_{Coul}) in the presence of an electric field F (with potential ψ_{F}), is to lower the energy barrier for a charge carrier hopping in the direction of the field by $\beta\sqrt{F}$, as illustrated in Figure 1.8.b. This so-called *Poole-Frenkel* behavior is described by:

$$\mu(F) \propto \mu_0 \exp\left(\beta\sqrt{F}\right). \qquad \text{(Eq. 1.22)}$$

being μ_0 the mobility at zero-fielf ($F = 0$), and β is the so-called *amplification factor*.

Pasveer et al. expanded the Bässler model, formulating that a comprehensive description of the mobility as a function of the temperature T, the applied electric field F, and the density carrier [78].

The material mobility can therefore be a written combination of two terms, one dependent on the carrier density ϱ and the other dependent on the field:

$$\mu(\sigma_{\mathrm{DOS}}, T, \varrho, F) \approx \mu(\sigma_{\mathrm{DOS}}, T, \varrho)\, f(\sigma_{\mathrm{DOS}}, T, F). \qquad \text{(Eq. 1.23)}$$

1.3.2. Electrical transport

The *current density* j is the quantity that macroscopically expresses the charge transport in the molecular scale. If the contact between the (carrier injector-) electrode and the organic semiconductor provides an ohmic contact – i.e. the current density is not limited by the injection process itself – the maximum density current in the device is limited by the transport process. Once the charge carriers (q) are injected from the electrode into the organic material, they will be carried between the two electrodes, due to the electric field. The reciprocal interaction between the carriers affects the total concentration (changing locally the internal field), and thus the overall mobility of the material. This conduction model is referred as *space charge limited current* (SCLC).

The total carrier density $\varrho(x)$ is given by the contribution of both free and trapped charge carriers. The free (mobile) carriers hop around the transport E_t energy (see previous section) and, in the steady state, give rise to the device current; their density is referred as $\varrho_f(x)$. The trapped (immobile) charge carriers mostly do not contribute to the conduction process, since they remain above E_t; their density is noted as $\varrho_t(x)$. The localized states in which carriers are trapped are commonly described in the context of organic semiconductor as the tails of the Gaussian distributed DOS, of the

exponential density of states, or of other isolated traps present in the semiconductor [79].

The presence of the electric field prevents the spatial independence of the hopping process – diffusion term in (Eq. 1.18) can be neglected – shifting the relative position of the DOS along the electric potential (see Figure 1.8). The free carriers are transported by the action of the applied electric field $F(x)$ between the two electrodes (with relative distance *d*), and the current follows the drift equation

$$j(\varrho, \mu, F) = q\ \varrho_f(x)\ \mu(x, T, F, \varrho)\ F(x) \qquad \text{(Eq. 1.24)}$$

where ϱ_f, μ are the density of the free carriers and the mobility of the material, respectively. With the following set of equations and boundary conditions, an analytical expression for the density current can be found

Poisson eq. $$\frac{dF(x)}{dx} = \frac{q}{\varepsilon_0 \varepsilon_r}\ \varrho(x), \qquad \text{(Eq. 1.25)}$$

Continuity eq. $$\frac{d\varrho(x,t)}{dt} = \frac{1}{q}\frac{d}{dx}\ j(x), \qquad \text{(Eq. 1.26)}$$

Boundary condition $$U = \int_0^d F(x)dx, \qquad \text{(Eq. 1.27)}$$

Charge density $$\varrho = \varrho_f + \varrho_t. \qquad \text{(Eq. 1.28)}$$

Only for few limiting cases, analytical solutions can be found for the current in the SCLC regime. The discussion in the following section is restricted to unipolar devices, i.e. those in which the current density is carried by only one type of charge carriers. The hole-only device will also be discussed.

Constant mobility and without traps states

In the special case of a trap-free semiconductor ($\varrho = \varrho_f + \varrho_t = \varrho_f$, since $\varrho_t = 0$), in which the mobility $\mu(x, T, F, \varrho)$ is homogenous and not a function of x, T, F, ϱ (μ_0 is a constant), the equation for *j* can be solved analytically with the set of equations (Eq. 1.25) - (Eq. 1.28). In solving the Poisson equation in particular, if the number of the injected free charge is not negligible, the expression for the density current is the so-called *Mott-Gurney* equation (also indicated as a trap free space charge limited current, TF-SCLC):

$$j(U) = \frac{8}{9}\varepsilon_0 \varepsilon_r \mu_0 \frac{U^2}{d^3}. \qquad \text{(Eq. 1.29)}$$

If, on the other hand, the density of carriers is negligible, the solution of the Poisson equation reduces to the Ohm law $j(U) = e\mu N_f\, U/d$, where N_f is the number of free charge carriers.

Constant mobility with discrete trapping states

Let us now consider the rare case of an organic semiconductor with single energy level traps. The energy distribution $h(E)$ can therefore be written as $h(E) = N_t\, \delta(E - E_t)$. If the energy E_t of the traps is between the Fermi level and the *IE*, traps are then referred to be *shallow traps*. The carriers will fill all the trap states until the so-called *trap filled limit* is reached, due to the field assisted transport.

The ratio between trapped carriers (N_t) and the free carriers (N_f) can be described by the parameter θ ($\theta = N_f/N_{\mathrm{TOT}}$) defined as

$$\theta = \frac{N_f}{N_f + N_t}.$$

The solution of the Poisson equation is therefore

$$j(U) = \frac{8}{9}\varepsilon_0\varepsilon_r\mu_0\theta\,\frac{U^2}{d^3}. \qquad \text{(Eq. 1.30)}$$

This expression has the same form as TF-SCLC (Eq. 1.29), substituting the mobility with an *effective mobility* ($\mu_{\mathrm{eff}} = \mu_0\theta$), corrected by the factor θ. Obviously, if no traps are present ($N_t = 0$), θ becomes equal to unity, and (Eq. 1.30 is identical to (Eq. 1.29.

If the traps are deep, i.e. E_t lies above the Fermi level, an analytical expression for $j(V)$ cannot be found; however, a numerical calculation can be obtained [50,80,81].

Trapping states with energy distribution

Traps are generally found to be dispersed in energy, and they are gradually filled by the carrier transport, due to the increasing electric field. A common energy distribution $h(E)$ that follows an exponential decay, and for holes is given by:

$$h(E) = \frac{N_t}{k_B T_{\mathrm{trap}}}\exp\left(-\frac{E}{k_B T_{\mathrm{trap}}}\right)$$

where T_{trap} is the characteristic distribution constant. Based on an exponential trap distribution, with the so-called *trap-charge limited current* (TCLC) regime, the increase in current is then faster than the quadratic, up to the point at which all traps are filled.

The analytical solution of the Poisson equation gives a non-linear dependency with the applied bias

$$j(U) \propto \left(\frac{2\ell+1}{\ell+1}\right)\left(\frac{\ell+1}{\ell}\frac{\varepsilon_0\varepsilon_r}{eN_t}\right)\frac{U^{\ell+1}}{d^{2\ell+1}} \qquad \text{(Eq. 1.31)}$$

where $\ell = T/T_{\text{trap}}$.

1.4. Non-volatile memory devices

Organic semiconductors have been extensively studied and are nowadays used in many commercial electronic devices. Related to the impressive research efforts in the field of OLEDs, OFETs and OPVs, another category of electronic devices that are on the brink of being revolutionized by organic materials is the one of *memory devices*. Indeed, the increasing and persistent need for information storage is pushing traditional storage-technology (based on inorganic materials) to its theoretical and technological limits. New generations of memory devices based on organic materials have emerged as possible candidates as an alternative or supplementary to conventional semiconductor-based devices.

In electronics, a *memory device* refers to a component with the ability to store retrievable data over a period of time (retention time). The logical data storage occurs through a material's ability to change one physical property between (at least) two unambiguous metastable states, which can be associated with the bit "1" or "0" (i.e., On/Off, or True/False), respectively. The logical state of memory is written and read by a connected processing unit.

Memory devices can be divided into two categories, according to the endurance of the stored information. Memory is called *volatile,* if the information is lost as soon the device is turned off, i.e. they require a power supply to maintain the logical state. *Non-volatile* memories (NVM), on the contrary, have the ability to retain memory even if the device is not attached to a power supply.

Conventionally, memory devices are implemented based on three circuit elements: capacitors (C), transistors (T), and resistors (R), as well as on their combinations [18,26]. In its simplest form, a capacitor-based memory consists of a dielectric capacitor in which the information is stored according to the charging state of the capacitor itself. Since capacitors tend to discharge by leaking through conductive

paths, they must be periodically refreshed [18]. Longer retention time can be obtained by substituting the dielectric capacitor with a medium with ferroelectric nature [82,83]. Ferroelectric materials can be permanently polarized by an external electric field, and thus are good candidates for elements in so-called cross-point geometry for non-volatile memories. Each *two-terminal* ferroelectric capacitor-element is sandwiched between two (perpendicular) electrode-lines (see Figure 1.9.a). The cross-point architecture permits the closest possible architecture. Indicating with f the minimum width of the electrode-line (as well as the minimum inter-line space), each bit occupies an area of $4f^2$.

Memory devices based on the permanent polarization of ferroelectric materials are the so-called *ferroelectric random-access memory* (FeRAM). Alternatively, to reduce the discharging due to leaking conductive path, the capacitor can be coupled with a transistor and form a *three-terminal* 1C1T element (see Figure 1.9.b), typical in dynamic random access memory (DRAM). Both small molecules and polymers have been investigated as ferroelectric media for capacitors, such as metallo-porphyrines [84–86], ferrocene derivates [85], fluorocarbon-based monomers and polymers [87,88].

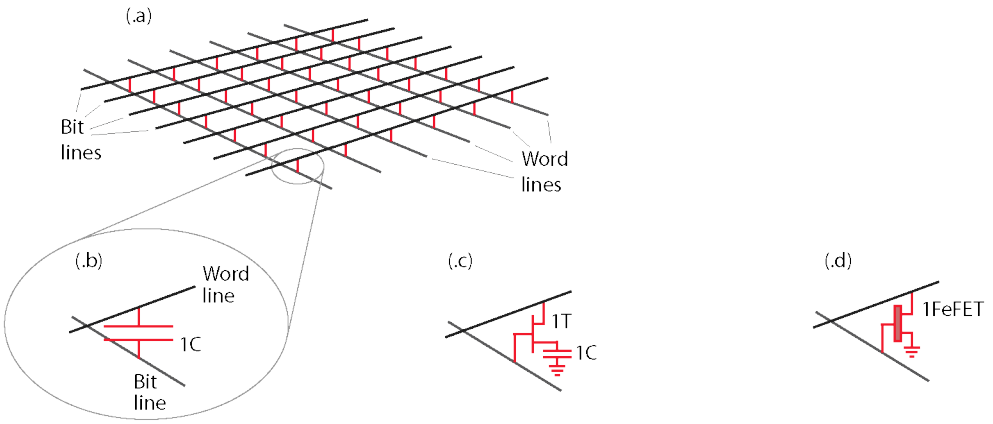

Figure 1.9. The circuit diagram of a cross-point architecture is depicted in (.a). At each intersection between bit lines and word lines a two-terminal capacitor is shown in (.b). Due to current leaking through conductive paths transistors are employed to preserve the capacitors charging. A typical three terminal 1T1C element is depicted in (.c). 1C1T element can be substituted by a ferroelectric FET for the sake of space saving (.d).

In order to reduce the space for a single bit (i.e. increase the information density) and to simplify the circuit, the 1C1T system can be substituted with a field-effect transistor with ferroelectric gate (FeFET) [18,89] (see Figure 1.9.c).

Integration of organic material for the realization of the 1T-memory can be convenient, since ferroelectric organic material can work as a gate dielectric without the need for an intermediate dielectric, thus reducing the risk of depolarization. Furthermore, ferroelectric organic materials exhibit a lower dielectric constant with respect to inorganics, i.e. reducing the depolarization field needed compared to oxide FeFET [28]. A common configuration for 1T-memory is using floating gate. In floating gate FET, the carriers are trapped on a conductive or semiconductive layer (which serves as gate), entirely surrounded by a dielectric [26,28,90]. The floating gate can be continuous or dispersed nanoclusters in an organic film (see Figure 1.9.d).

Devices incorporating switchable resistive materials can also be fashioned in a two-terminal structured and therefore be integrated into a cross-bar architecture. The logical information is stored in these materials through their ability to exhibit different conductive states. Because of their simple structure and scalability in large integrated circuits, they are promising candidates for the generation of future memory. 1R-memory devices are classified as resistive random access memory (RRAM). Since this thesis deals with resistive devices, in the following section a more detailed overview will be presented.

1.5. Organic resistive memory devices and switching mechanisms

The fundamental characteristic of a resistive memory device concerns its two different states of resistivity: the *high resistance state* (HRS, usually associated with the logical bit “0”) and the *low resistance state* (LRS, usually associated with the logical bit “1”). The resistance state can be changed by an appropriate electric stimulus. This resistance (/conductivity) is an intrinsic parameter of the material, thus no power is needed for the storage of the logical information. Memory devices based on resistance bistability are therefore NVMs (indicated in the following as R-NVMs).

As for other kinds of memory devices, if the material resistance is changed from one state to the other (the process is referred as *setting*), but the original state can never be *reset*, the memory is a so-called *write-once-read-many* (WORM). On the contrary, other devices display switchable bistability, i.e. the state can be arbitrarily switched

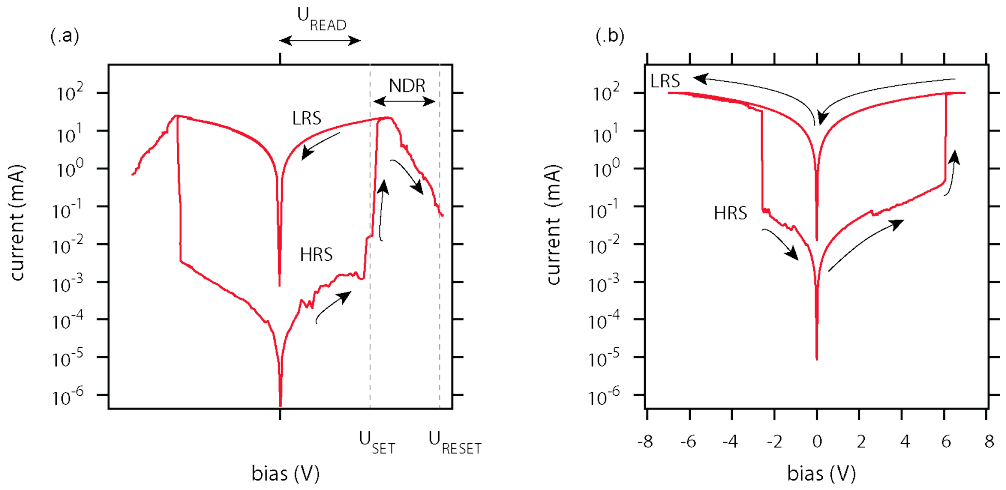

Figure 1.10. The *IU* curve of a unipolar R-NVM is shown in (.a). The bias at which the device switches from the HRS to the LRS is indicated as U_{SET}. The voltage range in which the device can be not destructively read is indicated as U_{READ}. By applying a bias greater than a threshold reset voltage (U_{RESET}) the device switches to the HRS. The curve for a bipolar device is shown in (.b).

between HRS and LRS. Depending on their current-voltage curve, they can be divided into two categories, *unipolar* and *bipolar*.

In unipolar NVMs, the switching direction does not depend on the polarity of the applied bias. Figure 1.10.a shows a typical current-voltage (*IU*) curve for R-NVMs [28,91,92]. The device switching from HRS to the LRS is displayed by the abrupt increase in current upon a specific applied critical bias U_{SET}. The device, after it has been set in the LRS, remains in such a state even if the applied bias is decreased below U_{SET}. The HRS can be reset by further increasing the bias above the critical value U_{ERASE}. The *IU* curve displays a negative differential resistance (NDR) between U_{SET} and U_{ERASE}. The device state can be "read" for any bias value below the NDR zone ($U_{\mathrm{READ}} < U_{\mathrm{SET}}$) non-destructively, i.e. the state is not modified by the reading process itself, as is the case for dielectric 1C-memories, for instance. In bipolar devices, opposite voltage polarities are required for the set and reset, respectively (see Figure 1.10.b).

To avoid over-programming (transition to a permanent HRS), the current can be limited by compliance upon bias, or a load resistor can be placed in series with the memory.

The number of structure and material combinations for NMR devices that have been reported to display resistive switch is remarkable, both for inorganic, organic, and

hybrid materials (a better overview can be found in referenced review papers [18,26,28,92]). The simplest structure (commonly reported, independently from the used materials) is based on metal-insulator-metal (MIM).

Many conjugated systems have been used as insulators in a MIM structure, such as the prototypical small molecules pentacene (PEN) [32,93], tris(8-hydroxyquinolinato)aluminium (Alq_3) [94,95], 4,4-bis[N-(1-naphthyl)-N-phenyl-amino]diphenyl (α-NPD) [96,97], as well as well known polymer such as polystyrene (PS) [36], polymethylmethacrylate (PMMA) [98].

Starting from the early 2000s [36,99,100], much research activity has been dedicated to two hybrid materials, in which metal nanoparticles (i.e. based on Au, Ag, Al, Mg, Cr) [31] are embedded in organic materials. Metal nanoparticles (MNPs) are imbedded in an organic/MNPs/organic three layer structure or blended into the entire organic bulk. Although R-NVMs often display similar current-bias characteristics, many mechanisms have been proposed to describe the switching behavior, which falls into two main categories: *field-induced switching* and *structural changes*.

1.5.1. Field-induced resistive switch

Mechanisms that involve changes of the device's internal field, with consequent effects on the current density, are reported in abundance in the literature. It is claimed that the presence of trapped immobile charges builds a space-charge field, which controls the current through the device. These mechanisms are often referred to as *Coulomb blockade* [15,18,29,30]. MNPs are imbedded into the organic material in the MIM structure both deliberately [30,99] or accidentally [32,101] during the top-electrode deposition. The claim effect of MNPs is to create trap sides for charge carriers and to allow bias-induced SCLC [30,31]. This switching mechanism is essentially identical to the one proposed by Simmons and Verderber (SV) for inorganic MIM diodes [102]. Most of the devices reported by different research groups [31,37,42,101,103,104] (although not all [15]) show NDR for a bias region above the set bias U_{SET} (see Figure 1.10). NDR is often explained as a gradual de-trapping of charge carriers [30,31]. A common feature reported for devices presenting NDR is the presence of intermediate resistance states (resistance value between the HRS and LRS), i.e. intermediate states are obtained by setting the device at a certain bias within the NDR region [30,42]. Although the SV model is often invoked as the driving mechanism for bistability, due

to the Coulomb blockade, there is a lack of systematic investigation of such important processes, i.e. how charge carriers enter and leave MNPs, or the actual conduction process in the HRS or LRS.

A different field-induced switching mechanism is the one reported for electron donor (D)-electron acceptor (A) complexes, characterized by electron transition(s). Charge transfer (CT) in a D-A complex was first observed in CuTCNQ (where TCNQ stands for tetracyanoquinodimethane) [105]. In ion-radical species, formed by the oxidation of donors or the reduction of acceptors, switching is induced by the electric field [16,26,105].

1.5.2. Resistive switch by filament formation/destruction

Filamentary conduction occurs when the current in the LRS flows in a localized path between the two electrodes [41]. Because the current flow occurs only in a specific region of the device, a distinct feature is that device resistance in the LRS is independent of the device area, while resistance in the HRS increases when the electrode size decreases [41,92].

Primarily, two types of filament path are reported [16,18,26]. One type is associated to carbon-rich filaments, formed by local degradation of the organic film [106,107]. The other is related to metallic filaments, resulting from migration of electrodes. Metallic bridging has been fully described and understood through redox reactions occurring in devices based on a thin electrolyte layer, sandwiched between an electrochemically active electrode, such as Al, Ag, Cu, or Ni, and an electrochemically inert metal electrode, such as Pt, Au, or W [35,41,108].

Figure 1.11 schematically depicts the formation of a filament in a device. The metal M of the electrochemically active electrode is oxidized at the interface, forming the cation M^{z+} when positive bias is applied between the electrodes ($M \rightarrow M^{z+} + ze^{-}$). The process is depicted in the top section of Figure 1.11.b. Upon bias, M^{z+} migrates toward the inert electrode and, once contact is established, reduces in the metallic form ($M^{z+} + ze^{-} \rightarrow M$), see bottom section of Figure 1.11.b. By increasing the number of active metallic atoms at the interface with the cathode, the formation of a (or many) complete metallic filament(s) into the thin film separating the electrodes, as depicted in Figure 1.11.c., is spurred. The device is therefore set into the LRS. When a negative bias is applied (Figure 1.11.d), the inverse process takes place, i.e. electrochemical

dissolution occurs and the metallic bridges can come to a stop, setting the device into the HRS. Once the filament is formed and then broken, it will function as a seed for successive filament switching (see Figure 1.11.e).

Joule dissipation, due to the increased current, also leads to thinning and degradation of the filaments, explaining the NDR region [109]. This filament-rupture process is depicted in Figure 1.11.f.

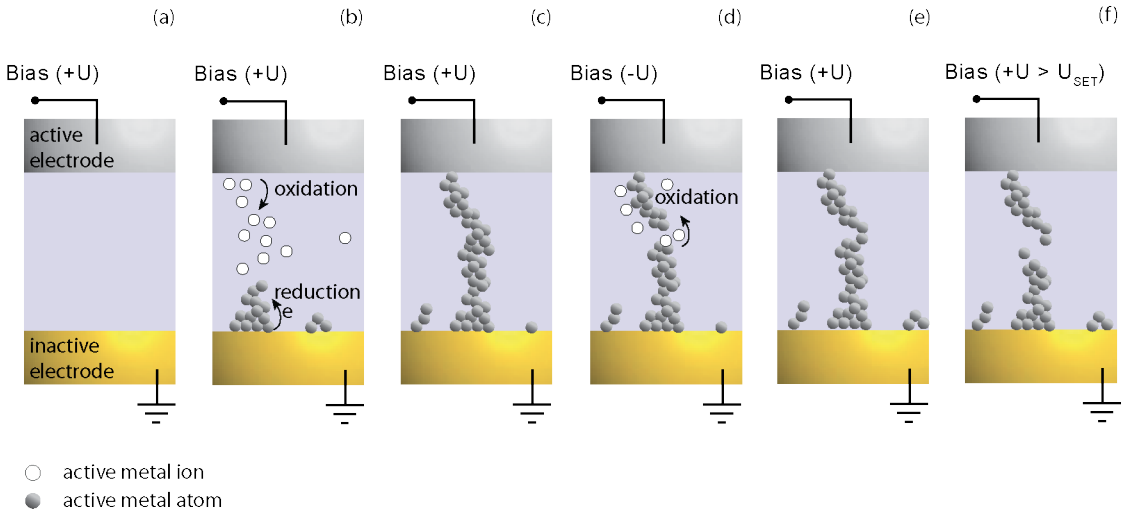

Figure 1.11. Filament formation in organic NVM devices. The pristine device is depicted in (.a). Reduction of the electrochemically active ions id depicted in (.b), leading to the formation of a complete filament, bridging the two electrodes (.c). Thinning of filaments leading to the rupture of bridges, due to redox reactions or Joule dissipation, are depicted in (.d) and (.f), respectively. Broken filaments act as a seed for successive filament switching (.e).

Chapter 2. Experimental techniques

This chapter presents a brief overview of the experimental techniques used in this work. The experimental setup of experiments will also be presented.

2.1. Photoelectron spectroscopy

For analysis of material electronic structure, photoelectron spectroscopy (PES) is a valuable tool [55,110,111]. PES probes the energy position of the occupied electrons' states and is thus a precious investigative tool for the chemistry and electronic properties at interfaces. The experimental technique is based on the photoelectric effect, i.e. the emission of electrons from matter as a result of light absorption.

In a common PES experiment (whose setup is depicted in the graphic in Figure 2.1), the sample is placed in an ultra-high vacuum system (base pressure 10^{-10} mbar) and irradiated by monochromatic electromagnetic radiation with energy $h\nu$. Directly after photo-absorption by the sample, if the radiation energy is at least higher than the work function of the sample (ϕ_{sample}, the energy to bring an electron from the sample surface into the vacuum level (see section 1.2.2), a photoelectron is emitted. The kinetic energy E_{kin} of the electron is directly related to the initial binding energy (E_{B}):

$$E_{\text{kin}} = h\nu - E_{\text{B}} - \phi_{\text{sample}}. \qquad \text{(Eq. 2.1)}$$

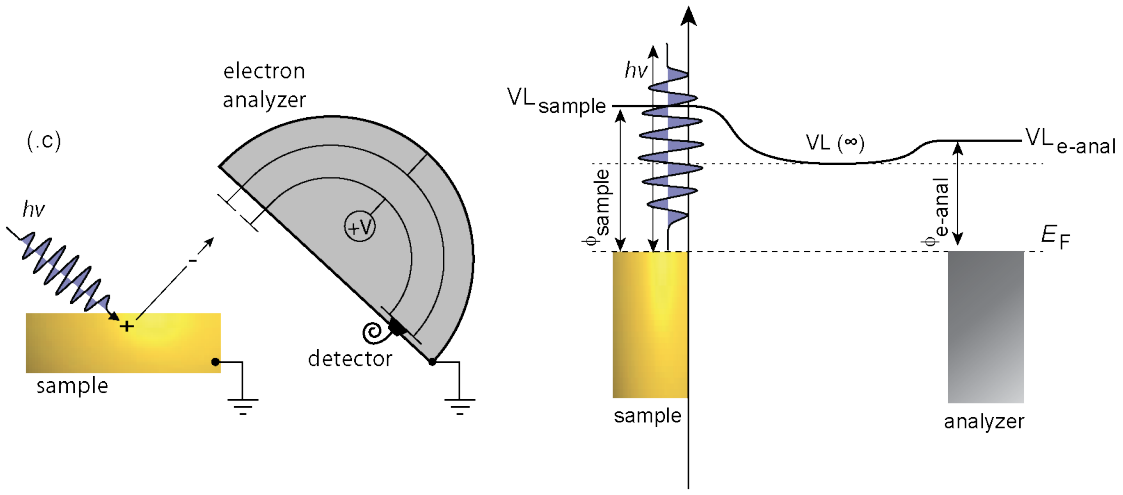

Figure 2.1. The experimental set-up for a photoelectron spectroscopy experiment is depicted in the graphic in (.a). The energy scheme in (.b) depicts the energy level alignment of the investigated sample with respect to the electron analyzer.

An electron analyzer (or spectrometer) collects and measures the kinetic energy of photoemitted electrons (see Figure 2.1.a).

The Fermi level of the electron analyzer and of the samples are aligned in thermodynamic equilibrium (since both are electrically grounded). Most likely, the work function of the electron analyzer ($\phi_{\mathrm{e-anal}}$) is different from that of the sample (ϕ_{sample}); therefore, the vacuum level will display variation along the electron trajectory (see Figure 2.1.b). Nonetheless, the measured kinetic energy E_{kin}^{M} is not influenced by variations in the vacuum level [112,113], since the electrostatic interaction is conservative and does not depend on the charge path, rather on the difference between potentials.

Since, for a given experiment, the potential difference between the sample surface (related to its work function) and the work function of the electron analyzer is constant, the measured kinetic energy E_{kin}^{M} is given by

$$E_{\mathrm{kin}}^{M} = h\nu - E_{\mathrm{B}} - \phi_{\mathrm{e-anal}} = E_{\mathrm{kin}} - (\phi_{\mathrm{e-anal}} - \phi_{\mathrm{sample}}). \qquad \text{(Eq. 2.2)}$$

The specific choice of the exciton radiation energy $h\nu$ fixes the depth of the sample electronic structure that is accessible (see below). By sweeping the kinetic energy from zero up to the maximum energy ($h\nu - E_{\mathrm{B}} - \phi_{\mathrm{e-anal}}$), the energy distribution curve is obtained. The cartoon in Figure 2.2.a schematically represents the generation of the electron analyzer' PES spectra as result of the photoemission of electrons from the excitation with radiation $h\nu$. For the sake of simplicity, we refer to the prototypical

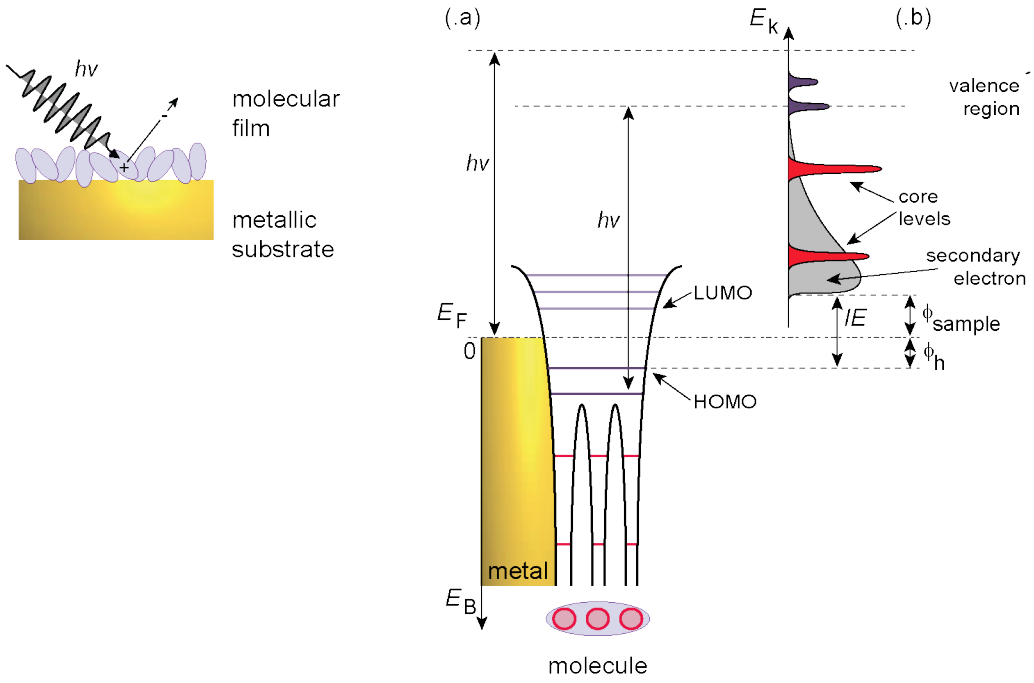

Figure 2.2. Electron structure probed by photoemission spectroscopy in (.a). The photoemission spectrum is shown in (.b). The depth of the structure energy accessible is determined by excitation energy $h\nu$. Here, binding energy E_B refers to the Fermi level E_L. E_k , ϕ_{sample} , ϕ_h are the kinetic energy of the photoelectron, work function and the hole-injection barrier, respectively. Adapted from [47].

molecule composed by three H-like atom (on a metal substrate) introduced in section 1.1.2. The PES spectrum is reported in Figure 2.2.b.

The electrons with highest kinetic energy originate from the highest unoccupied states (i.e. lowest binding energy) – the so-called valence region (VR). These electronic states can be the valence band for extended systems (crystals held together by covalent or van der Waals interactions), or σ- and π-orbitals for molecules. Metal presents a clear edge due to the Fermi level (E_F). Commonly, E_F serves as a reference for E_B, since ϕ_{e-anal} (as well as ϕ_{sample}) does not have to be known for calculating the binding energy. The core level (CL) region is located at lower kinetic energy, resulting from the photo-excitation of deep, localized atomic orbitals.

In the lowest kinetic energy region (close to zero) the main contribution to the spectrum is given by those electrons that are inelastically scattered (within the sample), i.e. the so-called secondary electrons. With decreasing E_{kin} the number of (i.e. intensity in the spectra) secondary electrons increases, up to the point where their kinetic energy is not sufficient to overcome the work function of the sample, and the intensity drops to zero. In a real experiment, an electron with $E_{kin} < \phi_{e-anal} - \phi_{sample}$

would not be able to be collected by the electron analyzer; therefore, electrons are accelerated by a potential of a few volts (typically 5 – 15 V).

An important parameter for photoelectron spectroscopy is the *electron escape depth*. It is defined as the distance perpendicular to the sample surface from which photoelectrons still manage to reach the analyzer.

As mentioned above, electrons traveling through a solid may experience energy losses due to electron-electron and electron-phonon interactions. Such interactions reduce the kinetic energy of a photoelectron in such a way that it either reaches the analyzer with lower kinetic energy or not at all (generation of secondary electrons). The longer the way the electron has to travel, the higher the probability for energy loss events.

Typically, the electron escape depth is quantified as *inelastic mean free path* (IMFP), defined as the distance at which the initial photo-emitted electron current I is decreased by the factor e^{-1}. Although the IMFP (for a certain kinetic energy) is element specific (due to the dielectric function), comparison of IMFP of different elements leads to a universal curve (see Figure 2.3). IMFP varies between 3 Å and 50 Å, and the minimum of the curve is located around 100 eV. The very small escape depth of photoelectron spectroscopy is responsible for the surface sensitivity of the method.

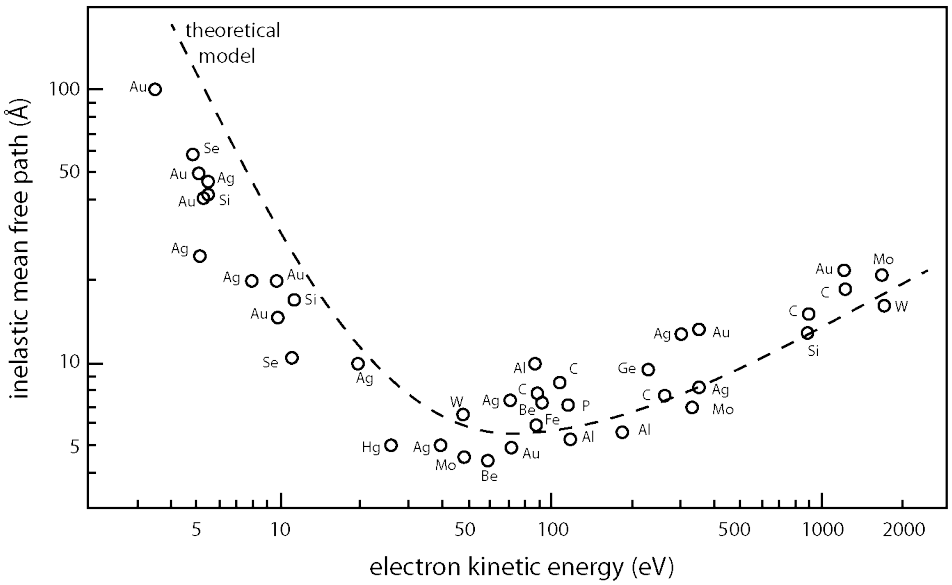

Figure 2.3. Inelastic mean free path of different elements as a function of their kinetic energy. After [110].

So far, the photoemission process of electrons has been described assuming systems with *non-interactive* electrons – often referred to as Koopmans' approximation. Koopmans' approximation states that the measured binding energy is the ground-state energy of the electron (accessible using Hartree–Fock approximation), the so-called *initial state*. This approximation holds only to some extent and is best used for free-electron band-like states, since it assumes that the removal of one of the N electrons from an orbital does not affect the rest of the electronic system (frozen orbital approximation). However, the remaining $N-1$ electron system interacts with the photo-hole (created by the photo-electron emission), relaxing the electronic structure. Therefore, PES does not exactly probe E_{B} of the initial state, but rather accesses the so-called *final state*.

The binding energy measured in a PES experiment is the difference between the total energy of the initial state with N electrons (E_i^N) and the final state with electrons (E_f^{N-1}), so that

$$E_{\mathrm{B}} = E_f^{N-1} - E_i^N = h\nu - {E_{\mathrm{kin}}}_i^N - \phi - \Delta E_{\mathrm{R}}. \qquad \text{(Eq. 2.3)}$$

The conservation of the elastic energy (Eq. 2.1) of the photo-electron assumed in a non-perturbed state must thus be corrected by adding an additional relaxation contribution (ΔE_{R}), due to photo-hole screening.

The effects of the polarization of the photo-hole manifest themselves depending on the specific polarizability of the media. For materials with high polarizability (i.e. metals), the screening of the photo-hole by the neighboring electron cloud is very efficient (especially in the electron-see in the valence band), and the Coulomb's interaction between hole and escaping electron is reduced. If the hole is created in materials with comparably smaller polarizability (i.e. dielectric material like organic materials), screening is less efficient. The Coulomb's interaction between the photo-electron and the (left) hole is stronger, and E_{kin} of the electron is reduced (E_{B} increased) as compared to the former case.

Figure 2.4 depicts an example of molecular films on a metallic substrate. At sub- and monolayer films, the metal half-sphere (underneath the molecules) is mainly responsible for the screening (see Figure 2.4.a). If the distance from the metal is increased, this influence becomes less important until virtually vanishing for thick organic films (see Figure 2.4.b).

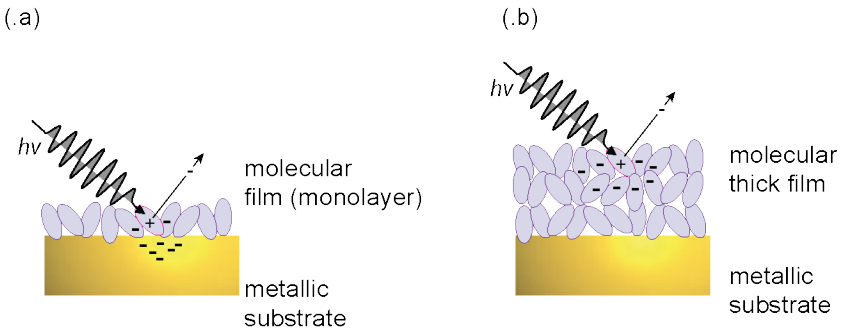

Figure 2.4. Photo-hole screening process. The case of a thin film (sub- or monolayer) is depicted in (.a). The case of a thick film is depicted in (.b).

A further consequence of the sample ionization is that charging neutrality must be re-established through current from the substrate (which must be grounded). This may lead to a positive charge build-up at the sample surface due to the low conductivity of many organic materials, and subsequent chemical reactions may occur between positively charged molecules.

Note that PES is generally a surface averaging technique, because the PES signal coming from sample location is usually in the range of μm^2 or even mm^2 in size.

As seen previously discussed (see Figure 2.3), the excitation energy of the photon, used to irradiate the sample, influences the depth of the electronic structure that can be accessed. PES is thus subdivided, depending on the excitation energy:

- *ultraviolet photoelectron spectroscopy* (UPS) when the photons are in the range of 10 - 100 eV;
- *X-ray photoelectron spectroscopy* (XPS) or electron spectroscopy for chemical analysis (ESCA) when X-rays (radiation energy between 100 eV - 10 keV) are employed.

Gas discharge lamps are used as laboratory sources for UPS. The gas employed is usually an inert gas; the most commonly used gas is He. If He is employed, depending on the gas pressure and discharging current, one can generate two different intensive lines with energy 21.2 eV (He I) and 40.8 eV (He II), with 3 meV and 17 meV as linewidth, respectively [114]. The narrow linewidth and low intensities of satellites allow work without monochromator.

The laboratory sources for XPS are X-ray tubes, in which the X-ray flux is created by bombarding a target with high energy electrons. Common target materials are Mg and Al, for which the emission spectrum is dominated by the unresolved doublet $K_{\alpha\,1,2}$ ($2p_{1/2} \rightarrow 1s$ and $2p_{3/2} \rightarrow 1s$ transitions) at 1253.6 eV for Mg and at 1486.6 eV for Al [114]. The linewidth of the $K_{\alpha\,1,2}$ doublet amounts to about 700 - 800 meV.

Alternative to the laboratory sources, one can use synchrotron light. The source of photons is the radiation emitted from an accelerated beam of charged particles. The range of the spectrum goes from a few eV to many keV; therefore, it is necessary to use monochromators to select the appropriate light energy. The high intensity, the total polarization, and the coherent characteristics of synchrotron light make this technique the most powerful tool in photoemission spectroscopy.

2.2. Atomic force microscopy (AFM)

The atomic force microscope (AFM) or scanning force microscope (SFM) was invented by Binnig, Quate, and Gerber in 1986 [115]. AFM is a versatile tool capable of high resolution topographical imaging, mechanical property analysis, and it is able to measure surface forces and interactions down to the nanometric scale. The technique can be applied in a range of media, such as air, fluid, or a gas atmosphere.

Typical resolution for AFM (1-10 nm in lateral resolution for most the commercial systems) approaches the limit of electron microscopic techniques, surpassing optical microscopy. The limitation of AFM resolution depends on the mechanical components of the system.

Figure 2.5.a shows the typical AFM setup. The AFM is basically composed of five elements: a cantilever with a sharp tip, a piezoelectric element (*x*-, *y*-, *z*-) scanner, a laser, a photodetector, and a feedback loop.

The AFM begins a scan by bringing the sharp tip that is mounted on the cantilever into contact with the sample surface. The tip diameter is in the nanometer scale (5 – 50 nm in radius) and is a parameter that determines lateral resolution.

The cantilever is very soft and behaves like a spring (typical spring constants range within 0.01 – 50 N/m), i.e. forces acting on the tip cause the cantilever to deflect. The motion of the cantilever is detected by a laser beam, which is reflected off the end of the cantilever (where the tip is located) and into a photodiode.

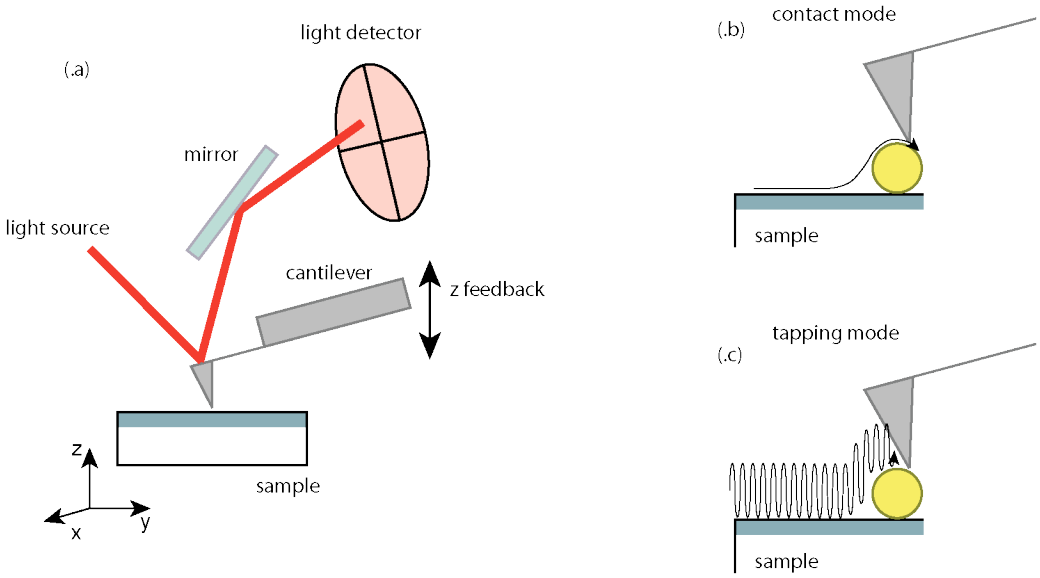

Figure 2.5. The experimental setup of an AFM is represented in the schematic in (.a). Different imaging modes are depicted: contact mode and tapping mode in (.b) and (.c), respectively.

The photodiode generally has four quadrants that measure changes in the position of the laser and thus the corresponding changes in cantilever deflection. These changes in laser position, or effective cantilever deflection, are recorded as a voltage by the photodiode. The deflection of the cantilever is used to measure the forces being applied on the tip. For example, when the tip is brought into contact with the sample surface, the repulsion force deflects the cantilever.

The cantilever is raster scanned across the surface in the *x*- and *y*- direction, using a piezoelectric scanner (depending on the AFM system, either the cantilever or the sample may be moved). A feedback loop is used to monitor the deflection of the cantilever and to dynamically control the *z*-position of the tip relative to the sample surface. The measurements performed with the feedback loop keep the cantilever deflection constant. The feedback loop adjusts the height of cantilever point by point (acting on *z*-direction in the piezoelectric element). This measurement configuration is called *contact mode.* Combining the *x*-, y- and *z*-data, the topographic 3D image of the sample can be collected.

The two main parameters that control the interaction of the tip with the sample during scanning are the *set-point voltage* and the *gains control*. The set-point voltage controls the applied force between tip and sample. For example, the higher the set-point voltage (which results in greater cantilever deflection), the higher the applied

force acting on the sample. The gains control is used to modulate the speed of the feedback loop. If the gains are set too high, the feedback becomes unstable and introduces noise. However, very low gains result in a poorly responsive feedback, i.e. the change in the *z*- height of the piezo cannot adjust in response to the topographic features.

Lateral forces generated by the contact mode scan of the cantilever tip can damage the soft sample (i.e. organic materials held by van der Waals interactions). To avoid this, (as well as to preserve the tip lifetime) *intermitted contact* (or *tapping*) *mode* is commonly implemented.

In tapping mode, the tip is held above the surface and allowed to oscillate at (or near) its resonant frequency. The tip amplitude oscillation is greater than the tip-surface distance, so that when the tip comes into contact with the surface, the amplitude is dampened (see Figure 2.5.c).

To obtain an image in tapping mode, the feedback maintains a constant amplitude (*set-point amplitude*) of the cantilever oscillation, as the tip is scanned across the surface. The amplitude set-point is typically set at 80% of the free amplitude. Similar to contact mode, changes in the height of the piezoelectric scanner, which are required to maintain the set-point amplitude, correspond to the height of the topographic features.

2.2.1. Conductive atomic force microscopy (C-AFM)

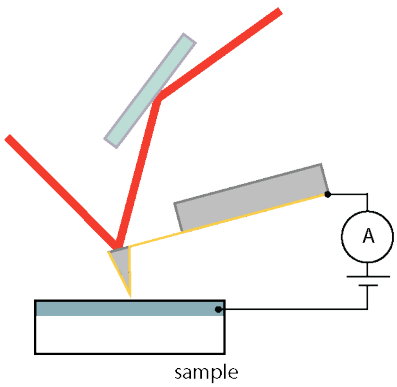

Figure 2.6. C-AFM experimen-tal setup. The cantilever has a conductive coating layer.

Conductive AFM (C-AFM) is a scanning probe microscopy (SPM) method that – using a conductive cantilever in contact mode – can perform electrical measurements of conductive samples. Figure 2.6 illustrates the setup of a typical C-AFM.

The conductive cantilever is generally a silicon or silicon nitride probe with a metallic or metallic alloy coating. A bias voltage is applied to the tip while the sample is held to ground potential. When the tip is brought to contact with the

sample surface, a current flows from the tip through the sample. Alternatively, a bias can be applied to the sample and the flow of current from sample to tip measured.

The current flowing between tip and sample is simultaneously measured with topography, as the tip scans across the surface. A conductive image is created using the current signal versus the *x*-, *y*- position of the tip on the sample.

As this technique is conducted in contact mode, damage to softer materials may occur due to lateral forces of the tip, and it is often the case that the conductive coating of the tip itself is damaged.

During the C-AFM experiment, the current passing between the tip and the sample is measured, converted into a voltage by an analog-digital converter. The voltage is then amplified and recorded. Therefore, a C-AFM module is not a standard voltage supply with a current meter, but a differential amplifier in a series with digital-analog converter (DAC) controller, which is used to source the bias voltages between the sample and the tip (virtual ground). The circuit board is as close as possible to the conductive tip glass holder and serves as a pA-amplifier.

Since the cantilever tip has a very small contact area (tens of nm^2, depending on the penetration of the cantilever in the organic material), the current must be limited with current-compliance, in order to limit the current density at the contact and thus damages to the cantilever.

Chapter 3. Materials and experimental details

In the following chapter, the materials that were used in the experimental sections, as well as the main techniques used for the fabrication of investigated samples, will be reviewed. The experimental details for the preparation of samples will be provided in the last section of this chapter.

3.1. Materials

3.1.1. Indium tin oxide (ITO) coated glass

There are several possible choices for the type of substrate to be used as an electrode in organic electronics. We decided to adopt the most widely used transparent electrode, indium tin oxide (ITO)[11].

ITO is a highly degenerate *n* type semiconductor with low resistivity, high transparency in the visible light spectrum, wide band gap, and relatively high work function [46,116]. For these reasons, ITO is frequently used on glass substrates and employed for panel display in flat devices as OLEDs, and solar cells. Despite the wide-spread use of ITO in both industry and research, the controlled production of coated ITO glass is still a challenge. Properties (e.g. instance morphology or work function) are indeed highly dependent on deposition techniques and conditions adopted, as well

[11] indium oxide (In_2O_3) and tin oxide (SnO_2), typically 90% In_2O_3 10% SnO_2 by weight

as post deposition treatments. Obviously, variations of ITO properties influence a device's performance. The effects of surface treatments (such as chemical cleaning, UV ozone, reactive ions etching) for application in organic electronics have been intensely studied [117–120]. In all related works, an evident relationship between physical-chemical treatments and a significantly large change of the ITO work function (range between 4.2 and 4.8 eV) is reported. Possible explanations include formation of surface electric dipoles [118] and carbon removal from the ITO surface [121], with consequent reduction of surface tension.

The ITO coated glass samples – used in the photoemission experiments (reported in Chapter 4 and Chapter 5), as well as in the nanostructured devices preparation (see Chapter 7) – were provided by Thin Film Devices Inc. All substrates come from the same batch of samples. The size of the ITO coated glasses is 10×10 mm $\pm$ 0.2 mm. The nominal ITO thickness is 145 $\pm$ 10 nm, with a nominal sheet resistance of 20 $\pm$ 2 Ω[12], as confirmed by four point probe resistivity measurements. The ITO/glass substrates used in the device experiments (reported in Chapter 6) were purchased from Präzisions Glas & Optik GmbH. The sample size is 25.4×25.4 mm $\pm$ 0.1 mm (1 inch square). The nominal ITO thickness is 120 $\pm$ 10 nm, with a nominal sheet resistance of 20 $\pm$ 2 Ω.

3.1.2. PEDOT:PSS

The contact interface between two different layers is never sharp [56]. As reported by A. Schlatmann et al., indium is found to diffuse into organic layers, thus acting as a trapping site for charge carriers [122]. In order to stabilize the anode interface and prevent indium and oxygen diffusion, another layer is inserted between ITO and the molecular semiconductor film. The layer is a thin film of poly(3,4-ethylenedioxy-thiophene): poly(styrenesulphonic acid) (PEDOT:PSS). PEDOT was originally introduced by G. Heywang in 1992 [123].

It is obtained from the polymerization of ethylenedioxythiophene (EDOT) monomers. The chemical structure is reported in Figure 3.1 (bottommost section). The polymer

[12] The *sheet resistance* (R_{SH}) of a thin film is defined as the ratio between the resistivity ρ and the thickness t of the film $R_{SH} = \rho / t$. The unit of the sheet resistance is therefore Ohm; however, it is often written as Ohms per square (Ω/sq).

shows interesting characteristics, including a relatively good electrochemical, ambient, and thermal stability of its electrical properties [123,124]. It is insoluble in many common solvents and unstable in its neutral state, as it oxidizes rapidly in air. To improve its processability, a polystyrene sulfonate solution (PSS) can be added, which results in an aqueous dispersion of PEDOT:PSS, where PEDOT is in its oxidized state. The PSS chemical structure is shown in Figure 3.1 (topmost section).

Figure 3.1. Chemical structure of PEDOT (bottommost part) and PSS (topmost) polymer chains, and how they mutually binded.

The binding between the two chains is due to the bridge between the phenyl rings of the PSS monomer and the acidic SO_3H groups. The combination yields to a water-soluble polyelectrolyte with properties suitable for film-forming, with high conductivity, with high visible light transmissivity, and with excellent stability. Films of PEDOT:PSS can be heated in an oxygen atmosphere at 100 °C for more than 1000 hours with only a minimal change in conductivity [125].

The electrical properties of PEDOT:PSS vary widely, depending on the solution formula as well as the film production procedure. The product in its original form has a conductivity of about 10 S/cm; this can be improved up to several hundreds of S/cm by adding a polyhydroxy (molecules which present many functional OH groups) compound (e.g. sorbitol or glycerol), or a decrease in conductivity, for instance by augmenting the PSS content. Conductivity is 10^{-3} S/cm for PEDOT:PSS with 1:6 ratio, 10^{-5} S/cm for 1:20 ratio [125]. PEDOT:PSS' work function is dependent on different formulations and processing conditions. Reported values for ϕ exhibit a significant spread from 4.8 to 5.2 eV [126]. The relative high work function of PEDOT:PSS – which results in low hole-injection barriers – favors the injection of holes from the anode into the active film, both with small molecule and with polymers semiconductors [126].

The main effects of the insertion of a PEDOT:PSS film between the transparent ITO anode and the first active layer are:

- acting as a buffer for the indium diffusion. Diffusion of indium through the ITO/PEDOT:PSS interface is observed, indicating that the polymer used as a buffer layer is not efficient as a complete indium filter [127];
- reducing the roughness of the substrate film, smoothing the ITO peaks.

The water saluted PEDOT:PSS used in this work was purchased from the H.C. Starck (CLEVIOS Al 4083). In the following section (see 3.3.2), the substrate preparation will be described in full.

3.1.3. Alq_3

Tris(8-hydroxyquinolinato)aluminium (Alq_3) is a chemical compound with the formula $Al(C_9H_6NO)_3$. Alq_3 is a metal complex wherein aluminum is bonded in a bidentate manner to the three 8-hydroxyquinoline ligands. The chemical structure is shown in Figure 3.2. Alq_3 is chemical stable, can be thermally sublimated, and yields to amorphous thin films [128]. Since 1987 [129], this conjugated compound is one of the most successful organic materials to be used in OLEDs, playing the dual roles of light emitter and electron transporter [130].

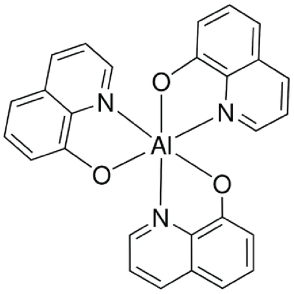

Figure 3.2. Alq_3 chemical structure.

The mobility of Alq_3 has been studied extensively [131–135]. Typical values of electron mobility are between 10^{-6} to 10^{-5} $cm^2\ V^{-1}s^{-1}$ in electric field in the range 0.1 – 1 MV cm^{-1}. In contrast, hole mobility is in the range of 10^{-9} $cm^2\ V^{-1}s^{-1}$ with the same intensity in the electric field.

Analysis of the molecular frontier indicate for Alq_3 IE = 5.8 eV and EA = 2.2 eV. Calculations based on density functional theory (DFT) predict that the HOMO is localized mainly on the phenoxide side of the ligands, whereas the LUMO set is localized on the pyridyl side [136,137]. This implies that oxidizing agents will attack the molecule on the phenoxide side of the ligands, and reducing agents on the pyridyl side [136].

Kahn and co-worker extensively studied the interaction between Alq_3 with highly reactive alkali, alkaline-earth, and other metals such as Ca, K, Li, Mg and Al [138–143], underlining the formation of organometallic structures.

3.1.4. α-NPD

4,4-bis[N-(1-naphthyl)-N-phenyl-amino]diphenyl (α-NPD, $C_{44}H_{32}N_2$), as hole injector and transport material, is one of the most studied small organic conjugated molecules. In fact, α-NPD is often combined with Alq_3 for the realization of OLED [46,51]. The chemical structure is shown in Figure 3.3. α-NPD chemical structure.

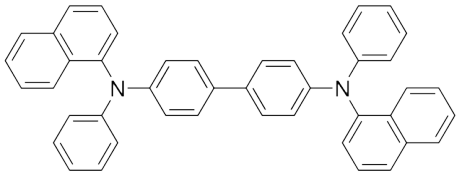

Figure 3.3. α-NPD chemical structure.

α-NPD is chemically stable, and sublimation at room temperature substrates produces stable amorphous films.

The charge carrier mobility has been investigated extensively [51,58,144–148]. Typical values of hole mobility are between 10^{-6} to 10^{-5} cm^2 $V^{-1}s^{-1}$. Additionally, the electronic structure of α-NPD has been the object of many studies by means of photoemission spectroscopy. Molecular ionization energy and electron affinity are 5.4 eV and 1.5 eV, respectively [58,149–151]. DFT calculation shows that the major contribution to the HOMO arises from the nitrogen atoms, thus indicating that N would be the most likely site of electronic excitation, i.e. N are the most chemically reactive sites [152].

3.1.5. Gold nanoparticles

Metals exhibit completely dissimilar behavior, once their dimensions are reduced from the macroscopic to the nanometric scale. Chemical or catalytic properties that are not normally (or only weakly) present in the bulk can be strongly different or enhanced in metal nanoparticles (NPs) [153–155]. The finite dimensions of the NPs with consequent electron confinement affects the discretization of the electronic energy levels [156–158]. This phenomenon was first highlighted by Fröhlich in 1937 [159]. However, a complete quantitative analysis was first developed in the early 1960s by Kubo [160,161]. The Fröhlich-Kubo model estimates the critical size of nanoparticles at which *non-metallic* behaviors (e.g. conductivity, thermal transport) are to be expected [162].

The critical particle size can be predicted, if the average space between successive quantum levels (δ) exceeds the thermal energies:

$$\delta \approx \frac{2}{3}\frac{\Delta_{CB}}{N_A z} > k_B T ;$$

where Δ_{CB} is the width of the conduction band crossing the Fermi level (in Au, 6s and 6p band ≈ 20 eV), N_A is the number of atoms in the particle, and z the valence number. Particular for gold (z = 1), the result is $\delta \approx 8\ \text{eV}/N_A$. This implies that the discrete nature of energy levels can be revealed at room temperature ($k_B T$ = 25 meV) in gold particles, if the number of atoms in the particles is less 300.

Optical properties (e.g. surface plasmon resonance) and changes in the electronic structures of particles can be observed in the nanoscale [158,163]. For this reason, metal NPs are nowadays being merged with organic semiconductors (both small molecules or polymers) to form hybrid materials and to be employed in different applications or devices, such as solar cells [164–166], light emitting diodes (LED) [167,168], and field effect transistors [169,170].

3.1.6. Molybdenum oxide

Thin interlayers of transition metal oxide such as molybdenum, vanadium and tungsten (MoO_3, V_2O_5, WO_3) play an important role as hole-injection layer, when placed between an electrode and a hole transport material [167,171].

MoO_3, in particular, was first employed as hole-injection layer in an OLED by Tokito et. al. in 1996 [172]. Since then, considerable effort has been directed toward understanding the mechanism that allows for a reduction in the charge injection barrier at the interface with organic semiconductor. In particular, the interface with α-NPD has been taken as case study [173–176].

The electron affinity (EA) and ionization energy (IE) of vacuum-grown MoO_3 are found to be 6.7 eV and 9.7 eV, respectively [174]. MoO3 films are n-doped by oxygen vacancies; the Fermi level is below the conduction band (CB) of about 0.2 eV (E_F = 6.9 eV) [150,173].

Given that the work function of MoO_3 is larger than the IE of most organic material used as hole transport layer (e.g. α-NPD as seen above has IE = 5.4 eV), electron transfer occurs from the organic material to the oxide at the heterojunction. Thus, Fermi level pinning arises between the CB of the oxide and the HOMO of the organic. Due to the small energy barrier between CB and HOMO, hole-injection into the hole

transport material proceeds via electron extraction from the organic HOMO, providing almost Ohmic contact [173,176,177].

3.2. Sample preparation techniques

A short overview of the techniques involved in sample preparation is presented in the following section.

In order to fabricate organic electronic devices, the π-conjugated materials must be deposited to obtain thin films. Two techniques are commonly used for the deposition process, depending on the nature of the treated materials:

- *thermal evaporation*, if the molecules are thermally stable they can be heated to the sublimation point. For this purpose, vacuum techniques must be employed. The vacuum condition allows for vapor particles to travel directly from the organic vapor source to the target object (substrate), where they condense into thin film. To keep the substrate clean and to reduce contamination in the growing film, UHV conditions are used (< 10^{-7} mbar);
- *solution processing*, in this case the molecules are in a dilute solution with a (usually volatile) solvent. A physical process is involved, in which the solvent is evaporated, leaving a film on the sample.

3.2.1. Molecular beam deposition

In Ultra Vacuum (UV) or Ultra High Vacuum (UHV) conditions, an evaporator cell, the so-called *Knudsen cell*, is usually used to produce the vapor beam of atoms or molecules to be deposited. The beam hits a substrate maintained at the desired temperature T_S. Gauging the temperature of the evaporation cell (T_E), the atomic/molecular beam flux can be controlled; in doing so, the deposition rate can also be controlled.

The process occurring at the surface can be summarized in four steps:

- *adsorption of the incoming molecular flux on the surface*. This is chemical in nature (chemisorption) when electron transfer occurs with consequent formation of strong bonds between molecules and the surface. If the process is driven mainly by van der Waals forces, physisorption occurs. See section 1.2.1 for further details.

- *migration* occurs when molecules from the vapor collide with the substrate surface, or when the growing film has enough energy to diffuse. Diffusion can occur on the layer itself (intra-layer) or between different layers (inter-layer);
- *incorporation* occurs when a molecule finds a suitable location and is completely integrated into the growing film;
- *desorption* occurs if the sticking energy of the molecule is insufficient for its cohesion.

The layer grows via one of the three modes illustrated in figure 1.4:

- *Frank-van der Merve* or *layer-by-layer*, where the substrate-molecule interaction is stronger than the one between the neighboring monolayers. Therefore, the first molecules form a closed monolayer on the substrate, before the second monolayer begins to nucleate (see Figure 3.4.a);
- *Volmer-Weber* or *island mode*, where the interaction between neighboring molecules (molecule-molecule) exceeds the interaction with the substrate (substrate-molecule). Therefore, small clusters nucleate on the surface, forming islands (see Figure 3.4.b);
- *Stranski-Krastanov* or *layer-plus-island*, an intermediate case where, after the formation of one or several complete monolayers, island formation will occur (see Figure 3.4.c).

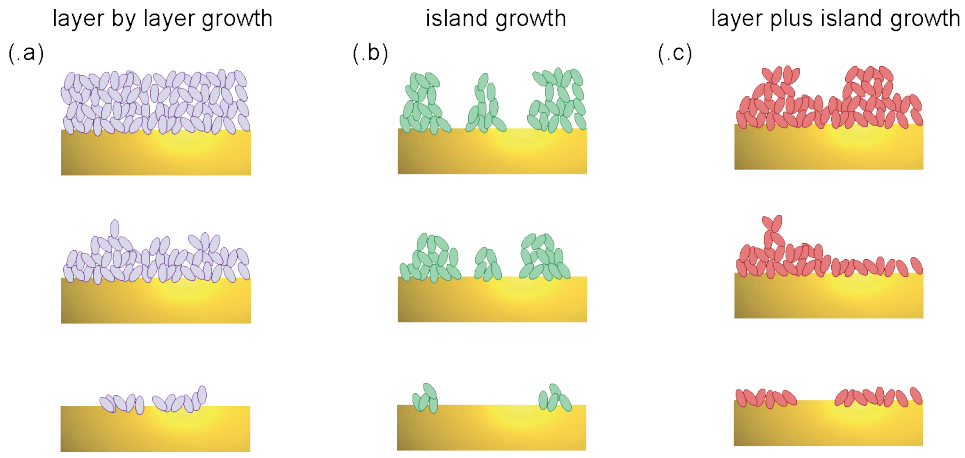

Figure 3.4. Cross-sectional view of the three growth models. In (.a) Frank-van der Marve or layer-by-layer growth model. In (.b) the Volmer-Weber or island growth model. In (.c) the Strasnki-Krastanov or layer-plus-island growth model.

3.2.2. Glancing angle deposition (GLAD)

Glancing angle deposition (GLAD) is a technique, which allows the tailoring of nanostructured morphologies through physical vapor deposition via controlling the substrate orientation, with respect to the vapor source direction.

When thin films are deposited onto stationary substrates under the condition of *oblique deposition*, meaning that the vapor flux is non-perpendicular ($0° < \alpha < 90°$, see Figure 3.5) to the substrate surface, an inclined columnar nanostructure is produced.

The process is due to the ballistic shadowing of the morphology of the surface and is amplified by the Volmer-Weber mode growth. The arrival of vapor flux and of the formation of film nucleation points is a random ballistic process. The nuclei grow into columns and develop shadows. As a result, some nuclei will screen neighboring nuclei from the incoming vapor flux, suppressing their growth. Given sufficient time, smaller columns can become completely shadowed and thus stop growing. This process, referred as *column extinction,* continues throughout the growth of a GLAD film. As the columns grow, more incoming vapor flux will be deposited on them. Eventually, only the top of the nuclei is able to grow, developing into columns tilted toward the vapor source. *Column tilt angle* is defined by the angle between the surface normal and the column's direction usually described by $\beta = \alpha - \arcsin\left(\frac{1-\cos\alpha}{2}\right)$.

Substrate orientation is defined by two angles, the above-mentioned *deposition angle* α and the *substrate rotation angle*, φ, which defines the azimuthal substrate position relative to an arbitrary starting position (see Figure 3.5). By continuously rotating the sample (at a constant angle α) during the film deposition, vertically oriented columns can be obtained ($\beta = 0°$).

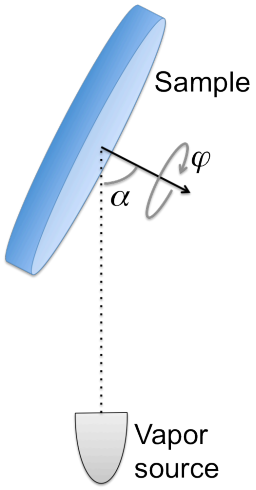

Figure 3.5. GLAD experimental setup.

3.2.3. Spin casting

Spin casting is a coating technique, which permits the application of evenly distributed thin film on different substrates (thickness from a few nm to a few μm) [178,179]. The typical procedure involves the coating of the substrate surface with droplets of ink, in which the material to be deposited is dissolved in a solvent. The sample is adjusted on a high speed rotor (usually > 1000 rpm). The centrifugal acceleration causes the ink solution to spread on the substrate surface, and the excess is rapidly ejected from the substrate, leaving a thin film on the surface. The final thickness, as well as the other film properties, depends on the solution mixture (e.g. viscosity, drying rate, surface tension) and on the parameters chosen for the deposition (e.g. initial acceleration, static rotational speed, spinning time).

Since spin casting is a more affordable and less time-consuming technology compared to other coating techniques (e.g. organic molecular deposition), it is currently the predominant technique employed to produce thin film with organic materials, i.e. polymer and large molecule semiconductors. On the other hand, one of the main problems with spin coating technology is its repeatability: subtle variations in the parameters that define the spin casting process can result in drastic variations on the coated film. The main steps of the spin coating process are outlined in the following section.

Substrate preparation

A clean process is the best way to guarantee that the film is deposited evenly. For this reason, spin casting is usually performed in cleanroom. The substrate surface is cleaned (mechanically with chemical solvent, acid and/or plasma etching or ozone treatment), in order to remove any contaminant that may change the surface tension of the substrate.

The sample is than placed on the spin stage, which consists of a programmable rotor. The substrate is fixed on the stage using the vacuum effect, as produced by a small vacuum pump.

Solution deposition

Solution deposition can be achieved by means of a nozzle that either pours the coating solution or sprays it onto the surface. In applying the ink solution, the quantity of the coating highly excess with respect to the amount that will ultimately be present in the

final coating film. It is often useful to dispense the substance using a sub-micron sized filter to eliminate particles that could lead to error.

Rotary acceleration

The rotor begins to accelerate from zero to the process's rotary speed. In this step, excess fluid is expelled from the sample surface by the rotational motion. Because of the initial depth of fluid on the surface, spiral vortices may be present during this stage. These are the result of the different inertia in the film layers. The expulsion of the excess fluid reduces the film's thickness, so that it becomes thin enough to rotate along with the wafer, and so any evidence of difference in fluid thickness dissipates.

Constant speed

The substrate spins in a constant speed, and the thickness of the film decreases gradually, leading to a uniform final coating (under ideal circumstances). The main goal of the process, once the uniform thickness is achieved, is the solvent evaporation.

Annealing

Once the spinning is stopped, many applications require that heat treatment or annealing of the coating be performed in order to completely remove the solvent.

3.3. Sample preparations and measurement details

The detailed sample preparation for the experiments will be illustrated in the following chapters according to the order in which they occurred in the experiment.

3.3.1. Samples for photoemission experiments

Molecules on metal

The molecule–on–metal experiments were performed using our laboratory's facilities. The interconnected preparation (base pressure 1×10^{-8} mbar) and analysis (base pressure 1×10^{-9} mbar) chambers enabled sample transfer without breaking ultrahigh vacuum (UHV) conditions.

The Au(111) single crystal was cleaned by repeated Ar^+ ions sputtering and annealing (up to 550 °C) cycles. XPS was used to verify the absence of contaminants (i.e. C, O, N) on the crystal surface. α-NPD and Alq_3 (both purchased from Sigma-Aldrich) were incrementally deposited in the preparation chamber (pressure during evaporation < 5×10^{-8} mbar) via sublimation from a resistively heated pinhole source on the Au(111) crystal surface. The mass-thickness of the molecules was monitored by a quartz microbalance (QCM). The evaporation rate for both α-NPD and Alq_3 was

approximately 0.1 Å/s (bulk density assumed 1.3 g/cm^3). Three different thickness regimes were chosen as experimental steps: submonolayer (SubML), monolayer (ML), and few monolayers (MultiL). After the evaporation of the molecules, the sample was transferred into the analysis chamber for XPS analysis.

The spectra were collected in normal emission geometry with a hemispherical electron energy analyzer (Omicron EA125), with an energy resolution < 150 meV at 20 eV pass energy. C1s, N1s, O1s, and Au4f core levels were collected using a non-monochromatized Al Kα photon source (1486.6eV).

The XPS spectra analyses were performed by background subtraction of a Shirley function and Voigt lineshape deconvolution. In the following chapter, the XPS experimental data are displayed as scattered gray lines (normalized to constant intensity for the purpose of comparison), while the solid black lines represent the sum of the single fitting components (colored lines).

For the sake of being thorough, we repeated the deposition of the organic molecules also on the Au crystal, directly after sputtering, i.e. skipping the surface reconstruction (in the following indicated as AuSput), in order to measure any different chemical interactions induced from surface defects or dangling-bonds.

Metal NPs on Molecules

The AuNPs-on-molecule experiments were carried out at the end-station SurICat (beamline PM4) at the synchrotron light source BESSY II (Berlin, Germany). The UHV system consists of an interconnected preparation (base pressure 5×10^{-9} mbar) and analysis (base pressure 5×10^{-10} mbar) chambers.

α-NPD and Alq_3 were sublimated from resistively heated pinhole sources onto indium tin oxide (ITO) coated glass. The ITO substrates were previously cleaned by sequential sonication in acetone and isopropyl alcohol. The thickness for both films was 400 Å (evaporation rate ca. 0.1 Å/s, monitored with QCM), enough to avoid any substrate contribution in the sample surface photoemisison signal. After the PES characterization of the pristine molecule films, an increased amount of gold was stepwise evaporated on top of the pristine molecule films in the preparation chamber (pressure during evaporation < 1×10^{-8} mbar) by means of an electron beam evaporator, leading to the formation of AuNPs. The evaporation rate was monitored with a QCM and measured about 0.01Å/s. PES analysis was performed in the analysis chamber, consecutively after each evaporation step.

The spectra were collected at normal emission with respect to the hemispherical electron energy analyzer (Scienta SES 100).

For the UPS characterization, the photon energy was set at 35 eV. The resolution for UPS measurement is 150 meV. For the XPS characterization, the excitation energies used for recording the C1s, N1s, O1s, and Au4f core levels were 390 eV, 503 eV, 636 eV, and 213 eV, respectively, in order to achieve the same photoelectron escape depth of ~ 1nm. Binding energies (BEs) of core levels were attributed to the $Au4f_{7/2}$ line (84.0 eV) of a clean Au foil reference. The resolution resulted in 120 meV energy resolution at 20 eV pass energy.

3.3.2. Devices experiments

The hole-only devices were prepared on 1×1-inch glass substrates with a patterned indium-tin-oxide electrode (hereafter referred to as ITO/glass). Before patterning, tape film was applied to preserve the ITO coating needed for the experiment. To perform the patterning, the ITO/glass was immersed in a solution of HCl (38 %) for 12 minutes for etching. The substrates were repeatedly rinsed in de-ionized water for 10 cycles. The protective tape was removed; any traces of tape residue were removed by brushing with acetone. ITO resistivity was verified (pristine ITO ~ 20 Ω, etched ITO ~ 50 kΩ).

The (patterned) ITO/glass substrates were cleaned by sequential sonication in acetone, detergent, de-ionized water and isopropyl alcohol, before further oxygen plasma treatment was applied (200 W for 3 minutes). The transparent electrode surface was coated with ~ 50 nm layer of hole conductive polymer PEDOT:PSS (Clevios AI 4083) via spin-casting (30 s at 1500 rpm). The substrates were then transferred to a nitrogen filled glove box and annealed at 180°C for 10 minutes. Without air exposure, two substrates were introduced in a high vacuum (HV, base pressure 1×10^{-6} mbar) preparation chamber. The preparation of the two samples progressed simultaneously in five steps:

(i) 60 nm of the hole conductive molecule (α-NPD, Sigma Aldrich) were sublimated on both samples;

(ii) on one sample, AuNPs were deposited by thermal evaporation, while the other was kept masked (sample used as reference);

(iii) 60 nm of α-NPD were sublimated on both samples;

(iv) 10 nm MoOx thermally evaporated;

(v) 100 nm gold were thermally evaporated through shadow mask to define the device-pixel area as 0.15 cm^2 (10 pixels produced on each substrate).

The entire process was carried out without breaking the vacuum; depositing rates were controlled by the evaporation source temperature and were monitored by a quartz crystal microbalance (QCM).

A modified device was also fabricated. On the same bottom electrode PEDOT:PSS/ITO/glass, a layer of α-NPD was deposited with the same nominal thickness (120 nm) as the previous devices. The device was fabricated without inserting any metal NPs interlayer within the α-NPD film (NPs-free). The top contact was fabricated with deposition of 100 nm of Al. The same shadow mask was employed (i.e. device-pixel area to be 0.15 cm^2). Figure 3.7 illustrates the device.

After the preparation of the devices, they were introduced, without air exposure, into a nitrogen-filled glove box for electrical characterization. There, current density vs. bias (J-U) curves were measured with a computer-controlled Keithley 2400 source matter, at room temperature. All J-U curves were acquired with a continuous bias sweep. Before recording the J-U curves, the devices were electrically conditioned by means of the following series of bias sweeps:

- 10 x sweep from 0 V to - 1 V;
- 10 x sweep from 0 V to - 2 V;
- 10 x sweep from 0 V to 1 V;
- 10 x sweep from 0 V to 2 V.

The J-U curve measurements discussed in the following Chapter 7 were carried out in three different illumination conditions:

- dark;
- illuminated with a red (685 nm) laser;
- illuminated with a blue (405 nm) laser.

The laser beams were broad enough to illuminate the entire measured device. The power density for both sources was ~ 0.05 mW cm^{-2}.

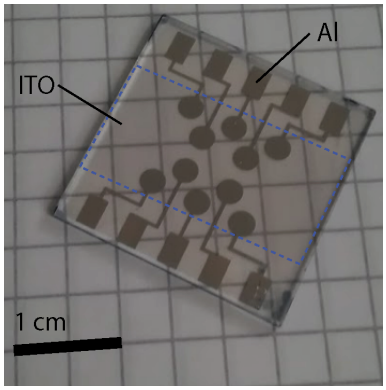

Figure 3.7. Pictured is the Al/NPD/PEDOT:PSS/ITO device. Al electrode is on the top contact. The dashed line represents the region coated with ITO.

3.3.3. Nano-structured devices experiments

The samples were prepared via sublimation α-NPD via GLAD onto ITO/glass and Ag-coated ITO/glass substrates at room temperature and in UHV condition. ITO substrates were cleaned supersonically in acetone, ethanol, and de-ionized water and were mounted on a sample holder attached to a computer-controlled stepper motor. This allowed for sample rotation about the substrate normal in a custom UHV chamber (base pressure base pressure 1×10^{-7} mbar). The Ag film was evaporated on clean ITO/glass in the same UHV chamber by means of electron beam evaporator (EBE) on ITO. The evaporation rate was about 0.2 Å/s. The ITO/glass was kept in normal incidence with respect to the Ag vapor. The substrate was kept in rotation for the sake of film uniformity.

α-NPD was sublimated from an effusion of cells in a condition of glancing angle deposition (GLAD). The substrate relative to the incoming molecular flux was adjusted by a precision rotary motion feedthrough. The substrate rotation speed was monitored by the above-mentioned computer. The deposited mass thickness was monitored by a quartz crystal microbalance. The deposition rate at the substrate was kept at about 1.0 Å/s.

Atomic force microscopy (AFM) and scanning electron microscopy (SEM) were used to investigate the morphology of the resulting samples. C-AFM was employed for the electrical characterization of the samples in air and at room temperature.

Chapter 4. Chemical properties of organic semiconductors/metal nanoparticles systems

4.1. Overview

As previously discussed in the introduction and in Chapter 3, the architecture of organic non-volatile memory (NVM) devices, which we decided to adopt for our investigations, consists of an hybrid organic/inorganic material: in which metal nanoparticles (MNPs) are imbedded in organic semiconductors, forming a well-defined interlayer. Since metals exhibit completely dissimilar behaviors, when their size is reduced to the nanometer scale as an effect of electron confinement in the nanoclusters, it is important to understand the nature of the interaction between the organic hosting material and the MNPs.

This chapter reports the investigations on the size-induced interactions between the conjugated small molecules chosen for the realization of NVMs in this work – the hole-transport molecule 4,4-bis[N-(1-naphthyl)-N-phenyl-amino]diphenyl (α-NPD) and the electron-transport molecule tris-(8-hydroxyquinoline)-aluminum (Alq_3) – with a generally inert metallic element, gold (Au). In fact, although bulk Au is generally known as a poorly reactive element (e.g. Au surfaces do not chemisorb many molecules easily) [180], it has proven to be quite active in form of NPs for catalytic reactions, such as (low temperature) CO and CO_2 oxidation [181,182] or NO reduction [183].

In the following section, an X-ray photoemission spectroscopy (XPS) investigation of the interface between organic molecules (both α-NPD and Alq_3) and gold nanoparticles (AuNPs) will be presented. For the sake of comparison, the AuNPs-on-molecule experiments will be compared with the reversed molecule-on-Au.
The results presented in this chapter are based on the article recently published in the peer-reviewed international journal ChemPhysChem [38].

4.2. Results and discussion

First, the chemical interaction between the molecules α-NPD and Alq_3 on Au were investigated. For this purpose, the organic semiconductor molecules were deposited in a step-by-step manner on a clean Au(111) single crystal. After the deposition of molecules, the sample was measured by mean of XPS. Three different thickness regimes were chosen as experimental steps: submonolayer (SubML), monolayer (ML), and a few monolayers (MultiL).
The XPS spectra analyses were performed by background subtraction (estimated by Shirley function) and lineshape deconvolution in Voigt peaks. In the following section, the XPS experimental data are displayed as scattered lines, while the solid black lines represent the sum of the fit components (colored line). For the sake of comparison, all the spectra have been normalized to constant intensity.

4.2.1. Molecules on metal

A. α-NPD on Au(111)

Figure 4.1 depicts the chemical structure of α-NPD molecule with the identification of the carbon atoms for the fit (C atoms are identified only on half of the molecule's structure for reasons of symmetry). Figure 4.2 displays the evolution of C1s, N1s, and Au4f core level spectra as a function of increasing amount of α-NPD molecule on the Au(111) substrate (in Figure 4.2.a, a schematic of the sample structure). The bottommost curve in each set represents the pristine substrate. The C1s core level, which appears after deposition of α-NPD, has been deconvoluted in two Voigt peaks (see Figure 4.2.b). The main component, located at lower binding energy, corresponds to C-C specie (C atoms 5, 10, 20 in Figure 4.1) and C-H specie (C atoms 2-4, 6-9, 12-16, 18-19, 21-22). Since these two single components cannot be resolved, we refer to the

superposition component as C-X (the red curve in the spectra in Figure 4.2.b); while the one at higher binding energy is related to C-N (the blue curve in the spectra).

The spectral weight ratio (i.e. the ratio of the area under C-N peak and C-X peak) is 3:19, in excellent agreement with the molecule stoichiometry (C-N:C-X ratio 3:19). At SubML regime, the C-X component is located at 283.8 eV, while the C-N component is at 284.8 eV. With an increasing amount of molecules on the Au(111) surface, the C-X peak shifts toward higher binding energy (+ 0.6 eV in the MultiL regime), while the relative energy shift between C-X and C-N does not change (+ 1.0 eV).

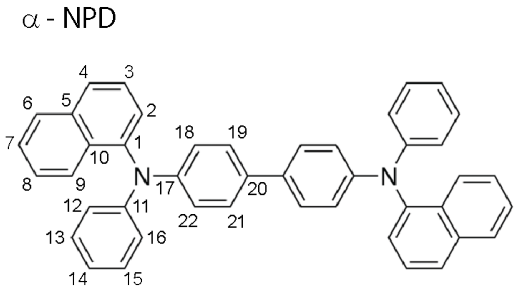

Figure 4.1. Chemical structure of the α-NPD molecule. The C atoms are identified.

The peak broadening (quantified by full width at half maximum, FWHM) remains substantially constant during the deposition sequence, results for both carbon species C-X and C-N, ~ 1.2 eV).

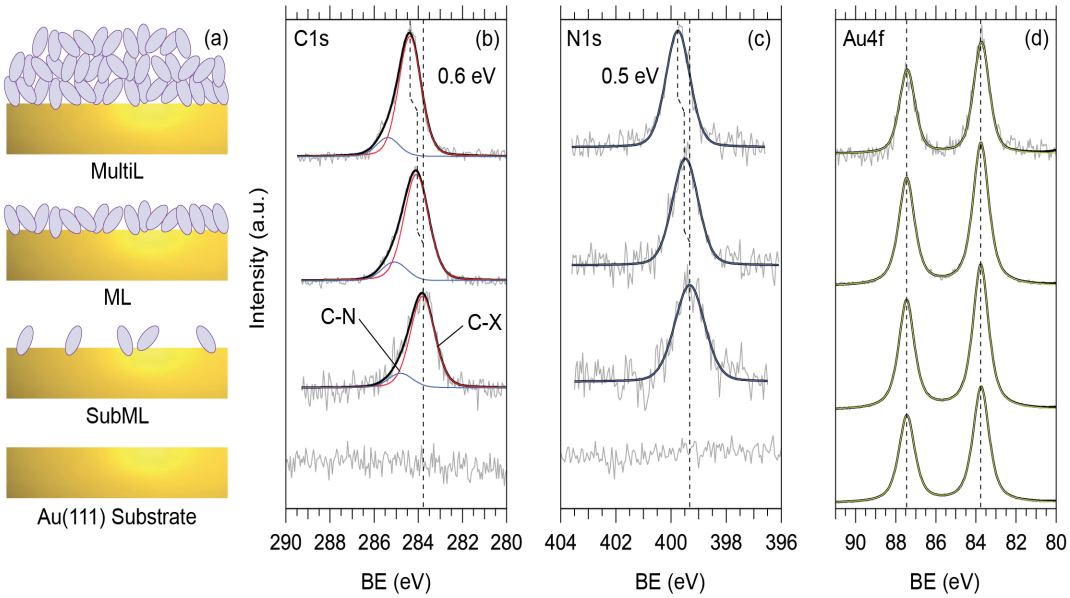

Figure 4.2. Core level evolution as a function of an increasing amount of α-NPD on Au(111) single crystal. The schematic illustration in .a depicts the different thickness regime.

In the N1s core level spectra (Figure 4.2.c), one symmetric component is resolved. This reflects the presence of only one chemical configuration for this species. The peak is located at 399.3 eV for the SubML regime and shifts about + 0.5 eV for the MultiL regime, consistent with the shift observed in the C1s spectra. FWHM slightly decreases after the formation of the first ML (1.3 eV for SubML, and 1.1 eV for ML and MultiL).

The Au4f core level does not exhibit any change upon α-NPD growth, as shown in Figure 4.2.d (except for the decrease in intensity due to screnning of the overlayer), neither in the energy position (the $Au4f_{5/2}$ and $Au4f_{7/2}$ lines are at 83.8 eV and 87.5 eV, respectively) nor in broadening (FWHM is consistently 0.95 eV).

It is noteworthy that, due to the excitation energy of the X-ray Al source employed (1486.6 eV), the Au4f signal is not sensitive to the surface and is stem mainly from the bulk crystal (photoelectron escape depth ~ 26 Å) [184]. Therefore, the Au4f core level cannot likely be used as an indicator for strong physical or chemical interactions between an α-NPD and the Au(111) surface. We can nevertheless rule out the possibility of strong interactions by the absence of substantial changes (e.g. new features especially in the SubML) in the C1s and N1s core levels. The tendency of α-NPD to form weak interactions with the substrate has already been reported, e.g. on Si, ITO and Ag(111) [180,185,186].

The observed energy shift in the C1s and N1s core levels between the SubML and MultiL regime has been attributed to photo-hole screening effects (final-state), more efficient at lower coverage (hole partially screened by the Au substrate) than at higher coverage [113].

We also find consistent results for α-NPD evaporated on the Au_{Sput} surface (see Figure 4.3). This suggests that neither surface defects nor dangling bonds (schematically represented as surface with defects in Figure 4.3.d) can induce any reactivity between α-NPD and the underlying Au substrate.

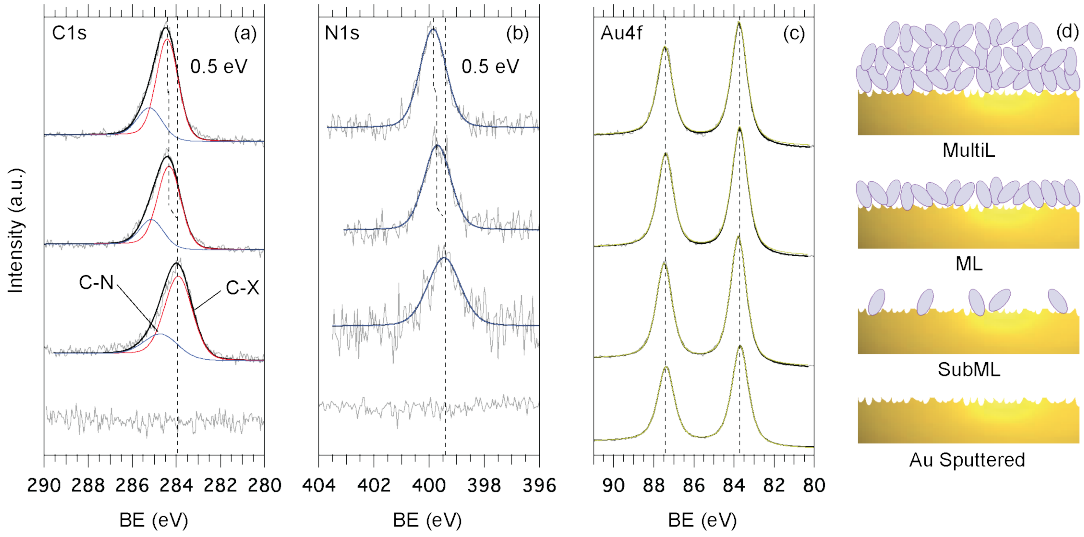

Figure 4.3. Core level evolution as a function of an increasing amount of α-NPD on sputtered Au single crystal. The schematic illustration in .d depicts the different thickness regime on the Au schematically represented with surface' defects induced by the sputtering.

B. Alq_3 on Au(111)

Figure 4.4 depicts the structure of the Alq_3 molecule, identifying C atoms on which the following analysis is based. The evolution of C1s, N1s, O1s and Au4f core level spectra as a function of the increasing amount of Alq_3 on Au(111) is displayed in Figure 4.5. For a schematic representation of the experimental steps, see Figure 4.2.a. The C1s core level (see Figure 4.5.a), after deposition on Alq_3, has been deconvoluted into five components in accordance with the theoretical model (based on density functional theory, DFT) proposed by Bisti et. al [187]. DFT calculation predicts a non-degeneration of the binding energies, neither for the different C-H carbon atoms. For this reason, we associated the five fit components to different carbon species (from higher to lower binding energy, respectively) C-O (C atom 8 in Figure 4.4), C-N (1, 9), C-C (4), C-H* (2), and the other four C-H (3, 5-7) carbon atoms, which are further away from the N atom.

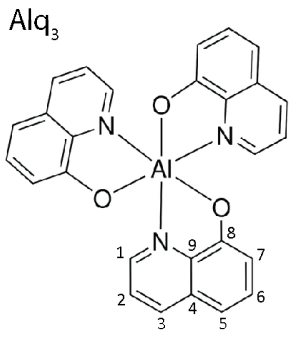

Figure 4.4. Chemical structure of the Alq_3 molecule. The C atoms are identified.

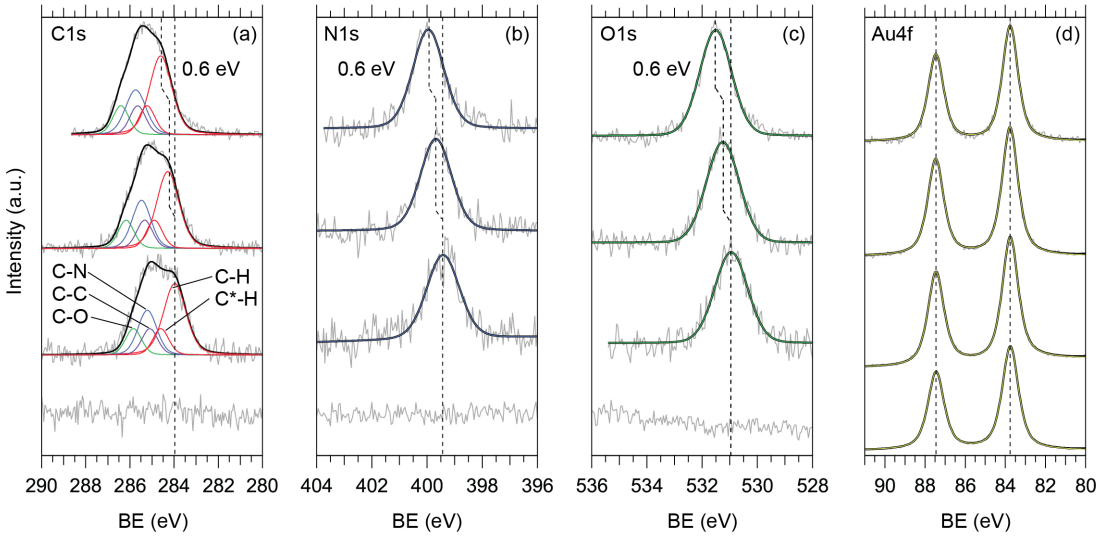

Figure 4.5. The evolution of C1s (in a), N1s (b), O1s (c), and Au4f (d) core levels as a function of the increasing amount of Alq_3 on Au(111).

In accordance with this molecule description and the stoichiometry, the components area ratio C-O:C-N:C-C:C-H*:C-H is 1:2:1:1:4, respectively.

The relative energy shift between C-O, C-N, C-C, and C-H* components from the main C-H peak are + 1.8 eV, + 1.15 eV, + 1.05 eV, and + 0.6 eV, respectively. As already seen for the α-NPD on Au(111) in Figure 1.a, the C1s main peak for the Alq_3 on Au(111) in Figure 4.2.b shifts towards higher BE of 0.6 eV (from 284.0 eV for SubML to 284.6 eV for MultiL), while relative distances and peaks in/of FWHM do not display any substantial evolution.

For N1s and O1s spectra (Figure 4.5.b and Figure 4.5.c, respectively), one main component (SubML starting positions 399.4 eV and 530.9 eV, respectively; FWHM ~ 1.3 eV for both core levels) is resolved, i.e. only one bonding configuration for these species is assumed. Increasing the molecule amount on the surface, N1s and O1s peaks also display an energy shift of 0.6 eV towards higher BE (as seen previously in the C1s spectra). As in the case of the α-NPD–on–Au(111) system, the shifts of the core levels are referred to as final-state photo-hole screening processes.

The Au4f core level, as shown in Figure 4.5.d, does not show any evolution with the increasing amount of molecule: the Au4f5/2 and Au4f7/2 core level peaks are located at 83.8 eV and 87.5 eV, respectively, and no broadening is observed (FWHM ~ 0.9 eV).

Also, for the Alq_3–on–Au(111) system, the absence of any additional features and peaks broadening (especially at SubML stage) rules out chemical or strong physical interaction with the Au(111) surface.

Results consistent with this outcome have been found for Alq_3 evaporated on Au_{Sput} surface, as well. Figure 4.6 displays the evolution of C1s, N1s, O1s and Au4f core level spectra as a function of the increasing amount of Alq_3 on a sputtered Au(111) surface.

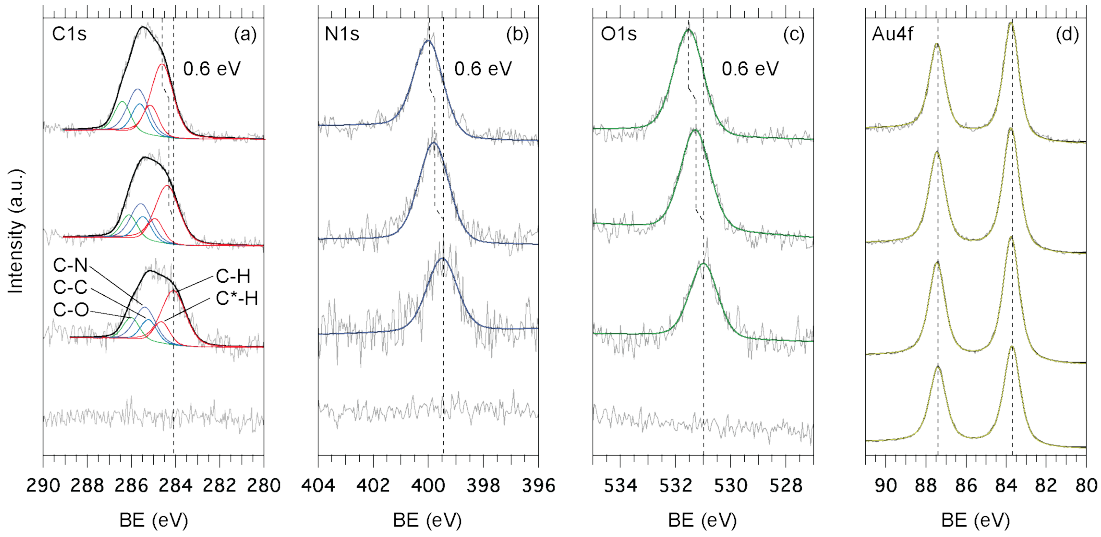

Figure 4.6. The evolution of C1s (in a), N1s (b), O1s (c), and Au4f (d) core levels as a function of the increasing amount of Alq_3 on Au surface directly after sputtering.

4.2.2. Metal NPs on molecules – TEM investigation

In the following section, we will report on the deposition of AuNPs on pristine α-NPD and Alq_3 molecular films. AuNPs are generated from gold thermal deposition onto the organic semiconductors. As a matte of fact, Au evaporation at a low coverage regime and at a low evaporation rate does not form homogeneous compact metallic films, but leads to the formation of NPs, instead [188,189]. To achieve low deposition rate (< 0.01 Å/s) in a controlled way for an extended period of time, electron beam evaporated was employed.

A series of equivalent samples (i.e. fabricated in the same evaporation condition, with respect to those investigated via photoemission spectroscopy) were examined by transmission electron microscopy (TEM). The purpose was to study the generation of AuNPs and to probe how statistical parameters, such as size of NPs, particle-particle

distance, and NPs density, are correlated to the total amount of Au evaporated (mass-thickness Θ_{Au}).

Figure 4.7 shows a comparison between two samples with different nominal evaporated Au mass-thickness (Θ_{Au}) deposited on Alq_3. Figure 4.7.a and Figure 4.7.b are bright-field TEM images (*xy*-plane, see Figure 4.7.f for the sample orientation with respect to the TEM set-up) of the samples. The topmost images refer to the Θ_{Au} = 0.3 Å sample, while the bottommost refer to 3.0 Å, respectively.

At subnanometer coverage regime, Au does not grow homogeneously in a compact metallic film, but forms nanoparticles (NPs) [188] as depicted in Figure 4.7.a and .c.

In order to investigate the interdiffusion of NPs into the organic bulk, a series of images (*xy*-planes) with different tilt (*rocking*) angles were acquired.

Figure 4.7.b and Figure 4.7.d show the projection of cross sectional images (*yz*-plane) that were reconstructed from the tilt series for both samples with Θ_{Au} = 0.3 Å and 3.0 Å, respectively. The images clearly demonstrate that AuNPs are on the same plane orthogonal to the cross section plane, and that no percolation occurs in the organic matrix.

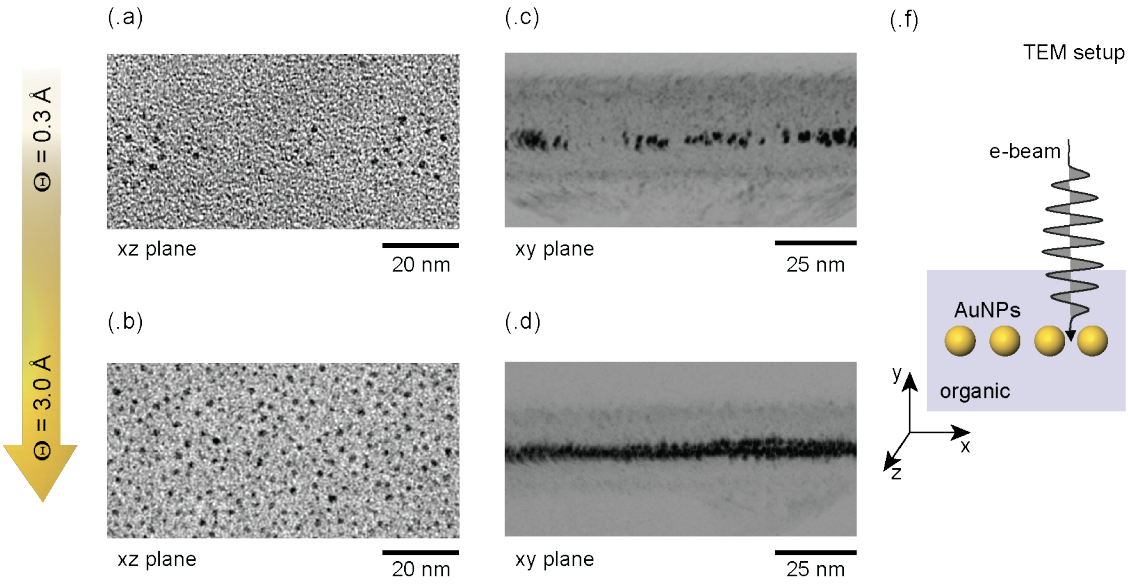

Figure 4.7. TEM investigation of AuNPs on Alq_3. Topmost pictures refer to the sample with 0.3 Å Au mass-thickness, while bottommost curve to sample with 3.0 Å Au mass-thickness. Figure (.a) and (.b) are the top-view images (*xz*-plane). Figure (.c) and (.d) are cross-sectional images (*xy*-plane). Figure (.f) reports the orientation of the sample see from the side with respect to the electron beam of TEM.

Results consistent with these have been found for the α-NPD/Au samples. Likewise, Au does not grow as a homogeneous film on α-NPD at subnanometer coverage regime, and the NPs layer is formed at the organic surface. For both Alq_3 and α-NPD, the subsequent growth of the second organic layer on the top of the NPs interlayer appears to be compact and homogeneous.

For both α-NPD/AuNPs and Alq_3/AuNPs system, statistical analysis shows that Θ_{Au} is correlated with the average particle diameter (d_{AuNPs}), particle-particle distance calculated with statistical autocorrelation function ($\lambda_{NP\text{-}NP}$, autocorrelation peak defined only for sample Θ_{Au} = 3.0 Å) and number of NPs per surface unit (σ_{AuNP}). Figure 4.8 shows the histogram of AuNPs dimension population for the α-NPD/AuNPs system (.a and .b) and the Alq_3/AuNPs (.c and .d) for increasing amount of Au mass-thickness.

Statistical analysis on the sample series shows that in increasing the nominal mass-thickness Θ_{Au}, the number of particles per surface unit (σ_{AuNPs}) and the average particle diameter (d_{AuNP}) grow as well. Only for higher AuNPs coverage it is possible to calculate the particle-particle autocorrelation function ($\lambda_{NP\text{-}NP}$). The results of statistical analysis are summarized in Table 4.1.

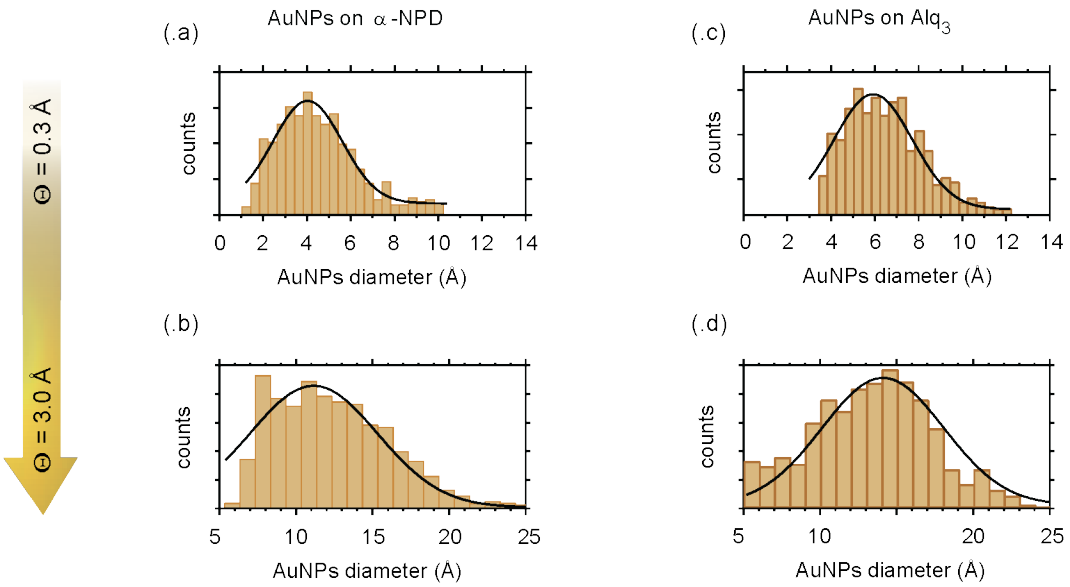

Figure 4.8. Histograms of AuNPs populations. Topmost curves refer to sample with 0.3 Å Au mass-thickness for α-NPD and Alq_3 in (.a) and (.c), respectively. Similarly, bottommost curves refer to the sample with 3.0 Å Au mass-thickness.

Table 4.1. TEM statistical analysis results regarding average particle diameter (d_{AuNPs}), particle-particle distance ($\lambda_{NP\text{-}NP}$), and number of NPs per surface unit (σ_{AuNPs}) for samples with different nominal Au mass-thicknesses Θ_{Au}.

	α-NPD			Alq_3		
Θ_{Au}	d_{AuNP}	$\lambda_{NP\text{-}NP}$	σ_{AuNPs}	d_{AuNP}	$\lambda_{NP\text{-}NP}$	σ_{AuNPs}
(Å)	(Å)	(Å)	(NPs/100 nm²)	(Å)	(Å)	(NPs/100 nm²)
0.3	6 ± 3	-	>1	4 ± 3	-	>1
1.0	11 ± 3	21	5	8 ± 3	-	2
3.0	14 ± 3	27	12	11 ± 3	33	8

4.2.3. Metal NPs on molecules – PES investigation

C. AuNPs on α-NPD

Figure 4.9 displays the evolution of C1s, N1s and Au4f core level spectra collected at normal emission with excitation energies 390 eV, 503 eV and 213 eV, respectively. In Figure 4.9.a the C1s core levels can be fitted with the same model proposed in the reversed α-NPD–on–Au experiment. Two components are found: one at lower BE reflecting the C-H/C-C carbon atoms (indicated as C-X), and one at higher BE for the C-N carbon.

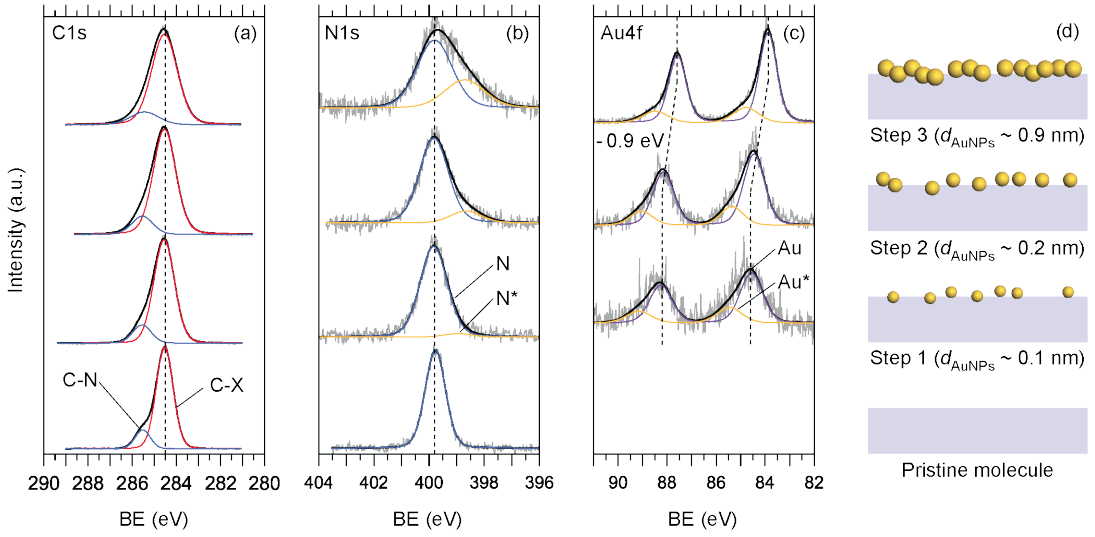

Figure 4.9. Evolution of C1s (.a), N1s (.b), Au4f (.c) core levels as a function of the increasing amount of AuNPs on a-NPD. The schematic of the measured samples is depicted in the right illustration (.d).

On the contrary, the fit of the N1s spectra (Figure 4.9.b) with one single component (like previously done, see Figure 4.2.b) does not yield to satisfactory results once AuNPs are deposited on the molecular surface. As a matter of fact, a new feature N* appears to evolve on the lower binding energy side of the main peak (Δ BE = - 1.2 eV). The area ratio between the main peak N (BE = 399.8 eV) and the new N* component (BE = 398.6 eV) increases with the AuNPs deposition.

While C1s and N1s peaks do not display any energy shift, the main components of the Au4f core level (see Figure 4.9.c, i.e. $Au4f_{7/2}$) are positioned at 84.9 eV in the earliest stage of deposition, but shift towards lower binding energies as a function of the AuNPs amount (see the illustration of the samples Figure 4.9.d). The bulk value (BE = 83.9 eV) is reached at the maximum coverage, which corresponds to an interconnected AuNPs network with metallic characteristics (i.e. existence of a "quasi"-Fermi edge) in the valence band region.

Figure 4.10 reports the photoemission spectra in the valence band regions for the two investigated systems, before the AuNPs deposition (black lines are the measurements of the pristine molecules) and after (gold lines). Refer to Chapter 5 for more details on the valence band region.

It is well known that the core level shift towards higher binding energy is dependent on the shrinking of the NPs size [190–194]. For metal NPs deposited on insulators or semiconductors, the photo-hole is poorly screened by the surrounding matrix, since the relaxation of the photo-hole is delayed compared to the time scale of the photoemission of the electrons.

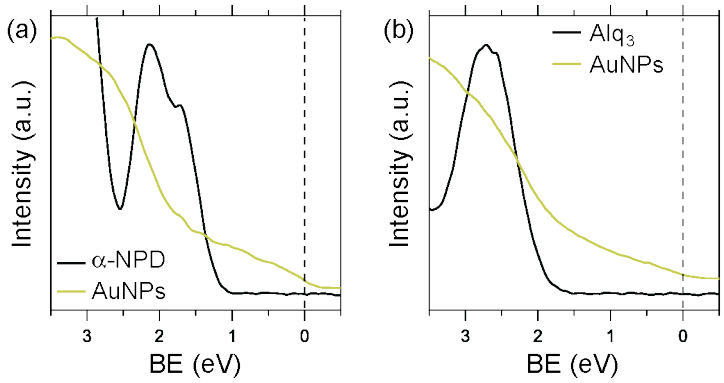

Figure 4.10. Valence band region spectra of pristine molecular films (black lines), and after AuNPs deposition (gold line) for α-NPD (in .a) and for Alq_3 (in .b).

In fact, using 213 eV as excitation energy, an electron from the Au4f core level has a kinetic energy of about 130 eV, which corresponds to 6.7×10^6 m/s,[13] thus sensitive to femtosecond process (considering the time necessary to tread a distance equal to few NPs diameters ~nm). This leads to a positive charging of the NPs during the photoemission process, with consequent Coulomb interaction between the (charged) NPs and the photo-electron (final-state effect). The kinetic energy of the photo-emitted electron is thus reduced (increasing the experimentally measured binding energy). The shifts to higher binding energy are observed for metal NPs smaller than about 5 nm [195].

The energy shift of the measured BE can be approximately estimated by modeling the AuNP as charged spherical capacitor (with radius $d/2$ in nm) and considering the energy required to remove an electron from it; thus

$$\Delta \text{ BE (eV)} = \frac{1}{4\pi\varepsilon_0\varepsilon_r}\frac{e^2}{d} = \frac{1.44}{\varepsilon_r}\frac{1}{d}; \qquad \text{(Eq. 4.1)}$$

where e is the electron charge, ε_r is the vacuum permittivity, and ε_0 is the relative permittivity of the surrounding matrix.

For the sake of comprehension, we report the position of the $Au4f_{7/2}$ peak, with respect to the diameter d of deposited AuNPs, in Figure 4.11, the indicated NPs sizes are estimated from the TEM investigation. The purpose of the graph is to verify the $1/d$ dependency on the energy shift.

The black curve is the fit according to the previous equation and gives a relative dielectric constant $\varepsilon_r \sim 11$ for this system.

The discrepancy between the value commonly reported in literature ($\varepsilon_r \sim 3$) and the calculated value is acceptable for this simplistic model.

---

[13] Knowing the excitation energy (213 eV), one can calculate the speed of the photo-electron. The kinetic energy of an electron is given by the relation

$$E_k = (\gamma - 1)E_0 \text{ and } \gamma = \frac{1}{\sqrt{1-{v^2}/{c^2}}};$$

where E_0 is the rest energy of an electron (E_0=0.511 MeV), thus, $\gamma = 1 + E_k/E_0$. Therefore the velocity of an electron is given by $v = c \cdot \sqrt{1 - 1/\gamma^2}$. If the photoenergy of the electron is 130 eV ($\gamma = 1.00023$), the corresponding velocity is 6.7×10^6 m/s.

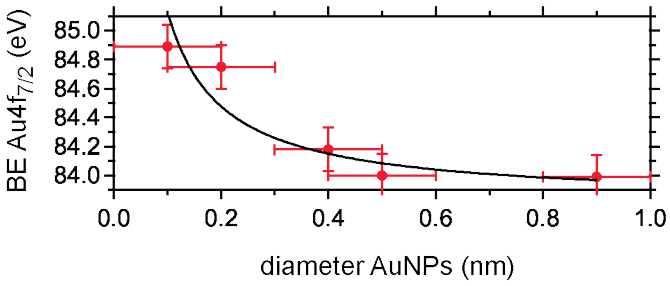

Figure 4.11. $Au4f_{7/2}$ BE as a function of the diameter of AuNPs, according to the TEM investigation.

As shown in Figure 4.9.c, the Au4f peak exhibits asymmetry, and the spectra can be fitted with an additional component at higher BE with respect to the main peak (BE = 85.7 eV). Some authors associate this asymmetry of the core level peak with final-state effects, due to NPs populations that are smaller than average in size (which affects the position of the main peak) [195,196].

Unlikely, such a large shift (+ 1.7 eV with respect to the bulk peak, BE = 84.0 eV) could only be originated by final-state effects; DiCenzo et. al. measured for extremely small AuNPs (with n = 5 Au atoms) an energy shift of about 1 eV from the bulk peak (84.0 eV) [194].

In the system reported here, changes in the electronic configuration of the system occur independently from the applied spectroscopic techniques; therefore, both initial-state and final-state effects play a role in the spectra energy shifts.

The shape of our spectra required the fitting of the lineshape with a new component (Au*) that is located at 85.7 eV, for the first AuNPs deposited-step here reported. Furthermore, as previously mentioned, the N1s in Figure 4.9.b exhibits the presence of a new feature (N*) at lower BE, associated with the negative charge accumulated in some of the N atoms, and therefore with a new chemical (electronic) configuration. Accordingly, the Au* component of the Au4f spectra, positioned at higher binding energy (+ 0.9 eV) with respect to the main component, indicates a higher oxidation state (i.e. more positively charge) for the Au specie. The opposite direction of the chemical shifts in N1s and Au4f core levels, respectively, suggests a net charge transfer (CT) from the AuNPs to the molecules, which, in combination with the additional discrete electronic levels characterizing the AuNPs (size effects), leads to the

formation of new, strongly-bound chemical species, indicated in the following as organo-metallic complex.

All molecular core levels broaden substantially during the deposition sequence and FWHM increases (~ 0.6 eV for C1s, and ~ 0.8 eV for N1s), while the FWHM of the Au4f main peak (related to the cluster size distribution) continuously decreases (from 1.2 eV to 0.8 eV). The increment of the C1s and N1s FWHM is due to the increasing amount of AuNPs on the surface, with consequent formation of different screened regions, where the atoms might experience different local potentials.

Therefore, the system AuNPs–on–α-NPD shows a chemical reactivity between Au and the molecules that was not observed in the reversed α-NPD–on–Au. The clear electronic CT between Au and N atoms – especially at lower Au coverage (i.e. smaller AuNPs size, the presence of which is demonstrated by the ΔBE of the Au4f peak) – shows the different physical-chemical interaction between the α-NPD and Au, once the size of the metal compound is scaled to nanosize dimensions. The special confinement of the electronic structure in NPs affects the energy level distribution with the formation of the organo-metallic complex.

D. AuNPs on Alq_3

Figure 4.12 shows the C1s, N1s, O1s and Au4f core levels spectra as a function of incremental amount of AuNPs deposited on Alq_3. For the pristine molecule, the C1s, N1s and O1s core levels fits are consistent with the ones proposed in the reversed Alq_3-on-Au experiment (see Figure 4.5). Once AuNPs are deposited on the molecular surface, important changes occur to all the molecular core levels (C1s, N1s and O1s). C1s exhibits a significant spectra broadening evolution on the higher BE side, even though the single 5 components do not show a substantial increase of the FWHM, the C-O, and the C-N components shifts to higher binding energy, consistent with the Au amount. The shifting of the C-O and C-N reflects the changes to electronic configuration occurring in the molecule.

Au deposition leads, in fact, to the formation of a lower BE component in N1s core level (- 1.0 eV from the main peak for both core levels), indicated as N* (see Figure 3.6.b). A substantial broadening is observed in the N1s and O1s spectra as well, while no energy shifts occurs. O1s spectra do not exhibit any asymmetry (or formation of new features) indicating, therefore, the presence of only one atomic configuration.

A new feature lies at higher BE (+ 0.9 eV) with respect to the main peak in the Au4f spectra (referred as Au*), indicating a charge transfer from this molecule to the AuNPs.

As in the previous case (AuNPs–on–α-NPD), the chemical shift of the Au4f spectra from the Au4f in the bulk is attributed to both initial- and final-state effects. Charge transfer between AuNPs and the Alq3 molecules leads the formation of new, strongly-bound chemical species (i.e. the metal-organic complex).

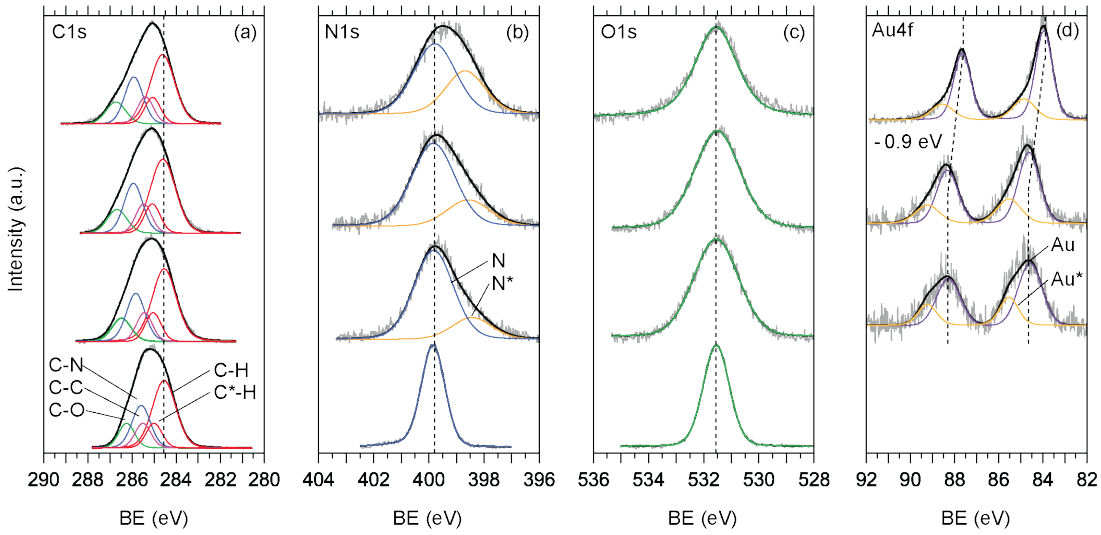

Figure 4.12. Evolution of C1s (.a), N1s (.b), O1s (.c) and Au4f (.d) core level as a function of the incremental deposition of AuNPs on Alq3.

4.3. Summary

The effects of nanoscaled gold particles on both surfaces of α-NPD and Alq_3 molecular films were investigated via XPS. The AuNPs-on-molecule experiments were compared with the inverted configuration molecule-on-Au. In the latter case, no strong interaction was measured for both molecular systems. On the contrary, we found that for both α-NPD and Alq_3 material, a chemical interaction occurs, once the size of deposited metal is within the nanometric scale, with a consequently different electronic redistribution with respect to the Au bulk. The charge transfer, between molecules and new, discrete electronic structure stated in the metal NPs, leads to the formation of a strongly-bound organo-metallic complex.

Chapter 5. Electronic properties of organic semiconductors/metal nanoparticles systems

5.1. Overview

As seen in section 1.5, much of the literature addresses the working mechanism of resistive organic non-volatile memory devices to charging/discharging process of metal NPs hosted in organic materials [29,30,94,103,197–201]. This chapter focuses on the electronic structure of the interfaces of such hybrid organic/inorganic materials. More specifically, the focus is on the AuNPs-on-α-NPD and AuNPs-on-Alq_3 systems. Ultraviolet photoelectron spectroscopy has been employed, in order to investigate the decharging processes of the metal NPs in organic matrixes. The results presented in this chapter are based on the published, peer-reviewed article, Ligorio et. al., App. Phys. Lett. 104, 163302 (2014), and provide experimental evidence for the exciton-mediated decharging of AuNPs upon illumination.

5.2. Results and discussion

Ultraviolet photoemission spectroscopy (UPS) was employed on the same samples described in Chapter 4 (in which the XPS investigation was illustrated). The valence band region has been measured with excitation energy of 35 eV. The UPS measurements were always performed under two different conditions:

- *dark*, i.e. only the excitation light for UPS was irradiating the sample;
- *light*, i.e. the sample was illuminated by an external light source (405 nm laser) during the UPS measurements.

Note that the power of the chosen laser was set to 0.02 mW cm^{-2}, and it was consistently sufficient enough to saturate the shift in energy displayed by the spectra (i.e. additional increase of laser power did not result in a further shift, as will be explained below). Further detail will follow.

The particular wavelength of the laser (405 nm) was chosen, in order to be within the optical absorption range for both organic molecules. Figure 5.1 displays the UV-VIS spectrum of 60 nm thick films of α-NPD (in .a) and Alq_3 (in .b). The spectra show that the molecules' films exhibit optical absorption below 430 nm and 450 nm, respectively; therefore, upon illumination provided by the 405 nm laser, excitons are generated and can diffuse within the films of the organic materials.

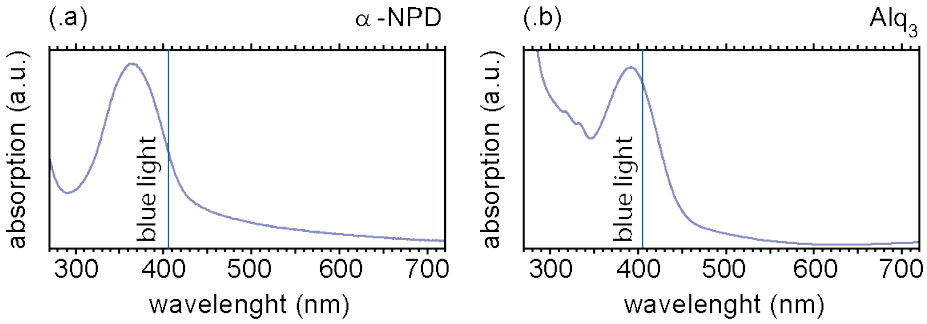

Figure 5.1. UV-VIS absorption spectra of 60 nm thick films of α-NPD (in .a) and Alq_3 (in .b).

Figure 5.2 shows the evolution of the UPS spectra for both systems α-NPD/AuNPs (in .a) and Alq_3/AuNPs (in .b) as a function of the increasing amount of Au (the nominal mass-thickness Θ_{Au} is reported for each experimental deposition step).

It is worth remembering that the deposition of Au is associated with the formation of AuNPs at the very surface of the organic molecular films (see TEM investigations, section 4.2.2) and that nominal mass-thickness Θ_{Au} (reported in the following as "indicator for the sample evolution)" is correlated to AuNPs size and coverage. The graphic in Figure 5.2.c depicts the sample structure for each experimental step.

The bottommost curves in Figure 5.2.a and Figure 5.2.b refer to the pristine molecular films (Θ_{Au} = 0.0 Å). The HOMO onset is found at 1.2 eV and 1.9 eV below E_F for α-NPD and Alq_3, respectively. No energy shift or spectral shape change are detected when the sample is measured in *dark* and in *light*.

Once the AuNPs were deposited on both organic films, two main effects are observed:

- ***i*** **changes in the spectra features**, and
- ***ii*** **rigid shift at higher BE in dark condition** for the steps of intermediate coverage (Θ_{Au} = 0.1 Å, 0.3 Å, 0.4 Å).

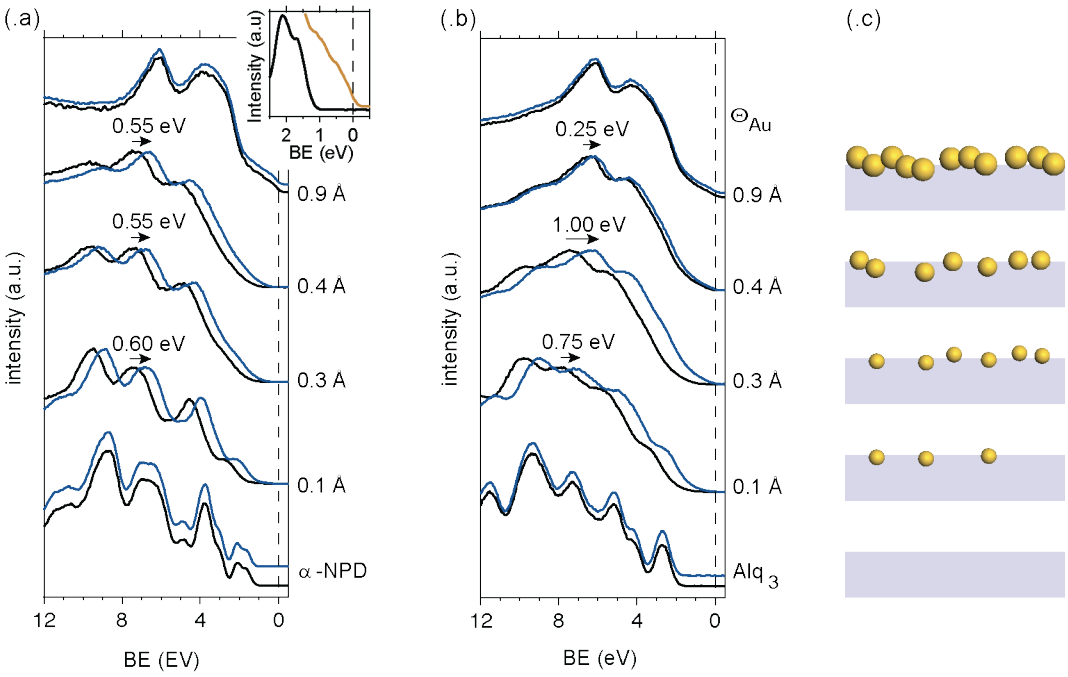

Figure 5.2. UPS spectra evolution as a function of increasing amount of AuNPs, for the α-NPD/AuNPs (in .a) and Alq3/AuNPs (in .b). The measurements were taken both in absence of external light beside the excitation energy (black lines) and with illumination, as provided by an external blue light source (blue lines).

5.2.1. AuNPs deposition effects on molecular valence band

The spectral shape in the valence region significantly changes for the hybrid interfaces with respect to the pristine molecular films, and the formerly sharp peaks, related to the molecular materials, can barely be discerned.

For an increase of Θ_{Au}, the spectra lose typical molecular fingerprints", and even the onset of the HOMO is no longer well-defined. The Au Fermi-edge appears from Θ_{Au} =

0.9 Å onwards (see inserts in Figure 5.2.a), demonstrating that (most of) the NPs are metallic; i.e. since continuous metal film has not been formed at this Θ_{Au}, the number of Au atoms per cluster is high enough to render them metallic. In fact, at this coverage (Θ_{Au} = 0.9 Å), the spectra of both systems are strikingly similar, and they are dominated by emission from Au (essentially two broad features at 4 eV and 6 eV, related to the Au $5d_{3/2}$ and Au $5d_{5/2}$ levels[202]).

In studies of atomically mono-dispersed AuNPs, often 55 atoms[14] are referred to as the amount Z of atoms at which the transition to metallic/non-metallic occurs. More specifically, it has been reported that the switching in Au_{55} can be influenced not only by the size but by the ligation of the outer atoms' shell to specific structure-stabilizing organic chains, as well [203].

In the following section, a simplistic calculation will be presented, in order to estimate the number of atoms as a function of the particle size, based on TEM statistical analysis (section 4.2.2). It is assumed that both density (ρ) and atomic weight (W) value in AuNPs can be approximated with the value of gold in bulk phase:

$$\rho_{\mathrm{AuNP}} \approx \rho_{\mathrm{Au}} = 19.3\ \mathrm{g/cm^3},$$

$$W_{\mathrm{AuNP}} \approx W_{\mathrm{Au}} = 197.$$

Through the mass of a NP with average radius r, given by

$$m_{\mathrm{AuNP}} = \rho_{\mathrm{Au}} \cdot V_{\mathrm{NP}}(r) = \rho_{\mathrm{Au}} \cdot 4/3\,\pi r^3,$$

one can calculate the number of gold moles present in one single AuNP ($N_{\mathrm{Au\ moles}} = m_{\mathrm{AuNP}}/W_{\mathrm{Au}}$). The number of gold atoms in the AuNP of radius r (expressed in cm) is therefore calculated by $Z_{\#/\mathrm{NP}} = N_{\mathrm{Au\ moles}} \cdot \mathcal{N}_{\mathrm{Avocadro}}$

$$Z_{\mathrm{Au/NP}}(r) = \mathcal{N}_{\mathrm{Avocadro}} \cdot \frac{m_{\mathrm{NP}}}{W_{\mathrm{Au}}} = \frac{4}{3}\pi \cdot \frac{19.3}{197} \cdot r^3 \cdot 6.022 \cdot 10^{23}\mathrm{mol}^{-1} \cdot r^3\mathrm{mol}.$$

The values found using this simplistic model are satisfactory in accordance with the literature [203,204]. For instance, an investigation of Au_{102} with atomic resolution has been reported in which NPs were found to be approximately 1 nm [205].

[14] Z = 55 is a "magic number", since the atoms build up a cuboctahedron.

Table 5.1. Estimation of the number of gold atoms in AuNPs, based on the average size as calculated via statistical TEM analysis.

		$\boldsymbol{\rho_{Au}}$ 19.3 [g/cm³]	$\boldsymbol{W_{Au}}$ 197	$\boldsymbol{\mathcal{N}_{Avocadro}}$ 6.022×10²³
$\boldsymbol{d}$ [nm]	V_{NP} [cm³]	m_{NP} [g]	$N_{Au\ moles}$ [mol⁻¹]	$z_{\#/NP}(r)$
0.5	5.24×10⁻²²	1.01×10⁻²⁰	5.13×10⁻²³	31
0.9	3.05×10⁻²¹	5.89×10⁻²⁰	2.99×10⁻²²	180
1.3	9.20×10⁻²¹	1.78×10⁻¹⁹	9.02×10⁻²²	543

In the UPS measurements reported here, the AuNPs exhibit a clear metallic behavior at the Θ_{Au} = 0.9 Å, corresponding to particles with an average diameter size of 0.9 nm (> 180 atoms).

The rapid evolution of UPS – with consequent alteration of the molecular line shape – can be explained, considering the role played by the chemical changes in both molecular films. In fact, for both molecules, XPS analysis (section 4.2.3) displayed new features in the N1s core levels, as soon as AuNPs were deposited (Θ_{Au} = 0.1 Å). Furthermore, in the case of Alq_3, the C1s core level also exhibits changes, i.e. C-O and C-N components shift toward higher BE, reflecting conformational changes in the molecular structure. This explains the sudden change, since density functional theory (DFT) calculations localize the highest occupied molecular orbital levels (HOMO, HOMO-1) on the lone pairs of nitrogen atoms [206].

Figure 5.3 shows the comparison between the zoomed valence band region for

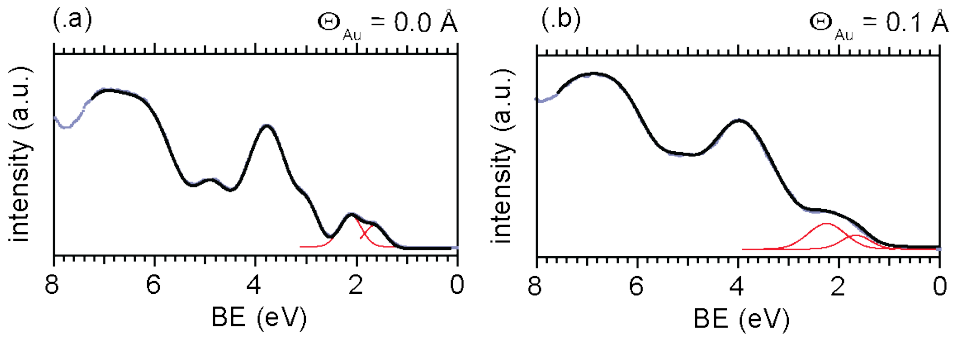

Figure 5.3. Comparison between the valence band regions of the pristine α-NPD molecular film (0.0 Å, in .a) and with 0.1 Å (in .b) of Au mass-thickness deposited. The valence band spectra have been deconvoluted with Gaussian functions (only HOMO, HOMO-1 shown); the spectra fits are shown as black lines on top of the experimental point.

Θ_{Au} = 0.0 Å and Θ_{Au} = 0.1 Å (for the sake of comparison, and to avoid any charging effects, the spectra reported were acquired upon illumination) and relative fit.

For the purpose of clarity, here we consider only α-NPD, where HOMO and HOMO-1 are better energetically resolved with respect to Alq_3 [206]. The zoomed valence band spectra are deconvoluted with Gaussian functions, centered on values based on the DFT calculations of Hill et. al. [206]. The peaks' full-width at half-maximum (FWHM) are adapted to best fit the experimental linewidth. In the case of the pristine molecular film, the FWHM of the first two highest occupied molecular orbitals (~ 300 meV) is consistent with the literature [180,206]. When Au is directly deposited on the surface, the FWHM of the peaks suddenly doubles. Table 5.2 summarizes the values of the peak energy positions (with respect to Fermi energy obtained by measuring the Au foil positioned above the sample) and the respective FWHMs. This broadening in the sample with AuNPs is due to the superposition of signals rising from both unreacted and Au-reacted molecules, which clearly reflects the co-presence of different molecular species at the surface.

Table 5.2. Fitting values for the valence band spectra of the pristine α-NPD molecular film (0.0 Å) and with 0.1 Å of Au mass thickness deposited.

	α-NPD (Θ_{Au} = 0.0 Å)		α-NPD/AuNPs (Θ_{Au} = 0.1 Å)	
	HOMO	HOMO-1	HOMO	HOMO-1
Energy (eV)	1.6	2.1	1.6	2.2
FWHM	0.28	0.30	0.61	0.66

As will be shown in Chapter 6, the inhomogeneity at the organic/inorganic hybrid interface increases the energy disorder of the DOS of the latter, thereby affecting the film mobility.

It is worth noticing that, in regards to the spectral broadening upon deposition of Au on α-NPD and Alq_3,the Au mass-thickness was estimated with a quartz crystal microbalance in our experiments. Therefore, slight differences may exist between the actual Au amounts on both organic surfaces at the same nominal thickness. In addition, the lateral distribution of Au clusters and atoms too small to be individually

resolved by TEM may be inhomogeneous, therefore leading to a more pronounced spectral broadening for Alq_3.

5.2.2. Exciton mediated metal nanoparticles decharging

Besides the change in the spectra shape, due to the different nature of the sample after Au deposition, the systems exhibit an optical induced dynamic. In *dark* conditions – for both systems – the molecular valence structures are shifted towards higher binding energy (by up to 1.0 eV) for Θ_{Au} = 0.1 Å, 0.3 Å and 0.4 Å.

As revealed by TEM analysis, the AuNPs are well separated. Due to the photoemission process itself, the AuNPs become positively charged; furthermore, charge neutralization by electrons from the substrate is not efficient, because the hole state on the AuNPs corresponds to a deep hole trap in the organic matrix. The positive space charge at the surface thus reduces the kinetic energy of the photoelectrons, shifting the UPS spectra toward higher binding energy.

In *light* (i.e. with additional laser illumination), the spectra are shifted towards lower binding energy for Θ_{Au} = 0.1 Å, 0.3 Å and 0.4 Å, compared to those measured in *dark*. This back-shift brings particular molecular emission features, e.g. at 2.5 eV and 5 eV for Alq_3 and at 4 eV and 6 eV for α-NPD, to the same energy position as was observed without AuNPs. Obviously, the illumination with visible light eliminates the space charge on the AuNPs, i.e. the NPs become decharged due to light absorption by the organic matrix.

The proposed mechanism is drafted in Figure 5.4. In the dark condition (Figure 5.4.a), the organic matrix is in a neutral state; the NPs bear positive charges because of the synchrotron radiation (*i*). The space charge at the hybrid surface reduces the photoemitted electron kinetic energy (shifting the UPS spectra toward higher BE, see Figure 5.2).

Upon illumination (Figure 5.4.b), excitons are created after light absorption in the organic matrix (*ii*); electron transfer from the molecular LUMO to the NPs is allowed because of the favorable energy level alignment (*iii*). There is a dynamic equilibrium between the NPs that become charged as a result of photoemission (*i*) and the discharging that results from the excitons' dissociation with those electrons migrating from the organic LUMO in the NPs. The space charge is therefore reduced or made

negligible, and the photoelectrons are not affected at the organic/metal interface (UPS spectra are aligned).

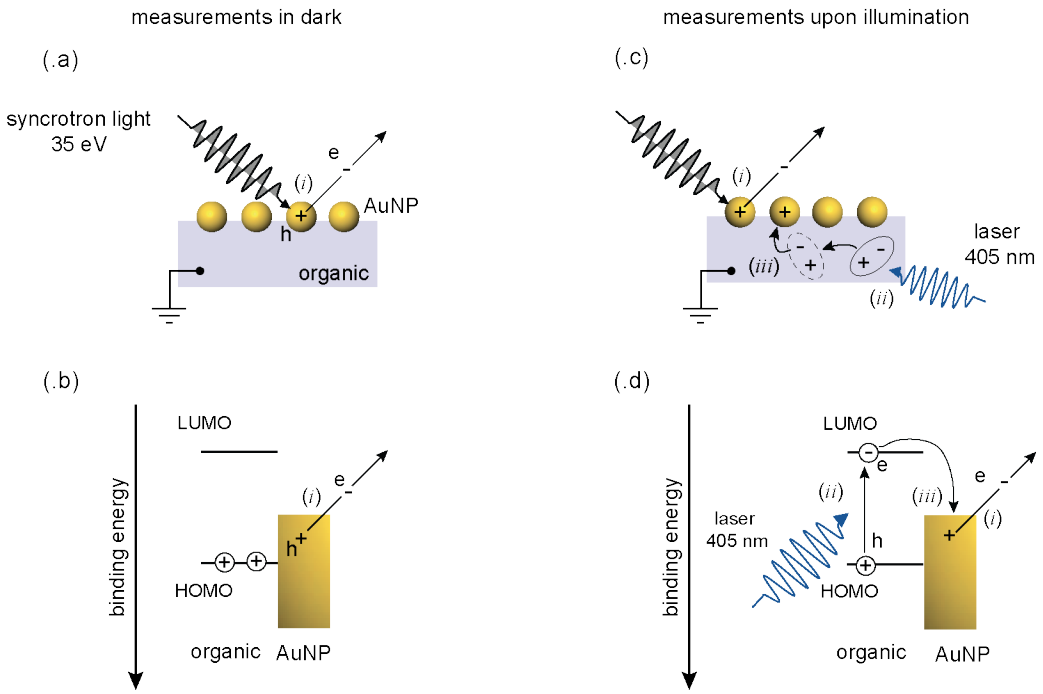

Figure 5.4. The schematics in (.a) and (.c) depict the process of the charging/decharging mechanism, while (.b) and (.d) represent the energy level diagrams: (*i*) electron photoemission with consequent positive charging of AuNP, (*ii*) light absorption and formation of exciton in organic film, and (*iii*) electron transfer from the molecular LUMO levels to the AuNP, with consequent decharging of the latter.

5.3. Summary

In sum, optically induced electron transfer from organic semiconductors to positively charged AuNPs was demonstrated. TEM studies manifested the defined growth of AuNPs on Alq_3 and α-NPD surfaces, which allowed for unambiguous evidence of the decharging mechanism. In our experiments, the photoelectron emission from AuNPs created the surface charge on the AuNPs, and exciton generation in the organic semiconductors was facilitated by laser irradiation. By appropriate selection of the laser intensity, the charge on AuNPs could be completely removed, i.e. dynamic electronic equilibrium was established.

Chapter 6. Optically established neutrality of metal nanoparticles in organic devices

6.1. Overview

As seen in section 1.4, in spite of the decades of research on (two-terminals) resistive non-volatile memory devices (R-NVMs), a consistent explanation about their working mechanism is yet to be found. Among the different proposed models, one that is most frequently invoked speculates that the switching mechanism is related to Coulomb-blockade: the process of charging/decharging of the imbedded metal nanoparticles (MNPs) guides the space-charge field current into the device.

This chapter summarizes the results of electric experiments based on unipolar devices with embedded MNPs. This investigation aimed to determine whether charging of MNPs is present in the resistive switching process of actual devices.

The exciton-mediated de-charging of MNPs, illustrated in Chapter 5, will be employed in the following section in order to control the charging state of MNPs embedded in organic semiconductor by means of optical stimuli. A manuscript with the results presented in this chapter will be soon submitted to the a peer-reviewed journal Applied Physical Letter.

6.2. Results and discussions

6.2.1. Description and structure investigation of the samples

The structures of the two devices discussed in the following section are depicted in Figure 6.1. The leftmost graphic (.a) refers to the reference device (Au-free, referred in the following as *Ref-device*), while the rightmost cartoon (.b) refers to the structure of the device with embedded AuNPs (to be indicated in the following section as *AuNPs-device*). Details about the samples' preparation are reported in section 3.3.2.

The device with embedded AuNPs was fabricated in parallel with the Ref-device, i.e. the Ref-device was kept masked during AuNPs deposition. Thus, the bottom contact (PEDOT:PSS/α-NPD) and top contact (α-NPD/MoO_3) are considered identical in comparing the two devices.

The well-defined AuNPs layer was fabricated by means of direct thermal evaporation (evaporated from a resistance heated Tungsten boat) of low amount of gold on the first 60 nm of α-NPD.

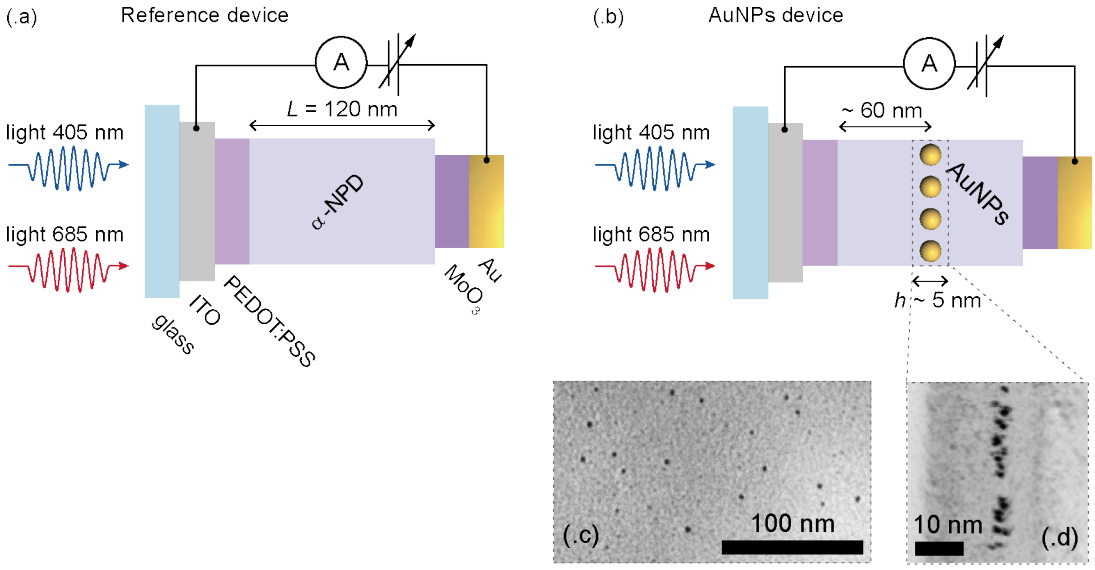

Figure 6.1. The schematic of the experimental setup illustrate the Ref-device (in .a) and the AuNPs-device (in .b). Top-view (in .c) and cross-sectional (.d) TEM images of an equivalent sample provide morphological details about the interlayer with dispersed AuNPs on α-NPD.

The evaporation of such a low amount of Au leads to the formation of dispersed metallic NPs, whose presence is confirmed by transmission electron microscopy (TEM). Figure 6.1.c shows a top-view of a TEM bright field image of an equivalent sample, as prepared on a TEM copper-grid. Consistently with our previous investigations [39] and as reported in previous chapters, it was found that Au does not percolate into the organic film, i.e. AuNPs form a sharp interface on the amorphous material. This is clearly illustrated in Figure 6.1.d, which reports the cross-sectional TEM 3D tomography projection of the sample. Statistical analysis (reported in Figure 6.2) of the equivalent sample, produced on a grid for TEM, indicates an average AuNPs diameter (d_{AuNP}) of 1.4 (± 0.4) nm.

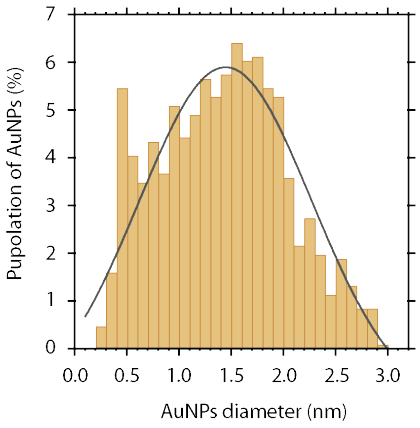

Figure 6.2. AuNPs diameter statistical distribution. The black line is a Gaussian fit of the distribution.

As shown in Figure 6.1.d, the AuNPs are dispersed on the organic surface with high lateral particle-particle distance (with respect to the d_{AuNP}). The device can therefore be understood as the structure represented in Figure 6.1.b: a narrow (h = 5 nm) hybrid interlayer of dispersed AuNPs imbedded in α-NPD, between two (60 nm thick each) films of pristine α-NPD (length $L \sim 120$ nm between the contacts).

After the preparation of the devices, they were introduced, without air exposure, into a nitrogen-filled glove box for the electrical characterization. Current density vs. bias (J-U) curves were measured with a computer-controlled Keithley 2400 source matter at room temperature. All J-U curves are acquired with a continuous bias sweep (0 V → 5 V → -5 V → 0 V). Before recording the J-U curves, the devices were pre-conditioned through of a series of bias sweeps as described in section 3.3.2. The J-U curve measurements were carried out in three different illumination conditions:

- dark;
- illuminated with a red (685 nm) laser; and
- illuminated with a blue (405 nm) laser.

The laser beams were broad enough to illuminate the entire measured device. The power density for both sources was ~ 0.05 mW cm^{-2}. The wavelengths of the lasers were chosen in order to be within (blue) and outside of (red) the optical absorption

peak of the organic molecule. Figure 6.3 shows the ultraviolet-visible (UV-VIS) absorption spectrum of a 60 nm thick film of α-NPD thermally evaporated on ITO/glass. The vertical lines indicate the wavelength's position of the light sources used for the J-U measurements upon illumination. Since the wavelength of the red laser is far away from the absorption peak, it serves as a light reference. No difference in absorption was observed between pristine a-NPD and a-NPD/AuNPs/a-NPD measured via differential UV-VIS.

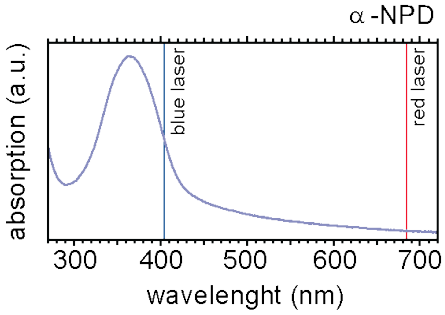

Figure 6.3. UV-VIS absorption spectra of 60 nm thick film of α-NPD. The spectra refers to the wavelength positions of the lasers used as illumination sources.

6.2.2. J-U curve of the reference device (AuNPs-free)

Figure 6.4 refers to the typical J-U curves measured at room temperature for the Ref-device and the AuNPs-device. The forward bias indicates that the top electrode is positively biased; therefore, the positive charge carriers are injected from the MoO_3/Au top electrode. The three J-U curves that overlay on one another refer to the measurement performed in dark condition (dark rhombi), as well as to the measurement performed under illumination with a red laser (685 nm, red triangles) and with a blue laser (405 nm, blue square), respectively. As seen in Figure 6.3, the two lasers have been chosen in accordance with the absorption properties of the organic material.

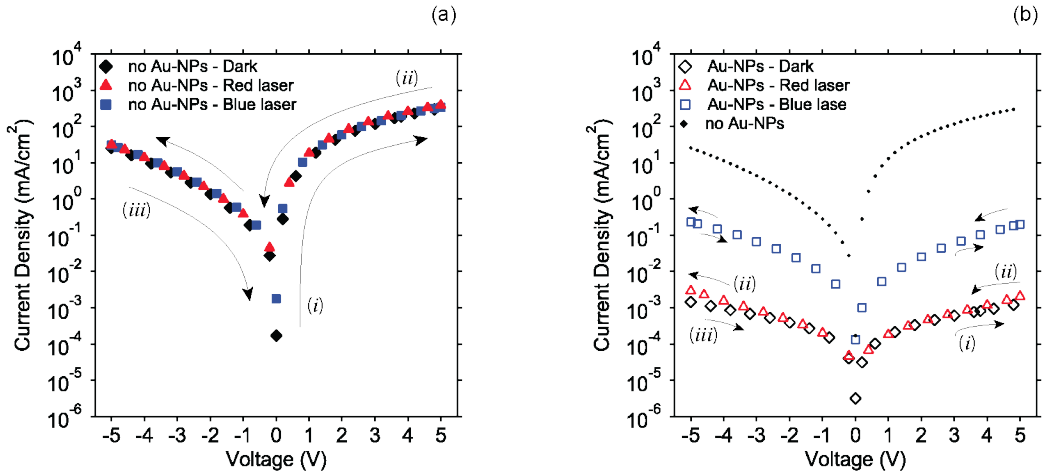

Figure 6.4. J-U curves of the Ref-device and the AuNPs-device are plotted in (.a) and (.b), respectively. The J-U curves are measured with a continuous sweep as indicated by the index arrows. The curves are measured in dark and upon direct illumination of a red and a blue laser. The curves are measured upon the maximum light provided by the laser.

The Ref-device exhibits non-linear behavior and an asymmetric J-U curve. This is a direct consequence of two different top and bottom electrodes. It has been reported that the α-NPD-on-PEDOT:PSS interface has a hole-injection barrier of ~ 0.4 eV [59,60], thus inducing a slight regime of injection limited current at reverse bias.

In contrast, transition metal oxides like MoO_3 (or V_2O_5, CrO_3, WO_3) display a better hole-injection capability and can provide Ohmic contact at the electrode interface [207,208]. In fact, at the MoO_3-on-α-NPD interface, the Fermi level is pinned to the conduction band (CB) of the oxide [173,176]. The majority charges in MoO_3 are electrons qualifying the metal oxide as n-type; the contact with α-NPD can therefore nearly provide nearly Ohmic contact, since electron-transfer occurs from the α-NPD HOMO into MoO_3 CB. This provides *p*-doping at the organic material. Together with the near Ohmic contact, the doped interface increases the conductivity of α-NPD [173,177]. The energy level alignment scheme as well as the carrier injection mechanism is depicted in the image in Figure 6.5. A further factor affecting hole-injection barrier can be the difference in the interfaces' morphology [56], since α-NPD on PEDOT:PSS forms a rather sharp interface, while MoO3 may atomically diffuse in the organic material during thermal evaporation.

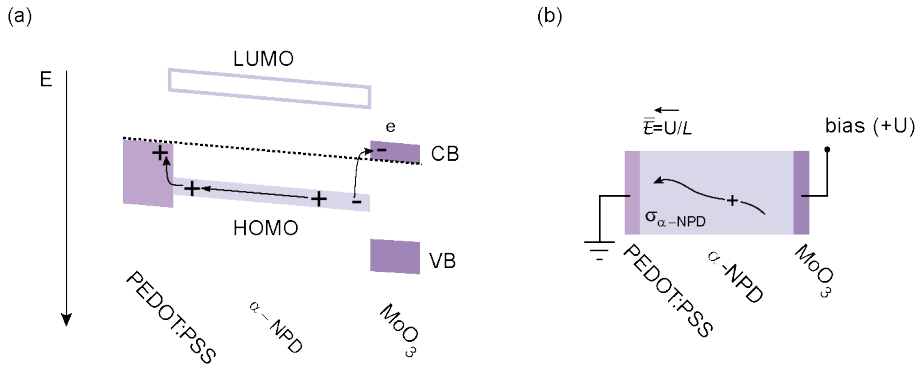

Figure 6.5. The energy level alignment of α-NPD with the top and bottom contacts is depicted in (a). The graphic illustrates the doping of α-NPD induced by the pinning of the MoO_3 CB. The carrier charge transport in the Ref-device upon forward bias is represented in (b).

The J-U curve of the device does not exhibit any difference when measured in dark or upon illumination. This provides evidence that no photocurrent is generated: neither with absorbed (blue) nor not-absorbed (red) light.

6.2.3. J-U curve of AuNPs-device

Figure 6.4.b displays the J-U characteristic curves of the AuNPs-device. For a direct comparison, the J-U curve of the Ref-device is also plotted (small dark rhombi). The J-U curves were acquired by continuous bias sweep, as indicated by the arrows in the figure. In contrast to Ref-device, the Au-NPs-device's J-U curves show symmetry between forward and reverse bias. Most importantly, the device manifests an optical response.

When the device is measured in dark or when the red laser illuminates it, the density current is drastically reduced by 5 orders of magnitude with respect to the Ref-device. Thus, from now on, the red light (not absorbed by the organic material as seen in the UV-VIS Figure 6.3) can be considered as dark.

When the AuNPs-device is measured upon the light radiation provided by the blue laser (absorbed wavelength), the density current is higher by a factor of $\sim 10^2$ with respect to the dark current, but still three order of magnitudes smaller with respect to the reference.

The difference between the J-U curves measured in dark and with the absorbed light cannot be attributed to charge carriers photogeneration at the electrodes' interface, because no such effect has been shown in the reference.

It has been reported that blending metal NPs in organic devices, i.e. hybrid photovoltaic cells (PVCs), can facilitate excitons' dissociation into free carriers (probability increase about 5% for bulk heterojunction PVCs) [165], therefore increasing the current through the device. On the other hand, the amount of AuNPs that we employed is negligible (see Figure 6.1.c) with respect to the hybrid devices usually reported, in which NPs are imbedded in the whole organic volume; therefore, carrier generation, due to excitons dissociation at organic/AuNPs interface, cannot alone explain a change of two order of magnitudes between density current measured in dark and light.

The hybrid organic/AuNPs interface clearly have direct effects on the electrical behavior of the device: first of all, the presence of AuNPs reduces the current through the device; second of all, AuNPs provide opto-switchable properties to the hybrid materials, allowing the device to enhance the current, once the device is illuminated with absorbed light.

In order to better understand the AuNPs effect on the device's electronic behavior, let us consider only the positive bias (i.e. free positive carriers flow from the top to the bottom contact). MoO_3 displays better hole-injection (due to the pinning of the Fermi level to the oxide conduction band) with respect to PEDOT:PSS, allowing for better fitting. Figure 6.6.a reports J-U curve at positive bias for both Ref- and AuNPs-devices, in a semi-log (.a) and log-log representation (.b). In the Ref-device (uppermost curves), the current density J follows with a square law the applied bias U. As seen in section 1.3.2, Mott-Gurney (M-G) law describes this behavior, and the J-U curve can be written as

$$\mathrm{J(U)} = \frac{9}{8}\varepsilon_0\varepsilon_r\mu\frac{\mathrm{U}^2}{L^3}; \qquad \text{(Eq. 6.1)}$$

where ε_0 and ε_r are the dielectric constants of vacuum and the medium, respectively; μ is the free carrier drift mobility; and L is the distance between the electrodes. As reported by Lampert [70], M-G law is typical for a perfect insulator, *free of traps* and with negligible density of free carriers in thermal equilibrium. In such medium, the number of injected carriers is limited, because their electrostatic potential inhibits the injection of additional carriers, and the J-U curve exhibits the SCLC bulk-controlled behavior. This is in perfect agreement with the behavior of the Ref-device, as shown by the perfect match between the experimental data (full marks in Figure 6.6.a) and

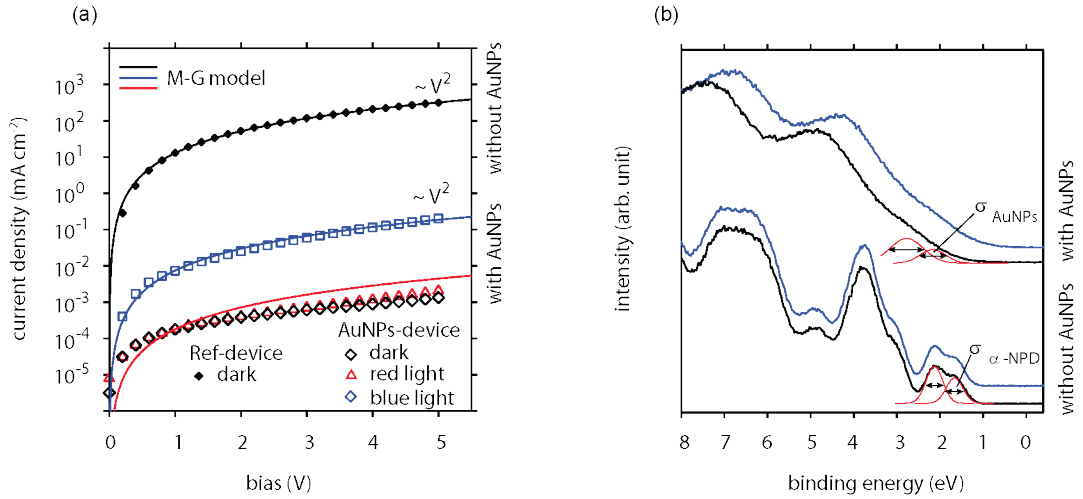

Figure 6.6. The J-U curves, upon forward bias for the Ref-device, and the Au-NPs are plotted in (a). The solid lines form the model based on the M-G equation (Eq. 6.1). The VB spectra of α-NPD and α-NPD/AuNPs measured in dark and light in (b). The red lines are the fit of the HOMO and HOMO-1 assuming a Gaussian DOS.

the M-G model (solid line). The M-G curve has been plotted assuming $\varepsilon_r \approx 3$ [145] and calculating μ from the current density at bias 1 V. For the Ref-device, the calculated mobility for the α-NPD bulk film ($\mu_{\alpha-\mathrm{NPD}}$) is 7.5×10^{-5} cm²/Vs, in good agreement with the literature [51,145,146,209].

The electrical behavior becomes more complex when traps are present in the insulator [70,77]. J-U curve does not follow the M-G law, and the analytical description of the electrical behavior requires the energy distribution of the traps to be known [81].

The difference in the J-U curves between the Ref- and the AuNPs-device is the immediate result of the effects induced by the AuNPs packet inside the α-NPD. AuNPs behave as deep-trap centers for the charge carriers due to the energy alignment between Au and α-NPD [60]. The schematic of the energy alignment is illustrated in Figure 6.7.a The Fermi edge of the isolated AuNPs is between the α-NPD HOMO and LUMO. For the positive carriers transported by the HOMO upon bias, it is energetically favorable to remain on the AuNPs, charging them spontaneously. Due to the formation of a space-charge field, the charged AuNPs inhibit the drift of the positive carriers. The electric potential acts as an injection-limiting barrier for the charge carriers through the hybrid interface, with the consequence of increasing the positive carriers' density p in proximity of the interlayer. The presence of the space-charge field, due to AuNPs

charging effect, was manifested by the shifting toward higher binding energy of VB spectra in the UPS. For the sake of simplicity, Figure 6.6.b only illustrates the previously-discussed VB regions, which are representative for the Ref-device and AuNPs-device discussed here.

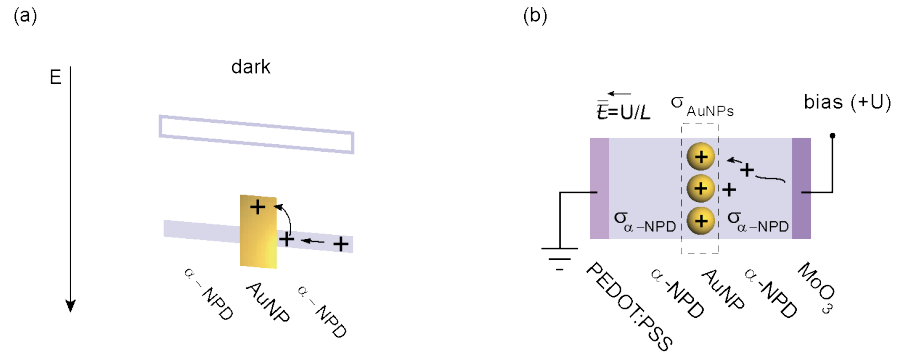

Figure 6.7. The energy level alignment of an isolated AuNP embedded in α-NPD is depicted in (.a). The schematic represents the hole trapping of diffusing charge upon bias. The cartoon in (.b) represents the inhibition of the current due to the build-up of a space-charge field and the local change of the transport constant σ.

A further effect discussed in Chapter 5 concerns the thermal deposition of AuNPs onto the organic film, as well as the consequent changes in the material electronic properties of the organic film. The interaction between AuNPs and the α-NPD results in an increase of the width of the conduction level energy distribution, described by the effective parameter σ [210], reducing the hopping transport, as a result (see previous section 1.3). The change in the VB was shown previously in section 5.2.1 and reported in Figure 6.6.b. The middle interlayer (where the AuNPs are localized) thus has a different σ with respect to the $\sigma_{\alpha\text{-NPD}}$ of the pristine α-NPD. For the sake of convenience, the effective parameter of the hybrid AuNPs/α-NPD interlayer is indicated as σ_{AuNPs} (note that $\sigma_{\text{AuNPs}} > \sigma_{\alpha\text{-NPD}}$).

Pasveer et al. addressed the analytical description of the mobility in organic materials [75], expressing the dependency of the mobility to the temperature T, the carrier density p, and the electric field E; i.e., $\mu = \mu(T, p, E)$. In particular, μ is sensitive to the ratio of σ/k_BT; i.e., $\mu \propto \exp(-\sigma/k_BT)^2$ [4]. In this experiment, T is kept constant throughout, while as seen, σ is modified by the AuNPs thermal deposition. Therefore, mobility can be considered as to be $\mu = \mu(\sigma, p, E)$.

The combined effect of the space-charge field with reduced transport, due to σ, decreases the local mobility at the hybrid interlayer (indicated for convenience as μ_{AuNPs}) with respect to mobility $\mu_{\alpha\text{-NPD}}$ of the pristine molecule bulk.

As previously discussed in the sample description (see section 6.2.1), the AuNPs-device can be modeled as a series of three regions with mobility $\mu_{\alpha\text{-NPD}}$, μ_{AuNPs}, $\mu_{\alpha\text{-NPD}}$, respectively. The effective mobility μ_{eff} for the whole device can be expressed as the harmonic mean of the mobility in each region [211]

$$\frac{1}{\mu_{\text{eff}}} \approx \frac{1}{\mu_{\alpha-\text{NPD}}} + \frac{1}{\mu_{\text{AuNPs}}} + \frac{1}{\mu_{\alpha-\text{NPD}}}.$$

This implies that the mobility is always limited by the lowest conductive region [211]. Thus, the narrow hybrid interlayer is responsible for the drastic drop in the current density displayed by the AuNPs-device. The limited carrier injection is occurring at the interlayer rather than at the electrodes. This explains the symmetry of the AuNPs-device J-U curves. Figure 6.7.b schematically represents the series of the three regions and the inhibition of current due to the AuNPs interlayer.

The presence of AuNPs induces deep and shallow traps in the carrier transport level; therefore, J cannot be analytically described by the MG equation (Eq. 6.1). When the AuNPs-device is measured in blue light (wavelength absorbed by α-NPD), the density current is higher by two orders of magnitudes with respect to one measured in dark. This higher current cannot be attributed to photo-generation at the electrodes interface, because no such effect has been shown in the Ref-device.

The underlying mechanism is the same that is the responsible for the rigid shift in VB (see Figure 6.6.b), once the sample is illuminated by light absorbed by the organic. Excitons are created in the organic materials, populating the lowest unoccupied molecular orbitals (LUMO) [210]. Electron transfer from the LUMO to the positively charged AuNPs is allowed because of the favorable energy configuration, as shown in the schematic Figure 6.8.a, with consequent de-charging of the AuNPs. Because the dynamic optically induced neutralization of the AuNPs (which behave as deep-traps), the J-U curve is well described by the MG model. Figure 6.6.a displays the perfect matching between the experimental data and the curve predicted by the MG model.

The process is considered (as in the UPS experiment) to be a dynamic equilibrium between the AuNPs-charging (due to spontaneous carrier trapping) and the exciton-induced de-charging.

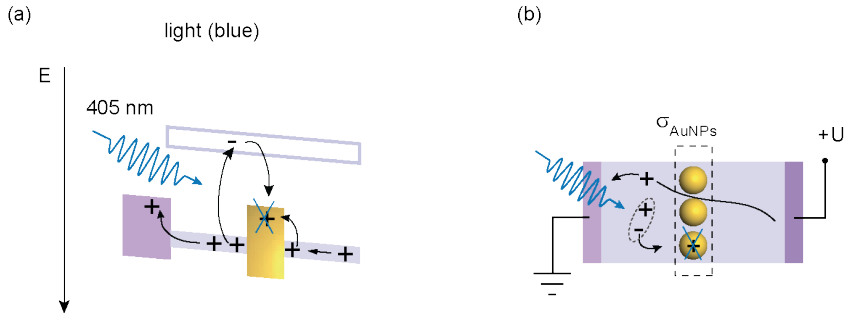

Figure 6.8. The energy level alignment of an isolated AuNP embedded in α-NPD upon illumination is depicted in (.a). The schemata represent exciton-induced decharging of trapped holes. The cartoon in (.b) represents the optical-induced neutralization of the built-up space-charge.

By appropriately selecting the power density of the illumination source, the charge on AuNPs can be almost completely removed. Figure 6.9 shows the current density at bias 5 V vs. the intensity of the light (gradually lowered *via* gray filters) in a semi-log plot. The solid line serves to guide the eyes. The light intensity is enough to reach the saturation regime, i.e. the charge on AuNPs is almost completely neutralized. Illumination contributes to an increase in mobility, since the space-charge field can be optically removed; however, the density current J is still about 3 orders of magnitude less than the ref-device.

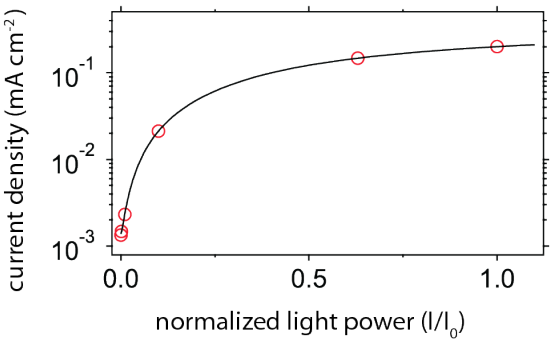

Figure 6.9. Density current of AuNPs-device measure at 5 V bias as a function of the intensity of light power.

The local mobility close to the hybrid interface is nevertheless affected by the increase in the width of the conduction level energy distribution (σ_{AuNPs}).

Despite the above-demonstrated ability to (optically-) control and remove the space-charge field within the organic, the device did not show any bistability or resistivity switching whatsoever. It is worth remembering that, in the devices previously discussed (see Figure 6.1 for the structures), both top and bottom electrodes were metal-free.

6.2.4. Bistability of devices with Al-electrode

A modified α-NPD-based device was fabricated and electrically characterized. The layer of α-NPD had the same nominal thickness (120 nm) as the previous devices. The device was fabricated without inserting any metal NPs interlayer within the α-NPD film (NPs-free). While the bottom contact remained the same as in the devices described above (ITO/PEDOT:PSS), the top contact was substituted with Al (100 nm). The device structure is illustrated in the graphic in Figure 6.10.a.

The I-U curves are measured with continuous sweep. as indicated by the arrows, and plotted in a semi-log scale. Figure 6.10.b displays the current measured from the pristine device. The device was first measured in reversed bias (arrows *i* and *ii*), i.e. the bottom electrode (PEDOT:PSS) was positively charged. The bias was then inverted, and upon forward bias (Al positively charged) the device manifested an abrupt increase of current at ~ 2 V (arrow *iii*). This change in resistivity corresponds to the act of setting the device to the low resistive state (LRS) from high resistive state (HRS). The I-U curve does not display the reestablishment of the HRS, in lowering the bias to the opposite polarity (arrow *iv* and *v*). The device remains (if the bias applied remains within ± 2 V) in the LRS. A higher value of the current level must be reached, in order to switch the device to HRS. Note that all pristine devices to have been measured were initially found in the HRS. Furthermore, the first switch was observed only when Al was positively charged.

Figure 6.10.c displays the typical I-U curve of the ITO/PEDOT:PSS/α-NPD/Al after adequate conditioning. As clearly demonstrated, the device with Al as top-electrode display resistive bistability, in contrast to the device with electrochemically inert electrodes (PEDOT:PSS and MoO_3) discussed above.

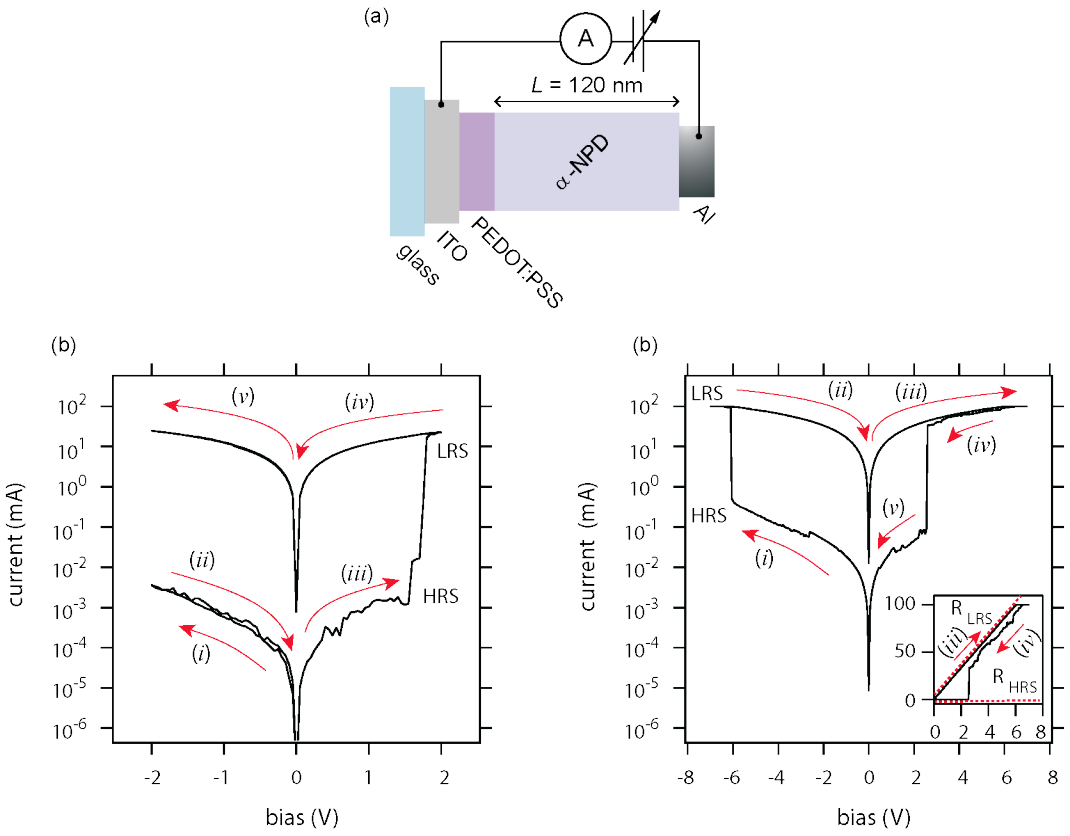

Figure 6.10. The graphic in (a) illustrates the structure of the ITO/PEDOT:PSS/α-NPD/Al device. The measured I-V curves are plotted in semi-log scale. Note that at forward bias, Al is positively charged. The indexed arrows indicate the bias sweep. The very first resistive switch of the device is shown in (b). Switching from HRC to LCS and vice versa is shown in (c) at forward and reverse bias, respectively. The insert in (c) plots I-U curve with linear scales in the forward bias; the dotted lines are linear fit.

Once the device has been conditioned (by means of repeated set/reset cycles), the resistive switching can be achieved both at reverse and forward bias. Figure 6.10.c, in particular, displays the same bias sweep employed in Figure 6.10.b. The device is first polarized in reverse (arrow *i*). The switch from HRS to LRS state occurs at ~ -6 V. To prevent an electrical breakdown of the device, the compliance current was set to 100 mA. After the setting process, the LRS was maintained during the sweep from – 7 V to 7 V (arrows *ii* and *iii*). When positive bias was lowered, the device current rapidly decreased. This is associated with the re-setting process from LRS to the HRS (from arrow *iv* to *v*).

The insert in Figure 6.10.c displays the measured current in linear scale upon forward bias. The resistance values for the HRS and LRS are calculated from J-U curve linear fit (dashed lines); $R_{\mathrm{LRS}} \sim 2.8 \cdot 10^5\ \Omega$ and $R_{\mathrm{HRS}} \sim 4.9 \cdot 10^2\ \Omega$, respectively.

In the literature, it is often reported that active metal (e.g. Cu, Al, Ag) can provide electrochemical mass transfer, and that devices that employ these materials as electrodes display abrupt change in resistivity [108,212–214]. The sudden change in resistivity is attributed to filament formation by the authors. The driving force for electrochemical mass transfer and consequent conductive filament formation is the external electric potential energy. Filaments have been directly observed via imaging investigation techniques [34,215–217]. While the formation of the filament requires the proper bias (in order to migrate the ions to the electric field), the re-formation of the filament is observed in both forward and reverse bias.

Accordingly, the behavior of the device described in the present section is explained by electrochemical diffusion of metallic ions from the Al electrode into the organic. Sebastian et. al. reported on a conceptually identical device (ITO/α-NPD/Al) with impedance spectroscopy [43]. The analysis reveals a transition from capacitive to resistive behavior upon switching voltages. Analogous to what was recently reported by Nau et. al. [42], this strongly suggests that the switching in metal/organic semiconductor/metal structures is caused exclusively by the growth and rupture of resistive filaments in the organic semiconductor.

A final note on the device reported in Figure 6.10: the device has been always measured with current compliance and I-U curve does not display negative differential resistance (NDR), as often reported in the literature [18,34,42,43,197,218]. NDR is attributed to the thinning of the filament due to Joule dissipation (when upon high voltage high current flows into the filament) [26,219–221]. Even if the device does not display NDR, the I-U curve exhibits (arrow *iv*) damaging of the filament, which causes rupture with consequent reset to the HRS.

6.3. Summary

In conclusion, a α-NPD based device without (reference) and with gold nanoparticles (AuNPs) interlayer was fabricated. Metal-free electrodes were employed to guarantee the absence of electrochemical active materials, which could provide metallic ion transport upon bias, i.e. filament formation was suppressed. TEM imaging provided evidence of the presence of isolated AuNPs in the organic matrix.

J-U characterization of the devices was conducted measuring the devices in dark, as well as upon illumination by a laser, with wavelength absorbed by the organic

material. The Ref-device does not display any light dependency in the electric characterization. Measuring in dark, the AuNPs-device displays a mobility $\mu \sim 10^5$ smaller than the Ref-device, and the J-U characteristic manifest an electrical behavior compatible with carrier traps presence. UPS measurement of the hybrid interface (AuNPs on α-NPD) shows an increase of the energetic disorder in the valence levels, as well as a built space charge, due to the charging of AuNPs. The combination of the two explains the strong reduction in mobility and conductivity in the device.

Upon light absorption, the mobility of the AuNPs-device increases by one order of magnitude, with respect to one measured in dark, thus improving the current density in the device. J-U characteristics follow the behavior expected for a trap-free medium. The UPS characterization of the hybrid α-NPD/AuNPs confirms the optically induced de-charging of AuNPs, which produces the suppression of the space-charge field. Despite the proven ability to optically-suppress space-charge field within the organic, the devices did not display bistability.

The electronic behavior of the devices fabricated with inert electrodes has been compared with equivalent devices with an electrochemical active metal as top-electrode (Al). It was found that devices with Al-electrode (even if the device was fabricated without NPs) display resistive switching upon proper polarization.

Chapter 7. Filament formation in nanoscaled resistive non-volatile memory devices

7.1. Overview

In tackling the problem of the miniaturization of memory elements in the nanometric scale, GLAD technique was employed. In GLAD, physical vapor deposition, under conditions of oblique incident-vapor, results in a film with a columnar microstructure. These columns orient themselves toward the vapor source. Substrate rotation can be used to sculpt the columns into various morphologies. Each nanocolumn represents a device in the nanometric scale, capable, in principle, of storing a logic bit.

To electrically characterize the GLAD nanostructured devices, conductive AFM (C-AFM) was used. C-AFM is a modified AFM, which is capable of performing electrical measurements on the nanometric scale. This is achieved by a conductive AFM cantilever that guides a bias voltage to the sample. The nanoscaled resistive-NVMs (R-NVMs) were electrically measured, providing evidence for the working principle based on filament formation/destruction in the lateral nanoscale.

7.2. Results and discussions

7.2.1. Effect of GLAD parameters

Tilt angle

The nano-topographical features of α-NPD thin films deposited with GLAD were investigated with atomic force microscopy (AFM) and scanning electron microscopy (SEM). Figure 7.1 displays the evolution of the film morphology as a function of the tilt angle employed during GLAD.

The topmost section of the figure refers to the film produced at an angle normal to the surface (α = 0); this corresponds to conventional physical vapor deposition. The schematic of the experimental set-up is shown in (.a). The topographical variations, as expected, are very small in comparison to the films produced at glancing angles of incidence (see below). The topography of the film was investigated both with atomic force microscopy (AFM, in .b) in tapping mode and with top-view scanning electron microscopy images (SEM, in .c). Note that the cross-sectional SEM image (.d) shows an uniformly smooth film on top of the ITO/glass substrate.

Typical GLAD nano-columnar structure starts to appear when α is increased above a critical angle (α > 50°, for this combination of substrate/molecular-vapor).

At the very first step of the GLAD process, the nucleation of α-NPD is enhanced at the ITO morphological defects (voids' or hills' surface randomly distributed), which act as nucleation seeds [222–224]. The substrate defects lead to variations in the size and shape of α-NPD nano-pillar. Shadowing effect is the dominant process during the film growth. The images in the central-line in Figure 7.1 refer to a film evaporated at α = 60° (see schematic in .e). As one can see, the topography is characterized by the presence of a structure with higher modulation between valleys and hills, with respect to the α = 0° sample; i.e., note for instance that the height scale in the AFM image (.f) is six times greater. The cross-sectional SEM image (.h) shows a corrugated surface, accordingly.

The increase of α enhances the initial nucleation and therefore the resulting shadowing effect, since even smaller defects of the surface may act as nucleation seeds.

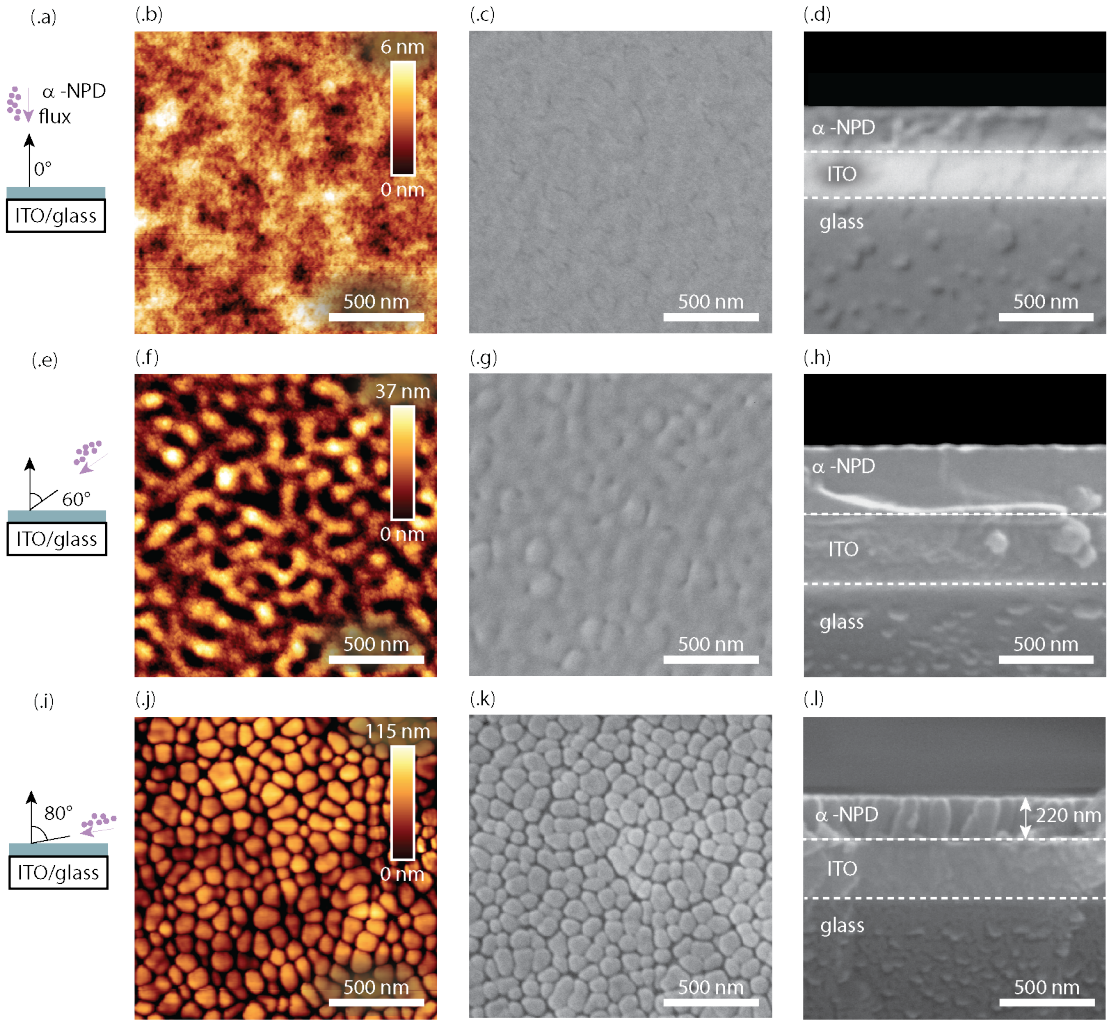

Figure 7.1. Morphological effect of the tilt angle (α) on α-NPD thin films during physical vapor deposition. The topmost pictures refer to the sample evaporated at normal incidence (0°), the central pictures to the sample evaporated at α = 60°, and the bottommost pictures to the sample evaporated at α = 80°. The schematic of the deposition geometry is shown in (.a), (.e), and (.i), respectively. AFM images (acquired in tapping mode) of the three samples are reported in (.b), (.f), and (.j), respectively. Note the different height scales of the AFM images. Top-view SEM images are reported in (.c), (.g), and (.k), respectively. Cross-sectional SEM images in (.d), (.h), and (.l), respectively.

The bottommost images in Figure 7.1 refer to a film evaporated at α = 80°. Isolated α-NPD nanocolumns are distributed on the ITO substrate, as demonstrated clearly by the morphological AFM and SEM images (.j and .k), as well as by the cross-sectional SEM image (.l). By comparing the height scale of the AFM image (.j) with the height calculated by the cross-sectional SEM image (.l), the geometrical constraints of the AFM measurements can be seen as a tip broadening effect, as well as a substantial decrease in the measured height of the film [225].

The comparison between the height measured with AFM (h_{AFM}) and the height measured via SEM image (h_{SEM}) is highlighted in Figure 7.2.a. The absolute height of the α-NPD columnar film AFM image has been corrected with the thickness measured by means of the height displayed in the SEM image, and shown in Figure 7.2.b. The figure provides evidence of the difficulty of probing the height of the nanocolumns, as a smaller fraction of the thickness is accessible with the AFM tip.

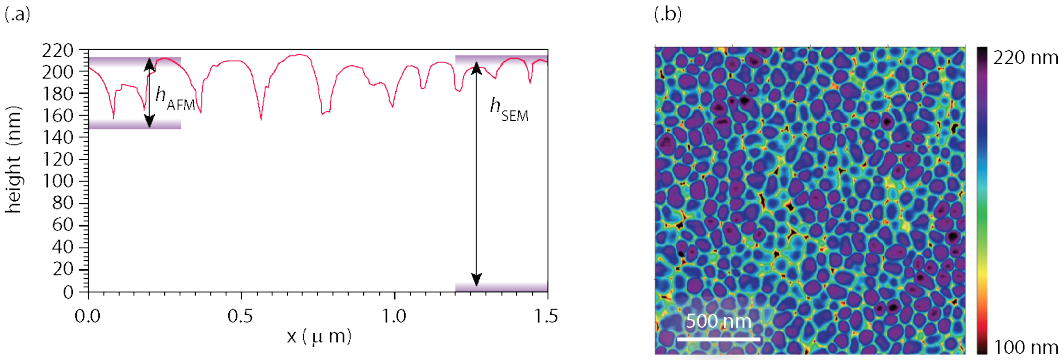

Figure 7.2. AFM line scan of the α-NPD sample α = 80° is shown in (.a). The limitations to properly probing the height of the columns is due to the physical dimensions of the AFM tip. The vertical scale has been corrected with the height measured via SEM (h_{SEM}). Note the difference in height measured via AFM (h_{AFM}). AFM image corrected with the SEM height in (.b).

Rotational speed

To produce the GLAD structures shown in Figure 7.1, it is necessary to continuously rotate the substrate on its normal axis during the evaporation. The effect of different rotation speeds is depicted in Figure 7.3, which reports AFM images of three samples fabricated at different rotational speeds: 0.3 revolutions per minute (rpm) (.a), 3.0 rpm (.b), and 30.0 rpm (.c).

Increasing the rotational speed, the ballistic growth process of nanocolumn formation is affected; i.e., the shadowing effect is reduced by the quicker revolution. In fact, at lower rotational speeds, nanocolumns present an approximate cylindrical shape with a smaller radius and a higher height-to-valley difference, while at the highest speed, nanocolumns collapse together into worm-like structures. Table 7.1 summarizes the analytical properties of the three samples.

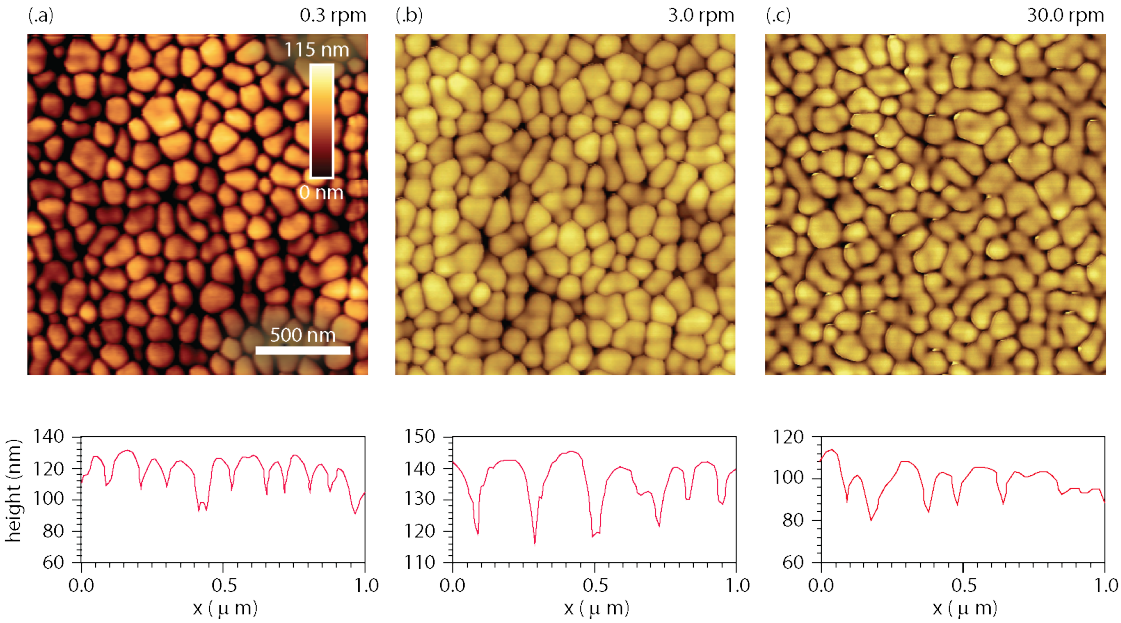

Figure 7.3. AFM images (acquired in tapping mode) and high profiles of three samples of α-NPD growth with GLAD obtained at different rotation speeds. 0.3 rpm in (.a), 3.0 in (.b), and 30.0 rpm in (.c). Note that the height profiles are not corrected by ex-situ investigation. The reported value is the modulation of the AFM cantilever.

Table 7.1. Mean parameters of GLAD samples, fabricated at different rotational speeds, keeping the tilt angle constant (α = 80°).

rotational speed	number of columns μm^2	mean radius	mean coverage
0.3 rpm	95.5	50 nm	48 %
3.0 rpm	81	66 nm	52 %
30.0 rpm	64	79 nm	55 %

7.2.2. Effect of the substrate

Ag coating layer

Columnar growth of α-NPD on silver-coated substrate was investigated for the production of nano-scaled devices, as well. Figure 7.4 displays the comparison between an α-NPD film grown by GLAD technique on pristine ITO/glass and on Ag-coated ITO/glass. The Ag coating film was evaporated in a high-vacuum chamber by means of electron beam evaporatorion (EBE) on ITO. The evaporation rate was about 0.2 Å/s, and the base pressure during metal evaporation was lower than $5 \cdot 10^{-7}$ mbar.

Once ITO was coated with Ag (thickness about 20 nm), without breaking the vacuum, α-NPD was evaporated by means of GLAD on the Ag-coated ITO/glass. The angle between evaporation source and the normal surface was 80°, the evaporation rate was 1 Å/s, and the rotation speed 0.3 rpm.

The presence of Ag underneath the α-NPD nanocolumns is manifested in Figure 7.4.f by the brighter interlayer, due to stronger secondary electrons emission. Topographical statistical analysis did not display a noticeable difference in size and packing for the nanocolumns, with respect to the sample grown on ITO/glass.

Morphologically, the Ag film is also responsible for the presence of irregularity structures; see AFM image in Figure 7.4.e. Investigations with secondary electron microscopy indicate that these structures are the result of the α-NPD growth by means of GLAD. In order to allow for a better contrast in the SEM images (because of the lower atomic number of the organic material), the sample was coated with 10 nm gold. The top-view SEM images in Figure 7.5 report close-ups of the α-NPD structures. The sample was tilted of about 30° during image acquisition.

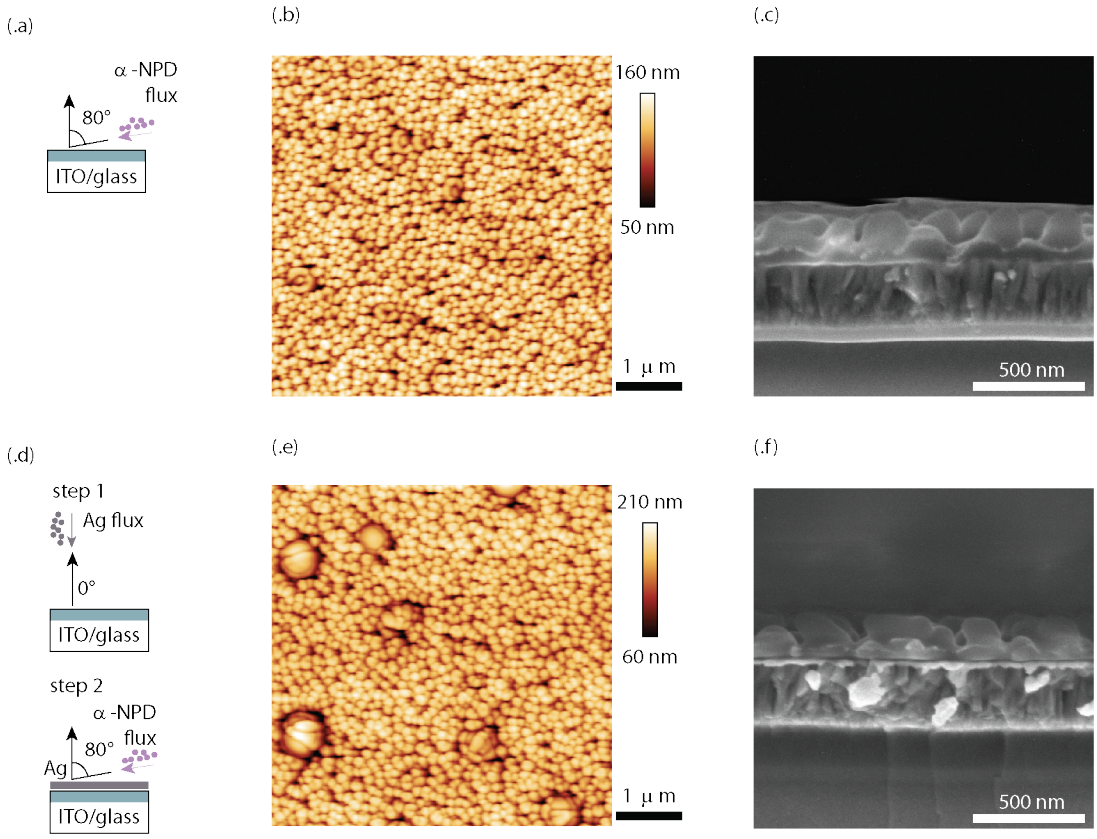

Figure 7.4. AFM (acquired in tapping mode) and SEM images, comparing the nanomorphology of α-NPD nanocolumn grown on pristine ITO/glass (topmost line) and on Ag-coated ITO-glass (bottommost line). The schematic in (.a) and (.d) reports the samples' preparation steps.

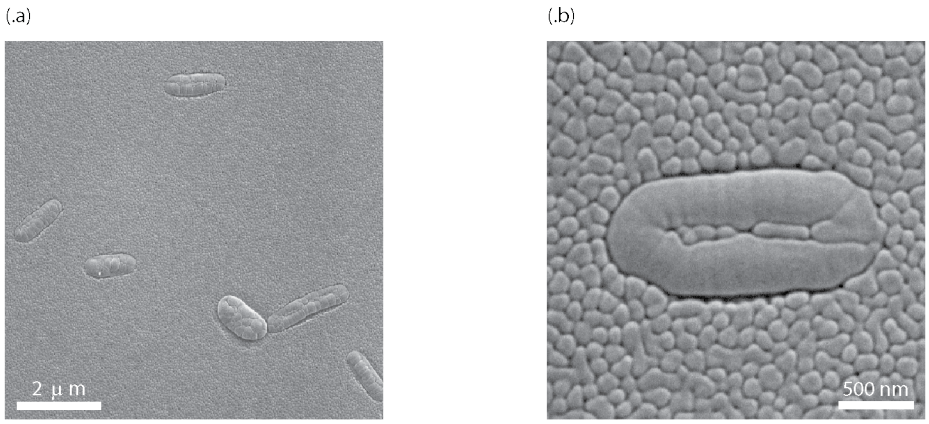

Figure 7.5. SEM images of α-NPD structure's growth by means of GLAD. These structures are induced by morphological defects given by the Ag coating layer.

Ag nanoparticles deposition

Electron beam evaporator was also employed to thermally evaporate silver inside the organic material. Ag was evaporated in a well-defined interlayer (a sharp organic/Ag/organic interface), as well as in co-evaporation; i.e., AgNPs are imbedded in the columns' bulk. AgNPs were thermally deposited, employing a low evaporation rate, as previously reported for AuNPs deposition.

Figure 7.6 shows cross-sectional SEM images (tilted at 30°) of two samples. The left section (.a) of the figure refers to the sample schematically depicted in the cartoon: nanocolumnar film of α-NPD, grown by means of GLAD on Ag coated ITO/glass. The right section (.b) of the figure refers to a sample grown under the same conditions but in which the organic film was not continuously deposited; i.e., A-NPD evaporation was completed in two steps, and Ag was thermally evaporated in between. The graphic on the right depicts the sample structure. The presence of metal is evident when comparing the two images; the upper part of the columns in (.b) is brighter with respect to the columns in (.a), because the secondary electrons originate from the metal. The dashed red line serves to guide the eyes.

A sample with α-NPD/AgNPs in co-evaporation was also prepared. The rates were 1 Å/s for the organic, and about 5 Å/min for the metal. Due to the homogeneity of the organic/AgNPs structure, SEM images show no significant contrast, i.e. AgNPs are not detectable as in the case in Figure 7.6.

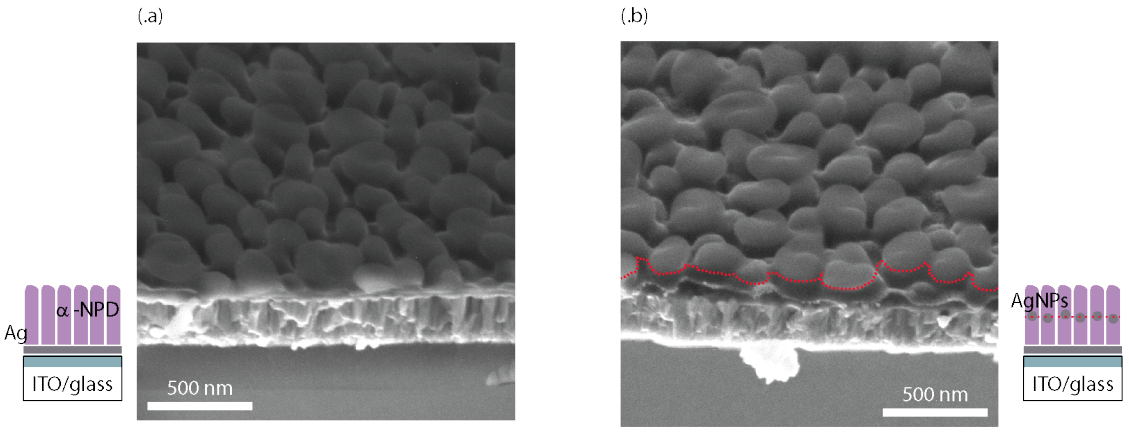

Figure 7.6. Cross-sectional SEM images (tilted of 30°) of nanocolumns α-NPD, grown by means of GLAD on Ag-coated ITO/glass. The comparison is between a sample without (.a) and with AgNPs interlayer (.b). The cartoons on the sides schematically depict the samples structure. The dashed red line guides the eyes, indicating the secondary electrons emitted by the AgNPs interlayer.

7.2.3. Electrical characterization with C-AFM

All electrical measurements presented in this section were performed with conductive AFM (C-AFM). The position of the cantilever during the electrical measurement was maintained via force scan mode. In force scan mode, the AFM cantilever approaches the surface and is kept in contact with the surface by controlling the vertical deflection: i.e. a feedback system controls the force applied on the tip against the sample surface, according to a chosen set point. The position on which the electric measurement was performed had selected after a topography AFM scan in tapping mode. It was therefore possible to perform the electrical characterization of a single chosen nanocolumn. During C-AFM experiments, the current flowing in the sample between the conductive cantilever and the bottom electrode was measured and converted into a voltage by an analog-digital converter. The voltage was amplified and recorded. Therefore, the C-AFM module does not act as a standard voltage supply with a current-meter, but as a differential amplifier in series with a digital-analog converter (DAC) controller that is used to source the bias voltages between the sample and the conductive AFM cantilever. Since the cantilever tip exhibits a very small contact area (tens of nm^2, depending on the penetration of the cantilever in the organic material), compliance current must be set in order to limit the current density, and thus avoid to damage the conductive coating of the cantilever. The maximum current range is ±100 nA (resolution 3 pA). This is an intrinsic limitation of the system with a direct effect on the ability to fully characterize the devices (which will be addressed later).

Figure 7.7.a shows the schematic of the sample structure being referenced. The sample consists of an α-NPD film grown by means of GLAD on ITO/glass. Each nanocolumn represents a single nano-device.

Figure 7.7.b reports the sample 3D reconstruction of the AFM image. The AFM topography image was acquired in tapping mode.

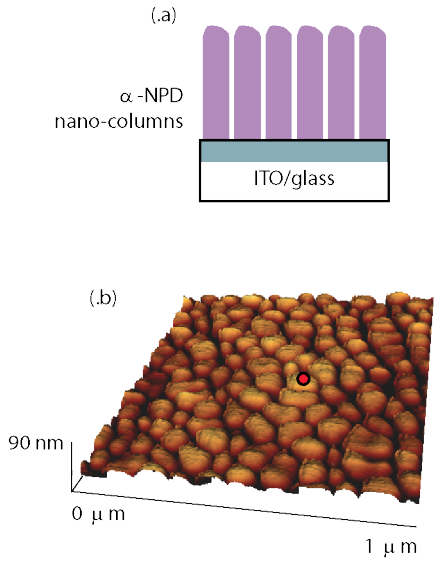

Figure 7.7. The structure of the reference sample is depicted in (.a); i.e., α-NPD grown by GLAD on ITO/glass. The 3D reconstruction of the AFM topography of α-NPD nanocolumns is reported in (.b).

On the chosen position (indicated in Figure 9.7 as a red dot, for the sake of providing an example), the cantilever is brought into contact with the nanocolumn, properly adjusting the setting-point. The Au coated cantilever, in contact with α-NPD, closes the circuit (see Figure 7.8.a). The choice of the electrode materials Au and ITO (with work functions of 5.1 eV and 4.8 eV, respectively) ensures (namely) hole-injection from both electrodes, once the hole-injection barrier has been overcome. The image in Figure 7.8.b depicts the energy alignment between the electrodes and α-NPD.

Figure 7.8.c reports the typical electrical characteristics for the α-NPD/ITO nano-device. The applied bias, the resulting current, and the calculated resistance R are plotted in relation to the measurement time, from bottom to top. For time $t \lesssim 150$ s, the bottom ITO electrode was virtually grounded and the cantilever is positively biased. The bias was increased (with 1 V step), but no current injection was observed. For $t \gtrsim 150$ s, the cantilever was the virtual ground, while ITO remained positively biased.

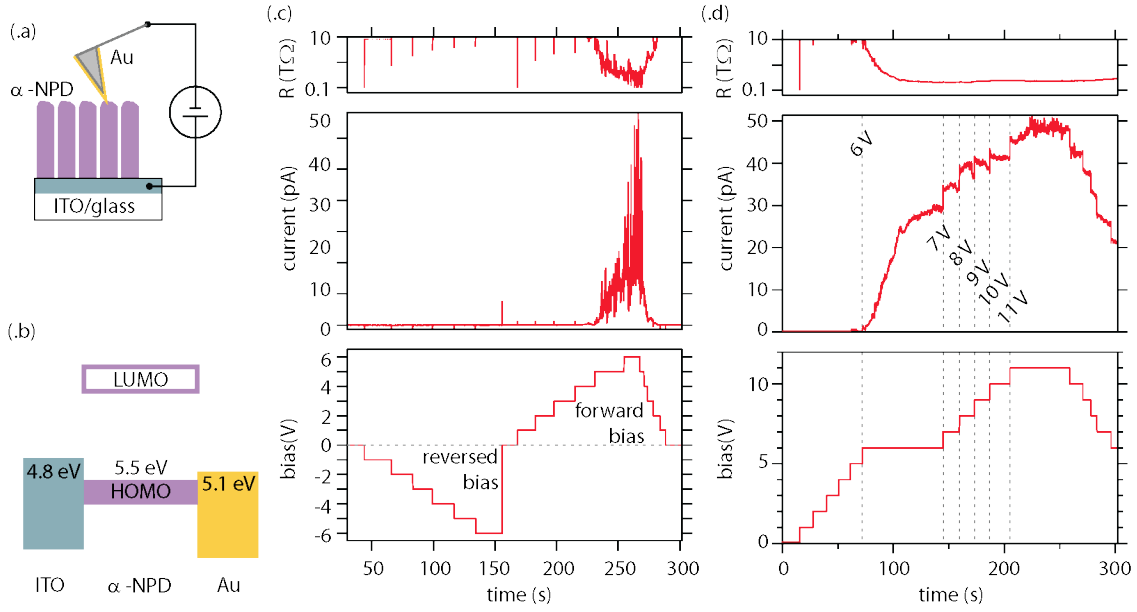

Figure 7.8. The image in (.a) depicts the C-AFM experimental configuration. The schematic in (.b) represents the energy alignment. From the bottom to the top in (.c) and (.d), the electrical curves are plots of the applied bias, current, and resistance (R) as a function of time, respectively. For the sake of simplicity in (.d), the dashed line indicates the time t at which the specific indicated bias is applied.

In this configuration for bias > 5 V, a current (in the order of a few pA) was measured. The figures show that the current is not constant over time; i.e. even if the same bias is applied for tens of seconds, the current value is subject to strong variation. This is even more evident in Figure 7.8.d, where a scan performed entirely in forward bias is shown.

The current fluctuation suggests that the electrical contact with the conductive cantilever is not efficient. The inefficiency of hole-injection from the Au cantilever-electrode can be attributed to the higher injection barrier, which is found at the α-NPD/Au interface due to push-back effect [59]. The measurements were conducted in air, and the interface may have suffered from the presence of humidity, thus resulting in a further reduction of charge injection.

This explains the lack of hole-injection at reverse bias (even if the energy level alignment should allow it), the extremely high resistance R measured (~ TΩ) unexpectedly for α-NPD, and the ohmic behavior. In fact, the device exhibits a constant value of R with respect to the applied bias, (see the logarithmic plot of R in the topmost section of Figure 7.8.d). The device was exposed for extended time (up to 600 s) to the highest bias (+ 11 V) without any noticeable change in resistivity, i.e. the nano-device remains in its high resistance state (HRS).

To observe a change in the conductivity behavior and a switch to a low resistance state (LRS), it is necessary to insert a material in the device that allows filament formation.

Silver has often been reported as an active material, able to form filaments in both organic and inorganic non-volatile memories [96,215,216,219,226]. As illustrated in the previous section 1.5.2, the filament formation arises from ionization of the electrode atoms that leave the electrode and drift upon the applied bias.

The neutralization of the cations occurs either due to electron transfer at the opposite electrode or due to free electrons transported in the organic material. The accumulation of metallic clusters forms a conductive path, effectively bridging the electrodes.

In the α-NPD nano-device, the conductivity change from HRS to LRS is indeed observed, when Ag is inserted between the α-NPD nanocolumns and ITO. Figure 7.9.a displays the structure of the nano-devices based on α-NPD grown on Ag/ITO/glass. The bottommost section and the topmost section of Figure 7.9.b display the applied bias and the current vs. time, respectively.

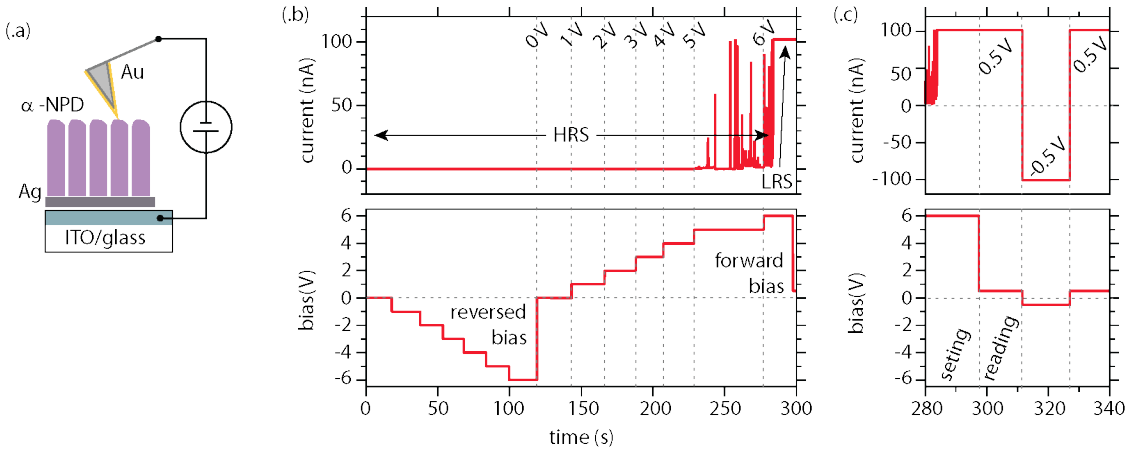

Figure 7.9. Sample structure and experimental setup in (.a). Electrical characterization in (.b), the applied bias-time curve and current-time curve are plotted in the bottommost line and topmost line respectively. The device switches from the HRS to the LRS once 6 V are applied between Ag/ITO electrode and the cantilever (virtually grounded). The current is limited to the internal compliance. If the bias is decreased to smaller value the current is still limited by the compliance; i.e. the nano-device is still in LRS.

Upon positive bias applied to the AFM cantilever electrode (defined as reverse bias), no current is injected. However, the current of the pristine device increases with sharp peaks during sweep (1 V step) of positive bias applied to the ITO electrode. A remarkable change from HRS to LRS is observed at 6 V (occurring at time $t \sim 270$ s in Figure 7.9.b), indicated by the plateau at 100 nA.

The plateau is due to the current compliance. If the bias is lowered to 0.5 V (representing the read-out bias), the device still displays limited current by the compliance, indicating its LRS state (see $t \sim 300$ s in Figure 7.9.c). Coherently, the device once switched into LRS presents at negative bias (- 0.5 V) a negative current (limited by the compliance at -100 nA), see Figure 7.9.c at $t \sim 310$ s.

Nonetheless, the switch from HRS to LRS can only be triggered when Ag is positively biased.

To illustrate the process that leads the formation of a filament bridging the bottom electrode with the cantilever, a constant bias (5 V) was employed to switch a pristine device from HRS to LRS. The current was measured as a function of time, and the curve is plotted in Figure 7.10.

The figure displays the current in different time scales (10 s, 30 s, 60 s, and 180 s). Note that for (.a), (.b), and (.c), the current scale is pA, while for (.d), the scale is in nA.

The conductivity changes over time, as the current varies in orders of magnitude. In particular, a sudden jump of current occurs at t = 172 s. This abrupt change in conductivity indicates that the device has been set from HRS to LRS.

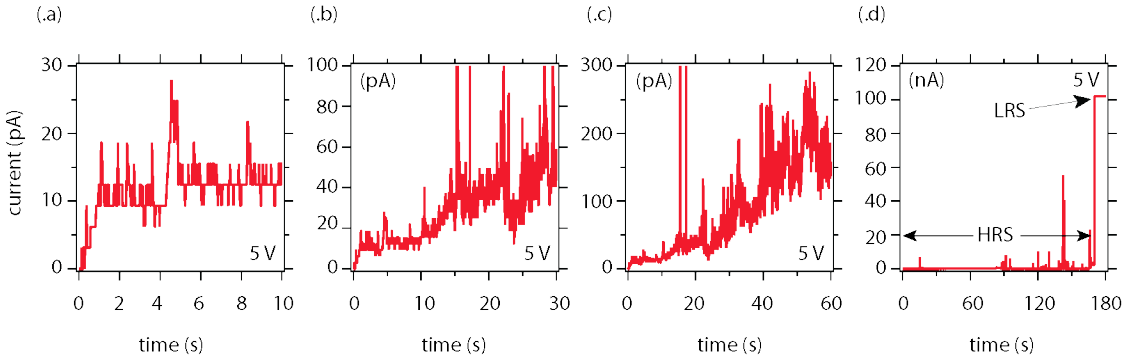

Figure 7.10. Current-time curves of a pristine device upon constant bias of 5 V. All curves refer to the same measurement, i.e. the current is displayed by increasing the time scale. The pristine device lies in HRS; at time 170 s the current increases several orders of magnitude (.d is displayed in nA), and the device is set in LRS.

To study the dynamics of filament formation, current-time curves under different constant bias were carried out. Constant biases (4 V, 5 V, 6 V, 7 V, 8 V and 9 V) were applied, in order to switch pristine nano-devices from HRS to LRS.

The current between the cantilever and the virtual ground was measured and is displayed as a function of time in Figure 7.11.a. The waiting time for the switching event (τ_S) was strongly dependent on the applied bias, since it decreased almost 1 order of magnitude when the bias was increased by 1 V. Figure 7.11.b plots the switching time τ_S vs. the constant applied bias.

The experimental data are in agreement with the fitted line, which assumes an exponential decay [217,227]

$$\tau_S = \tau_0 \exp(-V/V_0); \qquad \text{(Eq. 7.1)}$$

where τ_0 and V_0 are fit parameter. This suggests, therefore, that the transport of the Ag cation is the limiting factor in the dynamics of filament formation [227]. Deviation of some of the data from the exponential decay might be due to the difference in height of the nanocolumns.

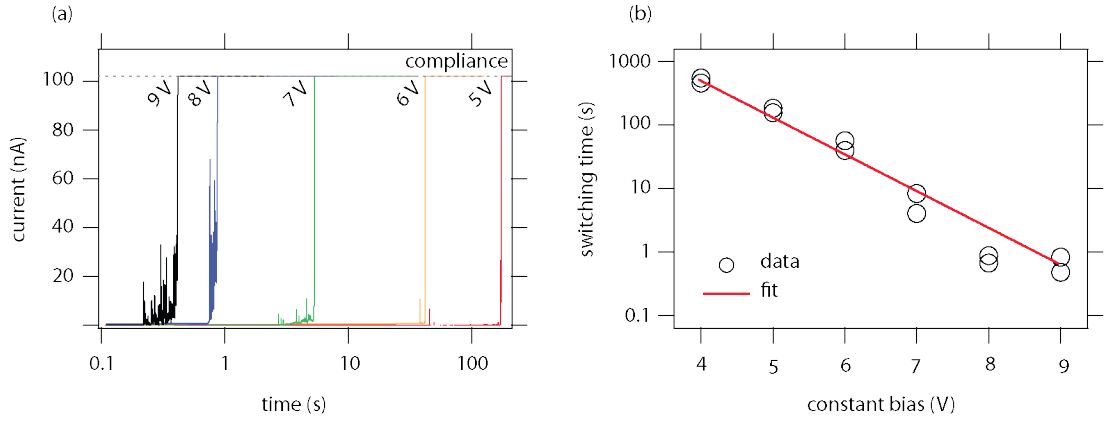

Figure 7.11. Current vs. time curves of pristine devices upon constant bias in (.a). Switching time (τ_S) as a function of the applied constant bias in (.b). The solid line is an exponential fit of the experimental data.

In order to test if the filament formation is indeed limited by the Ag transport mechanism, samples with a well-defined interlayer of Ag within the nano-devices were investigated.

The cross-sectional SEM image reported in the above Figure 7.6.b provides evidence of the presence of an Ag interlayer at half the height of the α-NPD nanocolumns. Similar to the previous experiment, constant voltages (1 V, 2 V, 3 V) were applied to pristine devices with Ag interlayer, and the current-time curve was recorded.

Figure 7.12 displays the current measurements. As expected, the devices display faster dynamics with respect to devices without Ag interlayer (see Figure 7.11); i.e. they display switching from HRS to LRS with lower applied bias and with shorter switching time τ_S.

In R-NVMs, once the filament is formed with consequent bridging of the electrodes, the device is set from the HRS to the LRS. The inverse filament-rupture process is needed, in order to re-set the device in the HRS. Usually, the filament rupture is achieved by applying a voltage greater than the threshold bias needed for the formation of the filament (see section 1.5.2) [41,109]. Joule dissipation, due to the increased current, leads to thinning and degradation of the filaments.

Because of the intrinsic compliance current (100 nA by factory setting), it was not possible to force higher current through the Ag filaments.

Nonetheless, the devices in LRS were kept upon bias for an extended time, manifesting spontaneous switching to HRS [215,216,226].

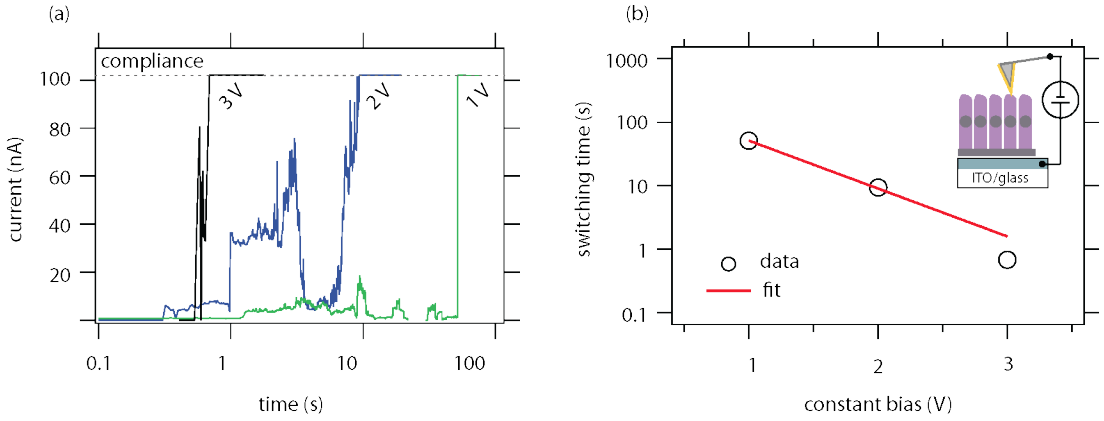

Figure 7.12. Current vs. time curves upon constant bias in (.a). of pristine devices with an Ag interlayer, located at half the height of the α-NPD nanocolumns. Switching time (τ_S) as a function of the applied constant bias in (.b). The inset in (.b) depicts the experimental setup, and illustrates the structure of the nano-columns with embedded AgNPs.

For nano-devices in LRS, the current flows in nano-sized metallic filaments, which implies great current density and still produces remarkable Joule dissipation effects, thereby leading to filament rupture. The Joule-heating provides enough energy to metal atoms to make them diffuse and dissolve the filament [33,41,220].

The spontaneous re-setting from LRS to HRS has been observed for all the devices previously described that contain Ag; i.e. both device types with and without the Ag interlayer. Yet, the effect is particularly clear in devices in which AgNPs are embedded within the nanocolumns; i.e. Ag was co-evaporated at a low rate at normal incidence geometry, while α-NPD columns were grown by means of GLAD. Figure 7.13.a schematically illustrates both the structure of the pristine samples with the experimental setup. The current-time curve upon positive constant bias (1 V) is reported in Figure 7.13.b. The current fluctuations over time indicate the competition between the filament formation dynamic and the filament rupture. When a forward bias is applied to a pristine nano-device, Ag cations drift within the nanocolumn and connect the AgNPs. Once a complete filament is formed, it shorts the electrodes and the current suddenly increases, setting the device in LRS (time $t \approx 20$ s).

The high current density over time induces the thinning of the conductive filament and leads to its eventual failure (e.g. $t \approx 30$ s, $t \approx 120$ s) [220].

In macroscopic R-NVMs during the degradation process which lead to filament-rupture, the devices' I-U curve displays negative differential resistance (NDR); i.e.

current drops through an increase in the applied bias. This is consistent with the current-time curve in Figure 7.13.b, where a decrease of the current occurs over a period of a few seconds (e.g. $t \sim 120$ s). Upon the presence of bias, the filament can be reestablished from the stubs left by the previous degradation.

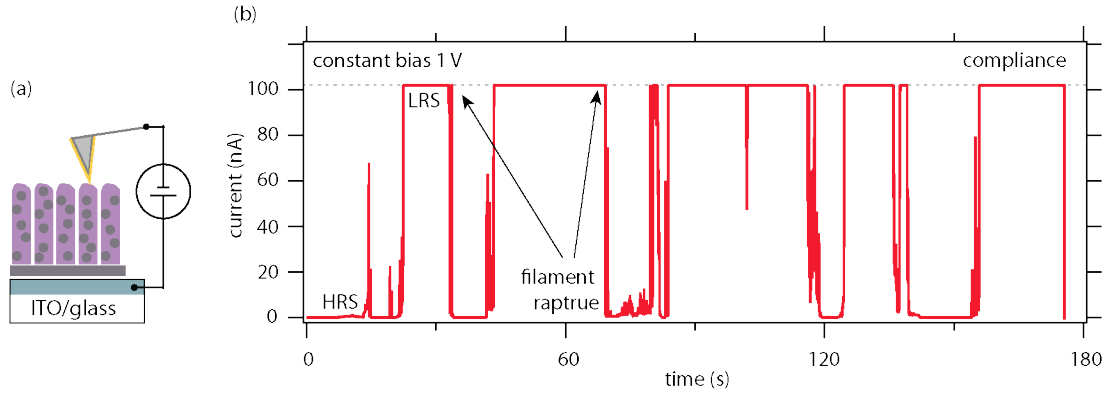

Figure 7.13. The structure of the pristine samples and the experimental apparatus is depicted in (a). The nano-devices were grown via α-NPD evaporation via GLAD while Ag was co-evaporated with EBE in normal incidence geometry with the substrate. The current vs. time curve of a pristine nano-device upon constant bias (1 V) is depicted in (b).

7.3. Summary

In conclusion, nanoscaled devices were fabricated by means of GLAD. The morphological properties of the devices were investigated with AFM and SEM imaging, providing evidence of potential high-density digital data storage. About 100 nano-devices per square micron have been found, which correspond to about six times the storage capacity of a commercial DVD [228].

The switching mechanism was studied by measuring electrical properties by means of a conductive AFM (C-AFM). The results indicate that the switching from HRS to LRS is due to sudden current transport through metallic filament arising from an active electrode. Several published *macroscopic* memory devices (both based on organic and inorganic medium between electrodes) show characteristics comparable to the nano-devices reported above [215–217,219,226].

The time-voltage dynamic occurring in the filament formation process was studied as well, and may have potential applications for future devices.

Chapter 8. Conclusion

The aim of the present work was to develop a coherent understanding of organic non-volatile memory devices (NVMs) based on electrical bistability. In particular, it focused on the mechanisms underlying the resistance switching in two-terminal devices, when metal nanoparticles (MNPs) are embedded in organic semiconductors.
The main goal was to detemine the validity of the model based on the Coulomb-blockade arising from the space-charge field induced by the presence of MNPs [15,29–31,95]. To that end, a variety of experiments was conducted to correlate the electronic and electrical properties of the materials involved in resistive NVMs (R-NVMs).

The materials chosen for this study were prototypical for organic optoelectronics. Due to the need to investigate the optical response of the samples, ITO-coated glass was chosen as substrate. Two small π-conjugated compounds were chosen as a case study (the hole-transport material α-NPD and the electron-transport molecule Alq_3). Their tendency to form amorphous films provides repeatability between experiments. Likewise, gold was chosen as an archetypal metal for NPs, since its work function lies within the frontier orbitals for both molecules (condition claimed to be a requisite by some authors [30,31]). Furthermore, Au allows for direct evaporation of MNPs on the organic molecules without the formation of an oxide layer. It was also chosen since it is generally considered to be an inert metal. For the fabrication of the electrodes' devices, materials that can prevent electrochemical ion mass transport were initially employed, i.e. PEDOT:PSS and MoO_3. This decision was made with the intention of

suppressing the formation of conductive filaments [41,92,108]. In addition, the electrical characteristics were compared with devices employing electrodes that, in contrast, do indeed provide ion mass transport (e.g. Ag and Al).

In Chapter 4 of this work, the electronic structure of the hybrid organic/AuNPs interface was investigated via photoelectron spectroscopy. XPS was employed to explore the effects of Au in terms of metal size on the interaction with α-NPD and Alq_3 molecular films. The molecule–on–Au experiments were compared with the inverted configuration, i.e. AuNPs–on–molecule. TEM studies provided evidence for the defined growth of AuNPs on the organic surfaces. In particular, AuNPs are found to occur confined to the interface, while no percolation is found to occur within the organic films. In the molecule–on–Au cases, no strong interaction was found for both molecular systems, that is, physisorption prevails as a mechanism for molecules on Au. In contrast, for both organic semiconductors α-NPD and Alq_3, chemical reactivity occurs once the size of the deposited Au enters the nanometer scale. As a consequence of the different electronic structure in AuNPs as compared to the Au bulk, the charge redistribution between molecules and the electronic states in the AuNPs leads to the formation of strongly bound organo-metallic complexes. New features (initial-state effects) arising in both molecular and metal spectra indicate charge transfer and thus chemical reactivity. This leads to the formation of an organo-metallic complex. The energy shifts (final-state effects) of the Au peak underline the size-induced nanometric nature of the molecule/Au interaction. These findings point out that size-dependent interactions between metals and organic compounds must be carefully considered.

In Chapter 5, UPS was employed to study how AuNPs induce modifications in the valence electronic structure of pristine organic semiconductors. It was found that the valence spectra shift toward higher binding energy. This provides evidence that AuNPs become positively charged due to the photoemission process. Therefore, a positive space-charge field is present at the organics/AuNPs interface. The charging of the AuNPs occurs, because it is energetically favorable for holes to remain on the AuNPs. Energy-level alignment thus does not allow spontaneous charge neutralization, and AuNPs act as charge-traps for holes. Furthermore, it was found

that the valence electronic structures broaden significantly as a function of the number of AuNPs deposited on top of the organic films.
Upon illumination by visible light (absorbed by the organic molecules), the spectra shift toward lower binding energy. Exciton generation, due to light absorption, allows for electron-transfer from the organic to the AuNPs. The positive charge on the AuNPs is neutralized, hence, removing the space-charge field. Upon illumination, the broadening of the spectra still occurs, indicating that molecular energy levels display a higher degree of DOS energetic disorder with respect to the pristine molecular films.

In Chapter 6, the ability to optically control the presence of space-charge fields in organic films hosting MNPs was employed in electronic devices. Unipolar devices were fabricated with the aim of testing the proposed switching mechanism in R-NVMs, which is based on the Coulomb-blockade. The materials chosen as bottom and top contacts (PEDOT:PSS and MoO_3, respectively) successfully inhibited the formation of metallic filament rising from ion transport upon bias. Therefore, if any resistive bistability were to have been observed, this could have been exclusively addressed to the space-charge field mechanism.
Electrical characterization of the devices was conducted, by measuring J-U curves both in dark and under proper illumination. It was shown that AuNPs act as charge-traps with consequent self-charging effects and with the build-up of a space-charge field bearing effect on conductivity. The MNPs' neutrality can be achieved upon illumination via exciton-mediated electron transfer. The conductivity increases after the optically induced suppression of the space-charge. Despite the ability to optically control the charge state of the embedded MNPs, the devices do not display electrical bistability.
In contrast, the employment of metals able to provide ion mas transport (i.e. formation of conductive filaments) provides resistive bistability upon proper device polarization. The electrochemical metal Al was employed to substitute the inert (MoO_3/Au) top electrode in the fabrication of (NPs-free) devices. Upon positively charging the Al electrode (forward bias), the devices promptly manifested resistive switching between two clear resistive states (HRS and LRS). Once the device was conditioned (filament formed), the switching could be achieved upon both forward and reverse bias, providing bistability to the R-NVM device.

In Chapter 7, the potential miniaturization of R-NVMs was explored. Devices in the nanometric scale were fabricated, employing glancing angle deposition (GLAD). Topographic investigations were provided by means of AFM and SEM. Electrical characterization by conductive AFM (C-AFM) was performed on the samples to verify filament formation in devices with lateral dimensions below 100 nm. Accordingly, for macroscopic devices, it was found that resistance switching is possible only if a material allowing for electrochemical ion mass transport is inserted into the device. Once nanocolumns were fabricated on silver coated ITO/glass, bistability was observed, in contrast to the behavior of nanocolumns fabricated on ITO/glass. Finally, the dynamic of the switching was investigated. In line with the switching mechanism based on conductive filaments, it was found that the filament formation process is dynamically limited by Ag ion transport upon the bias. Employing the GLAD technique, it was possible to achieve a memory density of 0.1 Tbit/cm^2 (about six times the storage capacity of a commercial DVD [228]).

In conclusion, the experimental results provided in this work demonstrate that the mechanism based on charging/de-charging of MNPs (Coulomb-blockade mechanisms) is *not* responsible for resistance switching in organic NVMs. Instead, the electrical bistability can be exclusively attributed to the formation/rupture of conductive filaments. The formation of these filaments was shown to be a consequence of ion mass transport within the organic material, upon proper device polarization. The resistance switching mechanism is accessible in the nanometric scale, and was demonstrated in devices with a lateral scale smaller than 100 nm.

With this thesis, fundamental questions as to the nature of resistance switching in electrode/organic/electrode systems were answered. On this basis, the results reported here raise new questions and encourage/call for future research in the following areas:

- The formation of the conductive filament process should be investigated in greater detail. As suggested by different authors [18,41,220], the working mechanism of a conditioned device is based on the (re-)formation/rupture of the filament, which initially set the device from HRS to LRS. Thus, it remains of paramount importance for technological applications to be able to control the formation of the initial

filament-seed. For this purpose, the parameters affecting the electrochemical dissolution of the electrodes (leading to the ion mass transport) must be fully understood and better controlled, i.e. the natural and chemical properties of the active materials, or the role of the interlayer between the electrodes. The time-bias dependency observed can, furthermore, be promising for technological applications.

- R-NVMs are often categorized with respect to their J-U curve into *unipolar* or *bipolar* [15,27,92,218]. The formation of the conductive filament in devices appears to depend on the polarity of the applied bias only in the very initial formation process. Once the filament has been established, further activations (post rupture) are found to occur for both forward and reverse bias. The ions that re-form the filament (once reduced to metal) stem from the filament itself. Furthermore, as frequently reported in the literature, the rupture is attributed to the thinning of the filament, due to Joule dissipation upon high current flow (independent from polarity) into the filament [26,219–221]. This suggests that the polarity could be a non-determining factor for device behavior in its working state. Therefore, unipolar and bipolar behavior could be unified, a topic worthy of further study.
- The investigation of filament formation for the fabrication of organic R-NVMs could provide useful knowledge to other types of organic electronic devices in which shortening between electrodes is undesirable (e.g. organic LEDs, organic solar cells). A systematic study could investigate the suppression of ion mass transport upon bias (leading to filament formation). The inhibition of ion transport could be achieved by the neutralization of ion species via charge transfer, which could then be reached via *p*- and *n*-doping (or an optically-induced LUMO population).

Acknowledgments

I want to thank Prof. Dr. Norbert Koch for giving me the possibility to work in his group. I am especially thankful for his mentoring and for the numerous opportunities he gave me to perform experiments in many different laboratory facilities. I am much obligated to Dr. Marco Vittorio Nardi, my supervisor. With his great experimental experience and enthusiastic passion for scientific research, he has been an important guide during my thesis.

The work at the synchrotron source (BESSY II) was possible with the assistance of Dr. Antje Vollmer and Dr. Ruslan Ovsyannikov (Helmholtz-Zentrum Berlin). The measurements were also made possible thanks to the support of my colleague Christos Christodoulou.

Prof. Dr. Dieter Neher (University of Potsdam) gave me the opportunity to perform experiments in his laboratory facilities. Thanks to Dr. Robert Steyerleuthner for providing support during the work in the University of Potsdam. Dr. Peter Schäfer (Humboldt University) and Carola Klimm (Helmholtz-Zentrum Berlin) enabled SEM characterizations.

I would like to thank all the members of the HYMEC project, in particular those that directly contributed to this work providing me support in characterization of the devices. From CNRS (Strasbourg), Dr. Martin Brinkman, Dr. Ileana Florea, Dr. Nicolas-Crespo Monteiro, Dr. Ovidiu Ersen performed TEM characterization. I would like to thank Dr. Sebastian Nau, Dr. Stefan Sax (from NTC Weitz), Prof Dr. Alessio Gagliardi

(TU München), Dr. Piero Cosseddu (University of Cagliary) and Francesco Santoni (University of TorVergata) for stimulating discussion.

I would like to thank Prof. Dr. Jürgen P. Rabe (Humboldt University) for giving me access to the experimental equipment in his laboratories. Dr. Philip Lange and Manuel Gensler gave me precious support with the AFM apparatuses. My colleague Junming Li supported me in C-AFM while Dr. Shuwen Yu helped in introducing me to GLAD.

Several people of Prof. Dr. N. Koch's group have to be acknowledged: Dr. Georg Heimel and PD Dr. Andreas Opitz were precious in discussions and in clarifying theoretical concepts useful for the data interpretation. Dr. Johannes Frisch helped with his technical expertise in the lab. Dr. Martin Oehzelt, Dr. Ingo Salzmann, Dr. Jens Niedehausen, Stefanie Winkler, Raphael Schlesinger, Philipp Herann were always available for help and interesting discussion. Last but not least, Henriette Strahl and Timo Florian for the external support to my work.

I would like to express my thanks to Kelly Miller for proofreading this thesis. Dr. Ingo Salzmann, Dr. Melanie Timpel, Dr. Ana-Sofia Anselmo and, in particular, Stefanie Winkler are also thanked for the kind help in proofreading.

This work has been possible also because the surrounding persons that supported me in these years. I thank all my dear friends in Berlin and my beloved family.

List of references

[1] J.C. Scott, Materials science. Is there an immortal memory?, Science. 304 (2004) 62–3.

[2] G.I. Meijer, Materials science. Who wins the nonvolatile memory race?, Science. 319 (2008) 1625–6.

[3] J.C. McCallum, Price and Performance Changes of Computer Technology with Time, (2014) http://www.jcmit.com.

[4] G.E. Moore, Lithography and the future of Moore's law, in: T.A. Brunner (Ed.), SPIE's 1995 Symp. Microlithogr., International Society for Optics and Photonics, 1995: pp. 2–17.

[5] M. Lundstrom, Applied physics. Moore's law forever?, Science. 299 (2003) 210–1.

[6] M. Albota, D. Beljonne, J.L. Brédas, J.E. Ehrlich, J.Y. Fu, A.A. Heikal, et al., Design of organic molecules with large two-photon absorption cross sections., Science. 281 (1998) 1653–1656.

[7] G. Heimel, I. Salzmann, S. Duhm, N. Koch, Design of organic semiconductors from molecular electrostatics, Chem. Mater. 23 (2011) 359–377.

[8] J.H. Burroughes, C.A. Jones, R.H. Friend, New semiconductor device physics in polymer diodes and transistors, Nature. 335 (1988) 137–141.

[9] R. Trattnig, L. Pevzner, M. Jäger, R. Schlesinger, M.V. Nardi, G. Ligorio, et al., Bright Blue Solution Processed Triple-Layer Polymer Light-Emitting Diodes Realized by Thermal Layer Stabilization and Orthogonal Solvents, Adv. Funct. Mater. 23 (2013) 4897–4905.

[10] B. Crone, A. Dodabalapur, Y. Lin, R. Filas, Z. Bao, A. LaDuca, et al., Large-scale complementary integrated circuits based on organic transistors, Nature. 403 (2000) 521–3.

[11] L.-L. Chua, J. Zaumseil, J.-F. Chang, E.C.-W. Ou, P.K.-H. Ho, H. Sirringhaus, et al., General observation of n-type field-effect behaviour in organic semiconductors., Nature. 434 (2005) 194–9.

[12] G. Horowitz, Organic Field-Effect Transistors, Adv. Mater. 10 (1998) 365–377.

[13] G. Yu, J. Gao, J.C. Hummelen, F. Wudl, A.J. Heeger, Polymer Photovoltaic Cells: Enhanced Efficiencies via a Network of Internal Donor-Acceptor Heterojunctions, Science (80-.). 270 (1995) 1789–1791.

[14] F.C. Krebs, N. Espinosa, M. Hösel, R.R. Søndergaard, M. Jørgensen, 25th anniversary article: Rise to power - OPV-based solar parks, Adv. Mater. 26 (2014) 29–39.

[15] Y. Yang, J. Ouyang, L.P. Ma, R.J.-H.J.-H. Tseng, C.-W. Chu, Electrical Switching and Bistability in Organic/Polymeric Thin Films and Memory Devices, Adv. Funct. Mater. 16 (2006) 1001–1014.

[16] B. Cho, S. Song, Y. Ji, T.-W. Kim, T. Lee, Organic Resistive Memory Devices: Performance Enhancement, Integration, and Advanced Architectures, Adv. Funct. Mater. 21 (2011) 2806–2829.

[17] Q.-D. Ling, D.-J. Liaw, E.Y.-H. Teo, C. Zhu, D.S.-H. Chan, E.-T. Kang, et al., Polymer memories: Bistable electrical switching and device performance, Polymer (Guildf). 48 (2007) 5182–5201.

[18] J.C.C. Scott, L.D. Bozano, Nonvolatile Memory Elements Based on Organic Materials, Adv. Mater. 19 (2007) 1452–1463.

[19] J. Ouyang, C.W. Chu, R.J.H. Tseng, A. Prakash, Y. Yang, Organic memory device fabricated through solution processing, in: Proc. IEEE, 2005: pp. 1287–1296.

[20] Y. Ji, S. Lee, B. Cho, S. Song, T. Lee, Flexible organic memory devices with multilayer graphene electrodes, in: ACS Nano, 2011: pp. 5995–6000.

[21] L. Li, Q.-D. Ling, S.-L. Lim, Y.-P. Tan, C. Zhu, D.S.H. Chan, et al., A flexible polymer memory device, Org. Electron. 8 (2007) 401–406.

[22] W.L. Leong, N. Mathews, B. Tan, S. Vaidyanathan, F. Dötz, S. Mhaisalkar, Towards printable organic thin film transistor based flash memory devices, J. Mater. Chem. 21 (2011) 5203.

[23] Y. Ji, D.F. Zeigler, D.S. Lee, H. Choi, A.K.-Y. Jen, H.C. Ko, et al., Flexible and twistable non-volatile memory cell array with all-organic one diode-one resistor architecture., Nat. Commun. 4 (2013) 2707.

[24] Y. Ji, B. Cho, S. Song, T.-W. Kim, M. Choe, Y.H. Kahng, et al., Stable switching characteristics of organic nonvolatile memory on a bent flexible substrate., Adv. Mater. 22 (2010) 3071–5.

[25] D.B. Strukov, G.S. Snider, D.R. Stewart, R.S. Williams, The missing memristor found., Nature. 453 (2008) 80–83.

[26] Q.-D. Ling, D.-J. Liaw, C. Zhu, D.S.-H. Chan, E.-T. Kang, K.-G. Neoh, Polymer electronic memories: Materials, devices and mechanisms, Prog. Polym. Sci. 33 (2008) 917–978.

[27] J.C.C.R.C. Scott, L.D.D. Bozano, Nonvolatile Memory Elements Based on Organic Materials, Adv. Mater. 19 (2007) 1452–1463.

[28] P. Heremans, G.H. Gelinck, R. Müller, K.-J. Baeg, D.-Y. Kim, Y.-Y. Noh, Polymer and Organic Nonvolatile Memory Devices †, Chem. Mater. 23 (2011) 341–358.

[29] L. Ma, S. Pyo, J. Ouyang, Q. Xu, Y. Yang, Nonvolatile electrical bistability of organic/metal-nanocluster/organic system, Appl. Phys. Lett. 82 (2003) 1419–1421.

[30] L.D. Bozano, B.W. Kean, V.R. Deline, J.R. Salem, J.C. Scott, Mechanism for bistability in organic memory elements, Appl. Phys. Lett. 84 (2004) 607–609.

[31] L.D. Bozano, B.W. Kean, M. Beinhoff, K.R. Carter, P.M. Rice, J.C. Scott, Organic materials and thin-film structures for cross-point memory cells based on trapping in metallic nanoparticles, Adv. Funct. Mater. 15 (2005) 1933–1939.

[32] D. Tondelier, K. Lmimouni, D. Vuillaume, C. Fery, G. Haas, Metal/organic/metal bistable memory devices, Appl. Phys. Lett. 85 (2004) 5763.

[33] M. Cölle, M. Büchel, D.M. de Leeuw, Switching and filamentary conduction in non-volatile organic memories, Org. Electron. 7 (2006) 305–312.

[34] B. Cho, J.-M. Yun, S. Song, Y. Ji, D.-Y. Kim, T. Lee, Direct Observation of Ag Filamentary Paths in Organic Resistive Memory Devices, Adv. Funct. Mater. 21 (2011) 3976–3981.

[35] C. Kügeler, R. Rosezin, E. Linn, R. Bruchhaus, R. Waser, Materials, technologies, and circuit concepts for nanocrossbar-based bipolar RRAM, Appl. Phys. A. 102 (2011) 791–809.

[36] J. Ouyang, C.-W. Chu, C.R. Szmanda, L. Ma, Y. Yang, Programmable polymer thin film and non-volatile memory device., Nat. Mater. 3 (2004) 918–922.

[37] B.B. Cho, T. Kim, S. Song, Y. Ji, M. Jo, H. Hwang, et al., Rewritable switching of one diode-one resistor nonvolatile organic memory devices., Adv. Mater. 22 (2010) 1228–32.

[38] G. Ligorio, M.V. Nardi, C. Christodoulou, N. Koch, Organic semiconductor/gold interface interactions: From physisorption on planar surfaces to chemical reactions with metal nanoparticles, ChemPhysChem. DOI: 10.10 (2015).

[39] G. Ligorio, M. Vittorio Nardi, C. Christodoulou, I. Florea, N.C. Monteiro, O. Ersen, et al., Charging and exciton-mediated decharging of metal nanoparticles in organic semiconductor matrices, Appl. Phys. Lett. 104 (2014) 163302.

[40] G. Ligorio, M. Vittorio, C. Christodoulou, R. Steyrleuthner, Optical decharging of metal nanoparticles in hybrid hole-only device, To Be Submitet Appl. Phys. Lett. (2015) 1–10.

[41] R. Waser, R. Dittmann, G. Staikov, K. Szot, Redox-Based Resistive Switching Memories - Nanoionic Mechanisms, Prospects, and Challenges, Adv. Mater. 21 (2009) 2632–2663.

[42] S. Nau, S. Sax, E.J.W. List-Kratochvil, Unravelling the nature of unipolar resistance switching in organic devices by utilizing the photovoltaic effect., Adv. Mater. 26 (2014) 2508–13.

[43] P. Sebastian, F. Lindner, K. Walzer, B. Lüssem, K. Leo, Investigation on the origin of the memory effect in metal/organic semiconductor/metal structures, J. Appl. Phys. 110 (2011) 084508.

[44] P. Atkins, J. de Paula, Atkins' physical chemistry, 10th ed., Oxford University Press, Oxford, 2014.

[45] P.W. Atkins, R. Friedman, Molecular Quantum Mechanics, Oxford University Press, Oxford, 2011.

[46] W. Brütting, ed., Physics of Organic Semiconductors, WILEY-VCH Verlag, 2006.

[47] N. Koch, N. Ueno, A.T.S. Wee, The Molecule-Metal Interface, WILEY-VCH Verlag, Singapore, 2013.

[48] I.G. Hill, A. Kahn, Z.G. Soos, R.A. Pascal, Jr, Charge-separation energy in films of π-conjugated organic molecules, Chem. Phys. Lett. 327 (2000) 181–188.

[49] N. Koch, Electronic structure of interfaces with conjugated organic materials, Phys. Status Solidi - Rapid Res. Lett. 6 (2012) 277–293.

[50] M. Schwoerer, H.C. Wolf, Organic Molecular Solids, WILEY-VCH Verlag, Weinheim, Germany, 2007.

[51] W. Brütting, S. Berleb, A.G. Mückl, Device physics of organic light-emitting diodes based on molecular materials, Org. Electron. 2 (2001) 1–36.

[52] S. Duhm, G. Heimel, I. Salzmann, H. Glowatzki, R.L. Johnson, A. Vollmer, et al., Orientation-dependent ionization energies and interface dipoles in ordered molecular assemblies., Nat. Mater. 7 (2008) 326–32.

[53] G. Heimel, S. Duhm, I. Salzmann, A. Gerlach, A. Strozecka, J. Niederhausen, et al., Charged and metallic molecular monolayers through surface-induced aromatic stabilization., Nat. Chem. 5 (2013) 187–94.

[54] M. Timpel, M. V. Nardi, S. Krause, G. Ligorio, C. Christodoulou, L. Pasquali, et al., Surface Modification of ZnO(0001)–Zn with Phosphonate-Based Self-Assembled Monolayers: Binding Modes, Orientation, and Work Function, Chem. Mater. 26 (2014) 5042–5050.

[55] H. Ishii, K. Sugiyama, E. Ito, K. Seki, Energy Level Alignment and Interfacial Electronic Structures at Organic/Metal and Organic/Organic Interfaces, Adv. Mater. 11 (1999) 605–625.

[56] A. Kahn, N. Koch, W. Gao, Electronic structure and electrical properties of interfaces between metals and p-conjugated molecular films, J. Polym. Sci. Part B Polym. Phys. 41 (2003) 2529–2548.

[57] S. Braun, W.R. Salaneck, M. Fahlman, Energy-Level Alignment at Organic/Metal and Organic/Organic Interfaces, Adv. Mater. 21 (2009) 1450–1472.

[58] A. Wan, J. Hwang, F. Amy, A. Kahn, Impact of electrode contamination on the α-NPD/Au hole injection barrier, Org. Electron. 6 (2005) 47–54.

[59] N. Koch, A. Elschner, J. Schwartz, A. Kahn, Organic molecular films on gold versus conducting polymer: Influence of injection barrier height and morphology on current–voltage characteristics, Appl. Phys. Lett. 82 (2003) 2281.

[60] N. Koch, A. Kahn, J. Ghijsen, J.-J. Pireaux, J. Schwartz, R.L. Johnson, et al., Conjugated organic molecules on metal versus polymer electrodes: Demonstration of a key energy level alignment mechanism, Appl. Phys. Lett. 82 (2003) 70.

[61] R.G. Parr, R.G. Pearson, Absolute hardness: companion parameter to absolute electronegativity, J. Am. Chem. Soc. 105 (1983) 7512–7516.

[62] X. Crispin, V. Geskin, A. Crispin, J. Cornil, R. Lazzaroni, W.R. Salaneck, et al., Characterization of the interface dipole at organic/ metal interfaces., J. Am. Chem. Soc. 124 (2002) 8131–8141.

[63] I.G. Hill, A. Rajagopal, A. Kahn, Y. Hu, Molecular level alignment at organic semiconductor-metal interfaces, Appl. Phys. Lett. 73 (1998) 662.

[64] J.C. Scott, Metal–organic interface and charge injection in organic electronic devices, J. Vac. Sci. Technol. A Vacuum, Surfaces, Film. 21 (2003) 521.

[65] J.C. Scott, G.G. Malliaras, Charge injection and recombination at the metal–organic interface, Chem. Phys. Lett. 299 (1999) 115–119.

[66] S. Nepurek, J. Sworakowski, Use of space-charge-limited current measurements to determine the properties of energetic distributions of bulk traps, J. Appl. Phys. 51 (1980) 2098.

[67] S.M. Sze, K.K. Ng, Physics of Semiconductor Devices, John Wiley & Sons, Inc., Hoboken, NJ, USA, 2006.

[68] V.I. Arkhipov, H. von Seggern, E. V. Emelianova, Charge injection versus space-charge-limited current in organic light-emitting diodes, Appl. Phys. Lett. 83 (2003) 5074.

[69] P. López Varo, J. a. Jiménez Tejada, J. a. López Villanueva, M.J. Deen, Space-charge and injection limited current in organic diodes: A unified model, Org. Electron. 15 (2014) 2526–2535.

[70] M.A. Lampert, Volume-controlled current injection in insulators, Reports Prog. Phys. 27 (1964) 329–367.

[71] E. Conwell, Impurity Band Conduction in Germanium and Silicon, Phys. Rev. 103 (1956) 51–61.

[72] N.F. Mott, ON THE TRANSITION TO METALLIC CONDUCTION IN SEMICONDUCTORS, Can. J. Phys. 34 (1956) 1356–1368.

[73] R.A. Marcus, On the Theory of Oxidation-Reduction Reactions Involving Electron Transfer. I, J. Chem. Phys. 24 (1956) 966.

[74] A. Miller, E. Abrahams, Impurity Conduction at Low Concentrations, Phys. Rev. 120 (1960) 745–755.

[75] H. Bässler, Charge Transport in Disordered Organic Photoconductors a Monte Carlo Simulation Study, Phys. Status Solidi. 175 (1993) 15–56.

[76] H. Bässler, A. Köhler, B. Heinz, K. Anna, Charge transport in organic semiconductors., Top. Curr. Chem. 312 (2012) 1–65.

[77] V. Coropceanu, J. Cornil, D.A. da Silva Filho, Y. Olivier, R. Silbey, J.-L. Brédas, Charge transport in organic semiconductors., Chem. Rev. 107 (2007) 926–52.

[78] W. Pasveer, J. Cottaar, C. Tanase, R. Coehoorn, P. Bobbert, P.W.M. Blom, et al., Unified Description of Charge-Carrier Mobilities in Disordered Semiconducting Polymers, Phys. Rev. Lett. 94 (2005) 206601.

[79] R. Schmechel, H. von Seggern, Electronic traps in organic transport layers, Phys. Status Solidi. 201 (2004) 1215–1235.

[80] S.C. Jain, A.K. Kapoor, W. Geens, J. Poortmans, R. Mertens, M. Willander, Trap filled limit of conducting organic materials, J. Appl. Phys. 92 (2002) 3752.

[81] S.C. Jain, M. Willander, V. Kumar, Conducting Organic Materials and Devices, Semicond. Semimetals. 81 (2007) 1 –188.

[82] A.F. Devonshire, Theory of ferroelectrics, Adv. Phys. 3 (1954) 85–130.

[83] T. Furukawa, Ferroelectric properties of vinylidene fluoride copolymers, Phase Transitions. 18 (1989) 143–211.

[84] Q. Li, G. Mathur, S. Gowda, S. Surthi, Q. Zhao, L. Yu, et al., Multibit Memory Using Self-Assembly of Mixed Ferrocene/Porphyrin Monolayers on Silicon, Adv. Mater. 16 (2004) 133–137.

[85] Z. Liu, A.A. Yasseri, J.S. Lindsey, D.F. Bocian, Molecular memories that survive silicon device processing and real-world operation., Science. 302 (2003) 1543–5.

[86] K.M. Roth, N. Dontha, R.B. Dabke, D.T. Gryko, C. Clausen, J.S. Lindsey, et al., Molecular approach toward information storage based on the redox properties of porphyrins in self-assembled monolayers, J. Vac. Sci. Technol. B Microelectron. Nanom. Struct. 18 (2000) 2359.

[87] K. Tashiro, H. Kaito, M. Kobayashi, Structural changes in ferroelectric phase transitions of vinylidene fluoride-tetrafluoroethylene copolymers: 1. Vinylidene fluoride content dependence of the transition behaviour, Polymer (Guildf). 33 (1992) 2915–2928.

[88] A.J. Lovinger, T. Furukawa, G.T. Davis, M.G. Broadhurst, Crystallographic changes characterizing the Curie transition in three ferroelectric copolymers of vinylidene fluoride and trifluoroethylene: 1. As-crystallized samples, Polymer (Guildf). 24 (1983) 1225–1232.

[89] S.L. Miller, P.J. McWhorter, Physics of the ferroelectric nonvolatile memory field effect transistor, J. Appl. Phys. 72 (1992) 5999.

[90] J.-S. Lee, Review paper: Nano-floating gate memory devices, Electron. Mater. Lett. 7 (2011) 175–183.

[91] D. Prime, S. Paul, P.W. Josephs-Franks, Gold nanoparticle charge trapping and relation to organic polymer memory devices., Philos. Trans. A. Math. Phys. Eng. Sci. 367 (2009) 4215–25.

[92] F. PAN, C. CHEN, Z. WANG, Y. YANG, J. YANG, F. ZENG, Nonvolatile resistive switching memories-characteristics, mechanisms and challenges, Prog. Nat. Sci. Mater. Int. 20 (2010) 1–15.

[93] H.-J. Kim, S.M. Jung, Y.-H. Kim, B.-J. Kim, S. Ha, Y.-S. Kim, et al., Characterization of gold nanoparticle pentacene memory device with polymer dielectric layer, Thin Solid Films. 519 (2011) 6140–6143.

[94] A.K. Mahapatro, R. Agrawal, S. Ghosh, Electric-field-induced conductance transition in 8-hydroxyquinoline aluminum (Alq3), J. Appl. Phys. 96 (2004) 3583.

[95] X. Liu, Z. Ji, L. Shang, H. Wang, Y. Chen, M. Han, et al., Organic programmable resistance memory device based on Au/Alq3/gold-nanoparticle/Alq3/Al structure, IEEE Electron Device Lett. 32 (2011) 1140–1142.

[96] J. Chen, D. Ma, Single-layer organic memory devices based on N,N[sup ']-di(naphthalene-l-yl)-N,N[sup ']-diphenyl-benzidine, Appl. Phys. Lett. 87 (2005) 023505.

[97] J.-G. Park, W.-S. Nam, S.-H. Seo, K.-H. Park, S.-H. Hong, G.-S. Lee, Nonvolatile memory characteristics of small-molecule memory cells with electron-transport and hole-transport bilayers, Curr. Appl. Phys. 10 (2010) e37–e41.

[98] G.Y. Jung, W. Wu, S. Ganapathiappan, D. a. a. Ohlberg, M. Saif Islam, X. Li, et al., Issues on nanoimprint lithography with a single-layer resist structure, Appl. Phys. A. 81 (2005) 1331–1335.

[99] L.P. Ma, J. Liu, Y. Yang, Organic electrical bistable devices and rewritable memory cells, Appl. Phys. Lett. 80 (2002) 2997–2999.

[100] L. Ma, J. Liu, S. Pyo, Y. Yang, Organic bistable light-emitting devices, Appl. Phys. Lett. 80 (2002) 362–364.

[101] W. Tang, H.Z. Shi, G. Xu, B.S. Ong, Z.D. Popovic, J.C. Deng, et al., Memory Effect and Negative Differential Resistance by Electrode- Induced Two-Dimensional Single- Electron Tunneling in Molecular and Organic Electronic Devices, Adv. Mater. 17 (2005) 2307–2311.

[102] J.G. Simmons, R.R. Verderber, New Conduction and Reversible Memory Phenomena in Thin Insulating Films, Proc. R. Soc. A Math. Phys. Eng. Sci. 301 (1967) 77–102.

[103] F. Verbakel, S.C.J. Meskers, R. a. J. Janssen, H.L. Gomes, A.J.M. van den Biggelaar, D.M. de Leeuw, Switching dynamics in non-volatile polymer memories, Org. Electron. 9 (2008) 829–833.

[104] J. Lin, D. Ma, Realization of negative differential resistance and switching devices based on copper phthalocyanine by the control of evaporation rate, Org. Electron. 10 (2009) 275–279.

[105] R.S. Potember, T.O. Poehler, D.O. Cowan, Electrical switching and memory phenomena in Cu-TCNQ thin films, Appl. Phys. Lett. 34 (1979) 405.

[106] Y. Segui, Switching in polystyrene films: Transition from on to off state, J. Appl. Phys. 47 (1976) 140.

[107] L.F. Pender, R.J. Fleming, Memory switching in glow discharge polymerized thin films, J. Appl. Phys. 46 (1975) 3426.

[108] E. Linn, R. Rosezin, C. Kügeler, R. Waser, Complementary resistive switches for passive nanocrossbar memories., Nat. Mater. 9 (2010) 403–6.

[109] Y.-C. Chang, Y.-H. Wang, Resistive switching behavior in gelatin thin films for nonvolatile memory application., ACS Appl. Mater. Interfaces. 6 (2014) 5413–21.

[110] S. Hufner, Photoelectron Spectroscopy, 1976.

[111] S. Hüfner, S. Schmidt, F. Reinert, Photoelectron spectroscopy—An overview, Nucl. Instruments Methods Phys. Res. Sect. A Accel. Spectrometers, Detect. Assoc. Equip. 547 (2005) 8–23.

[112] D. Cahen, A. Kahn, Electron Energetics at Surfaces and Interfaces: Concepts and Experiments, Adv. Mater. 15 (2003) 271–277.

[113] N. Koch, Energy levels at interfaces between metals and conjugated organic molecules, J. Phys. Condens. Matter. 20 (2008) 184008.

[114] H. Ibach, H. Lüth, Solid-state physics: An introduction to principles of materials science, 2010.

[115] G. Binnig, C.F. Quate, C. Gerber, Atomic force microscope, Phys. Rev. Lett. 56 (1986) 930–933.

[116] F. So, Organic Electronics, 2010.

[117] J. Kim, F. Cacialli, a Cola, G. Gigli, R. Cingolani, Increase of charge carriers density and reduction of Hall mobilities in oxygen-plasma treated indium-tin-oxide anodes, 19 (1999) 10–13.

[118] F. Nuesch, L.J. Rothberg, E.W. Forsythe, Q. Toan Le, Y. Gao, A photoelectron spectroscopy study on the indium tin oxide treatment by acids and bases, Appl. Phys. Lett. 74 (1999) 880–882.

[119] K. Sugiyama, H. Ishii, Y. Ouchi, K. Seki, Dependence of indium--tin--oxide work function on surface cleaning method as studied by ultraviolet and x-ray photoemission spectroscopies, J. Appl. Phys. 87 (2000) 295.

[120] C.. J. Brabec, a. Cravino, D. Meissner, N.. S. Sariciftci, M.. T. Rispens, L. Sanchez, et al., The influence of materials work function on the open circuit voltage of plastic solar cells, Thin Solid Films. 403-404 (2002) 368–372.

[121] S.S.K. So, W.W.K. Choi, C.H.C. Cheng, L.M.M. Leung, C.F.F. Kwong, Surface preparation and characterization of indium tin oxide substrates for organic electroluminescent devices, Appl. Phys. A Mater. Sci. Process. 68 (1999) 447–450.

[122] a. R. Schlatmann, D.W. Floet, a. Hilberer, F. Garten, P.J.M. Smulders, T.M. Klapwijk, et al., Indium contamination from the indium–tin–oxide electrode in polymer light-emitting diodes, Appl. Phys. Lett. 69 (1996) 1764.

[123] G. Heywang, F. Jonas, Poly(alkylenedioxythiophene)s—new, very stable conducting polymers, Adv. Mater. 4 (1992) 116–118.

[124] E. Vitoratos, S. Sakkopoulos, E. Dalas, N. Paliatsas, D. Karageorgopoulos, F. Petraki, et al., Thermal degradation mechanisms of PEDOT:PSS, Org. Electron. Physics, Mater. Appl. 10 (2009) 61–66.

[125] M.M. De Kok, M. Buechel, S.I.E. Vulto, P. Van De Weyer, E. a. Meulenkamp, S.H.P.M. De Winter, et al., Modification of PEDOT:PSS as hole injection layer in polymer LEDs, Phys. Status Solidi Appl. Res. 201 (2004) 1342–1359.

[126] N. Koch, A. Vollmer, A. Elschner, Influence of water on the work function of conducting poly(3,4-ethylenedioxythiophene)/poly(styrenesulfonate), Appl. Phys. Lett. 90 (2007) 043512.

[127] M.P. de Jong, L.J. van IJzendoorn, M.J.A. de Voigt, Stability of the interface between indium-tin-oxide and poly(3,4-ethylenedioxythiophene)/poly(styrenesulfonate) in polymer light-emitting diodes, Appl. Phys. Lett. 77 (2000) 2255.

[128] M. Brinkmann, G. Gadret, M. Muccini, C. Taliani, N. Masciocchi, A. Sironi, Correlation between Molecular Packing and Optical Properties in Different Crystalline Polymorphs and Amorphous Thin Films of mer -Tris(8-hydroxyquinoline)aluminum(III), J. Am. Chem. Soc. 122 (2000) 5147–5157.

[129] C.W. Tang, S.A. VanSlyke, Organic electroluminescent diodes, Appl. Phys. Lett. 51 (1987) 913.

[130] M. Cölle, W. Brütting, Thermal, structural and photophysical properties of the organic semiconductor Alq3, Phys. Status Solidi. 201 (2004) 1095–1115.

[131] H.H. Fong, S.K. So, Hole transporting properties of tris(8-hydroxyquinoline) aluminum (Alq 3), J. Appl. Phys. 100 (2006) 1–5.

[132] S. Berleb, W. Brütting, Dispersive electron transport in tris(8-hydroxyquinoline) aluminum (Alq3) probed by impedance spectroscopy., Phys. Rev. Lett. 89 (2002) 286601.

[133] R.G. Kepler, P.M. Beeson, S.J. Jacobs, R.A. Anderson, M.B. Sinclair, V.S. Valencia, et al., Electron and hole mobility in tris(8-hydroxyquinolinolato-N1,O8) aluminum, Appl. Phys. Lett. 66 (1995) 3618.

[134] S.C. Tse, H.H. Fong, S.K. So, Electron transit time and reliable mobility measurements from thick film hydroxyquinoline-based organic light-emitting diode, J. Appl. Phys. 94 (2003) 2033.

[135] H.H. Fong, S.K. So, Effects of nitrogen, oxygen, and moisture on the electron transport in tris(8-hydroxyquinoline) aluminum, J. Appl. Phys. 98 (2005) 023711.

[136] a. Curioni, W. Andreoni, R. Treusch, F.J. Himpsel, E. Haskal, P. Seidler, et al., Atom-resolved electronic spectra for Alq[sub 3] from theory and experiment, Appl. Phys. Lett. 72 (1998) 1575.

[137] A. DeMasi, L.F.J. Piper, Y. Zhang, I. Reid, S. Wang, K.E. Smith, et al., Electronic structure of the organic semiconductor Alq3 (aluminum tris-8-hydroxyquinoline) from soft x-ray spectroscopies and density functional theory calculations., J. Chem. Phys. 129 (2008) 224705.

[138] V.-E. Choong, M.G. Mason, C.W. Tang, Y. Gao, Investigation of the interface formation between calcium and tris-(8-hydroxy quinoline) aluminum, Appl. Phys. Lett. 72 (1998) 2689.

[139] N. Johansson, T. Osada, S. Stafström, W.R. Salaneck, V. Parente, D. a. dos Santos, et al., Electronic structure of tris(8-hydroxyquinoline) aluminum thin films in the pristine and reduced states, J. Chem. Phys. 111 (1999) 2157.

[140] C. Shen, A. Kahn, J. Schwartz, Chemical and electrical properties of interfaces between magnesium and aluminum and tris-(8-hydroxy quinoline) aluminum, J. Appl. Phys. 89 (2001) 449.

[141] C. Shen, A. Kahn, The role of interface states in controlling the electronic structure of Alq3/reactive metal contacts, Org. Electron. 2 (2001) 89–95.

[142] C. Shen, I.G. Hill, A. Kahn, J. Schwartz, Organometallic Chemistry at the Magnesium– Tris(8-hydroxyquinolino)aluminum Interface, J. Am. Chem. Soc. 122 (2000) 5391–5392.

[143] a. Rajagopal, A. Kahn, Photoemission spectroscopy investigation of magnesium–Alq[sub 3] interfaces, J. Appl. Phys. 84 (1998) 355.

[144] S.L.M. Van Mensfoort, V. Shabro, R.J. De Vries, R. a J. Janssen, R. Coehoorn, Hole transport in the organic small molecule material α-NPD: Evidence for the presence of correlated disorder, J. Appl. Phys. 107 (2010) 0–8.

[145] C.H. Cheung, K.K. Tsung, K.C. Kwok, S.K. So, Using thin film transistors to quantify carrier transport properties of amorphous organic semiconductors, Appl. Phys. Lett. 93 (2008) 083307.

[146] T.-Y. Chu, O.-K. Song, Apparent thickness dependence of mobility in organic thin films analyzed by Gaussian disorder model, J. Appl. Phys. 104 (2008) 023711.

[147] G. Schwartz, T.-H. Ke, C.-C. Wu, K. Walzer, K. Leo, Balanced ambipolar charge carrier mobility in mixed layers for application in hybrid white organic light-emitting diodes, Appl. Phys. Lett. 93 (2008) 073304.

[148] S.W. Tsang, S.K. So, J.B. Xu, Application of admittance spectroscopy to evaluate carrier mobility in organic charge transport materials, J. Appl. Phys. 99 (2006) 013706.

[149] W. Gao, A. Kahn, Controlled p doping of the hole-transport molecular material N,N???-diphenyl-N,N???-bis(1-naphthyl)-1,1???-biphenyl-4,4???-di amine with tetrafluorotetracyanoquinodimethane, J. Appl. Phys. 94 (2003) 359–366.

[150] J. Meyer, A. Shu, M. Kröger, A. Kahn, Effect of contamination on the electronic structure and hole-injection properties of MoO[sub 3]/organic semiconductor interfaces, Appl. Phys. Lett. 96 (2010) 133308.

[151] Y. Qi, T. Sajoto, S. Barlow, E.-G. Kim, J.-L. Brédas, S.R. Marder, et al., Use of a high electron-affinity molybdenum dithiolene complex to p-dope hole-transport layers., J. Am. Chem. Soc. 131 (2009) 12530–1.

[152] R.Q. Zhang, C.S. Lee, S.T. Lee, The electronic structures and properties of Alq[sub 3] and NPB molecules in organic light emitting devices: Decompositions of density of states, J. Chem. Phys. 112 (2000) 8614.

[153] F. Viñes, J.R.B. Gomes, F. Illas, Understanding the reactivity of metallic nanoparticles: beyond the extended surface model for catalysis., Chem. Soc. Rev. 43 (2014) 4922–39.

[154] M. Daniel, D. Astruc, Gold nanoparticles: assembly, supramolecular chemistry, quantum-size-related properties, and applications toward biology, catalysis, and nanotechnology., Chem. Rev. 104 (2004) 293–346.

[155] R. Meyer, C. Lemire, S.K. Shaikhutdinov, H.-J. Freund, Surface chemistry of catalysis by gold, Gold Bull. 37 (2004) 72–124.

[156] D.C. Ralph, C.T. Black, M. Tinkham, Spectroscopic Measurements of Discrete Electronic States in Single Metal Particles, Phys. Rev. Lett. 74 (1995) 3241–3244.

[157] J. Petta, D.C. Ralph, Studies of Spin-Orbit Scattering in Noble-Metal Nanoparticles Using Energy-Level Tunneling Spectroscopy, Phys. Rev. Lett. 87 (2001) 266801.

[158] F. Kuemmeth, K.I. Bolotin, S. Shi, D.C. Ralph, Measurement of discrete energy-level spectra in individual chemically synthesized gold nanoparticles., Nano Lett. 8 (2008) 4506–12.

[159] H. Fröhlich, Die spezifische wärme der elektronen kleiner metallteilchen bei tiefen temperaturen, Physica. 4 (1937) 406–412.

[160] R. Kubo, Electronic Properties of Metallic Fine Particles. I., J. Phys. Soc. Japan. 17 (1962) 975–986.

[161] A. Kawabata, R. Kubo, Electronic Properties of Fine Metallic Particles. II. Plasma Resonance Absorption, J. Phys. Soc. Japan. 21 (1966) 1765–1772.

[162] R. Kubo, a Kawabata, S. Kobayashi, Electronic Properties of Small Particles, Annu. Rev. Mater. Sci. 14 (1984) 49–66.

[163] K.L. Kelly, E. Coronado, L.L. Zhao, G.C. Schatz, The Optical Properties of Metal Nanoparticles: The Influence of Size, Shape, and Dielectric Environment, J. Phys. Chem. B. 107 (2003) 668–677.

[164] W.J.E. Beek, M.M. Wienk, R. a. J. Janssen, Efficient Hybrid Solar Cells from Zinc Oxide Nanoparticles and a Conjugated Polymer, Adv. Mater. 16 (2004) 1009–1013.

[165] J.J.-L. Wu, F.-C.F. Chen, Y.Y.-S. Hsiao, F.F.-C. Chien, P. Chen, C.-H. Kuo, et al., Surface plasmonic effects of metallic nanoparticles on the performance of polymer bulk heterojunction solar cells, ACS Nano. 5 (2011) 959–967.

[166] M.-C. Chen, Y. Yang, S. Chen, J. Li, M. Aklilu, Y. Tai, Self-assembled monolayer immobilized gold nanoparticles for plasmonic effects in small molecule organic photovoltaic., ACS Appl. Mater. Interfaces. 5 (2013) 511–7.

[167] M. Sessolo, H.J. Bolink, Hybrid organic-inorganic light-emitting diodes., Adv. Mater. 23 (2011) 1829–45.

[168] J.H. Park, Y.T. Lim, O.O. Park, J.K. Kim, J.-W. Yu, Y.C. Kim, Polymer/Gold Nanoparticle Nanocomposite Light-Emitting Diodes: Enhancement of Electroluminescence Stability and Quantum Efficiency of Blue-Light-Emitting Polymers, Chem. Mater. 16 (2004) 688–692.

[169] M. Kang, K.-J. Baeg, D. Khim, Y.-Y. Noh, D.-Y. Kim, Printed, Flexible, Organic Nano-Floating-Gate Memory: Effects of Metal Nanoparticles and Blocking Dielectrics on Memory Characteristics, Adv. Funct. Mater. 23 (2013) 3503–3512.

[170] C. Raimondo, N. Crivillers, F. Reinders, F. Sander, M. Mayor, P. Samorì, Optically switchable organic field-effect transistors based on photoresponsive gold nanoparticles blended with poly(3-hexylthiophene)., Proc. Natl. Acad. Sci. U. S. A. 109 (2012) 12375–80.

[171] S. Chen, J.R. Manders, S.-W. Tsang, F. So, Metal oxides for interface engineering in polymer solar cells, J. Mater. Chem. 22 (2012) 24202.

[172] S. Tokito, K. Noda, Y. Taga, Metal oxides as a hole-injecting layer for an organic electroluminescent device, J. Phys. D. Appl. Phys. 29 (1996) 2750–2753.

[173] K. Kanai, K. Koizumi, S. Ouchi, Y. Tsukamoto, K. Sakanoue, Y. Ouchi, et al., Electronic structure of anode interface with molybdenum oxide buffer layer, Org. Electron. 11 (2010) 188–194.

[174] J. Meyer, S. Hamwi, M. Kröger, W. Kowalsky, T. Riedl, A. Kahn, Transition metal oxides for organic electronics: energetics, device physics and applications., Adv. Mater. 24 (2012) 5408–27.

[175] J. Meyer, R. Khalandovsky, P. Görrn, A. Kahn, MoO3 films spin-coated from a nanoparticle suspension for efficient hole-injection in organic electronics., Adv. Mater. 23 (2011) 70–3.

[176] M. Kröger, S. Hamwi, J. Meyer, T. Riedl, W. Kowalsky, A. Kahn, Role of the deep-lying electronic states of MoO[sub 3] in the enhancement of hole-injection in organic thin films, Appl. Phys. Lett. 95 (2009) 123301.

[177] M. Kröger, S. Hamwi, J. Meyer, T. Riedl, W. Kowalsky, A. Kahn, P-type doping of organic wide band gap materials by transition metal oxides: A case-study on Molybdenum trioxide, Org. Electron. 10 (2009) 932–938.

[178] R.K. Yonkoski, D.S. Soane, Model for spin coating in microelectronic applications, J. Appl. Phys. 72 (1992) 725.

[179] K. Norrman, a. Ghanbari-Siahkali, N.B. Larsen, 6 Studies of spin-coated polymer films, Annu. Reports Sect. "C" (Physical Chem. 101 (2005) 174.

[180] J. Niederhausen, P. Amsalem, J. Frisch, A. Wilke, A. Vollmer, R. Rieger, et al., Tuning hole-injection barriers at organic/metal interfaces exploiting the orientation of a molecular acceptor interlayer, Phys. Rev. B. 84 (2011) 165302.

[181] M. Haruta, Gold catalysts prepared by coprecipitation for low-temperature oxidation of hydrogen and of carbon monoxide, J. Catal. 115 (1989) 301–309.

[182] H. Sakurai, M. Haruta, Carbon dioxide and carbon monoxide hydrogenation over gold supported on titanium, iron, and zinc oxides, Appl. Catal. A Gen. 127 (1995) 93–105.

[183] A. Ueda, M. Haruta, Nitric Oxide Reduction with Hydrogen, Carbon Monoxide, and Hydrocarbons over Gold Catalysts, Gold Bull. 32 (1999) 3–11.

[184] M. Klasson, J. Hedman, a Berndtsson, R. Nilsson, C. Nordling, P. Melnik, Escape Depths of X-ray Excited Electrons, Phys. Scr. 5 (1972) 93–95.

[185] L.S. Liao, L.F. Chen, X.H. Sun, N.B. Wong, C.S. Lee, S.T. Lee, Substrate dependence of thermal effect on organic light-emitting films, Chem. Phys. Lett. 356 (2002) 194–200.

[186] B. Lu, H. Zhang, H. Li, S. Bao, P. He, T. Hao, Photoemission study of an N,N′-bis-(1-naphthyl)-N,N′-diphenyl-1,1′-biphenyl-4,4′-diamine overlayer on Ag(111), Phys. Rev. B. 68 (2003) 125410.

[187] F. Bisti, A. Stroppa, M. Donarelli, S. Picozzi, L. Ottaviano, Electronic structure of tris(8-hydroxyquinolinato)aluminium(III) revisited using the Heyd-

Scuseria-Ernzerhof hybrid functional: Theory and experiments, Phys. Rev. B. 84 (2011) 195112.

[188] A.C. Dürr, N. Koch, M. Kelsch, A. Rühm, J. Ghijsen, R. Johnson, et al., Interplay between morphology, structure, and electronic properties at diindenoperylene-gold interfaces, Phys. Rev. B. 68 (2003) 115428.

[189] N. Koch, A.C. Dürr, J. Ghijsen, R.L. Johnson, J.-J. Pireaux, J. Schwartz, et al., Optically induced electron transfer from conjugated organic molecules to charged metal clusters, Thin Solid Films. 441 (2003) 145–149.

[190] H. Kröger, P. Reinke, M. Büttner, P. Oelhafen, Gold cluster formation on a fullerene surface, J. Chem. Phys. 123 (2005) 114706.

[191] G. Wertheim, S. DiCenzo, S. Youngquist, Unit Charge on Supported Gold Clusters in Photoemission Final State, Phys. Rev. Lett. 51 (1983) 2310–2313.

[192] P. Citrin, G. Wertheim, Y. Baer, Surface-atom x-ray photoemission from clean metals: Cu, Ag, and Au, Phys. Rev. B. 27 (1983) 3160–3175.

[193] H. Hövel, B. Grimm, M. Pollmann, B. Reihl, Cluster-Substrate Interaction on a Femtosecond Time Scale Revealed by a High-Resolution Photoemission Study of the Fermi-Level Onset, Phys. Rev. Lett. 81 (1998) 4608–4611.

[194] S. DiCenzo, S. Berry, E. Hartford, Photoelectron spectroscopy of single-size Au clusters collected on a substrate, Phys. Rev. B. 38 (1988) 8465–8468.

[195] Y. Kitsudo, A. Iwamoto, H. Matsumoto, K. Mitsuhara, T. Nishimura, M. Takizawa, et al., Final state effect for Au 4f line from gold-nano-particles grown on oxides and HOPG supports, Surf. Sci. 603 (2009) 2108–2114.

[196] L. Calliari, G. Speranza, L. Minati, V. Micheli, A. Baranov, S. Fanchenko, Composition and structure of a-C:Au nanocomposites obtained by physical vapour deposition, Appl. Surf. Sci. 255 (2008) 2214–2218.

[197] J. Lin, D. Ma, Origin of negative differential resistance and memory characteristics in organic devices based on tris(8-hydroxyquinoline) aluminum, J. Appl. Phys. 103 (2008) 124505.

[198] K.K. Yadavalli, A.O. Orlov, G.L. Snider, J. Elam, Aluminum oxide tunnel barriers for single electron memory devices, Microelectronics J. 36 (2005) 272–276.

[199] M. Rozenberg, I. Inoue, M. Sánchez, Nonvolatile Memory with Multilevel Switching: A Basic Model, Phys. Rev. Lett. 92 (2004) 178302.

[200] Q. Chen, B.F. Bory, A. Kiazadeh, P.R.F. Rocha, H.L. Gomes, F. Verbakel, et al., Opto-electronic characterization of electron traps upon forming polymer oxide memory diodes, Appl. Phys. Lett. 99 (2011) 083305.

[201] B.F. Bory, S.C.J. Meskers, R. a. J. Janssen, H.L. Gomes, D.M. de Leeuw, Trapping of electrons in metal oxide-polymer memory diodes in the initial stage of electroforming, Appl. Phys. Lett. 97 (2010) 222106.

[202] C.F. Roulet, H ; Mariot, J-M ; Dufour, G ; Hague, Size dependence of the valence bands in gold clusters, J. Phys. F Met. Phys. 10 (1980) 1025–1030.

[203] H.-G. Boyen, G. Kästle, F. Weigl, P. Ziemann, G. Schmid, M. Garnier, et al., Chemically Induced Metal-to-Insulator Transition in Au55 Clusters: Effect of Stabilizing Ligands on the Electronic Properties of Nanoparticles, Phys. Rev. Lett. 87 (2001) 276401.

[204] M. Azubel, J. Koivisto, S. Malola, D. Bushnell, G.L. Hura, a. L. Koh, et al., Electron microscopy of gold nanoparticles at atomic resolution, Science. 345 (2014) 909–912.

[205] P.D. Jadzinsky, G. Calero, C.J. Ackerson, D.A. Bushnell, R.D. Kornberg, Structure of a thiol monolayer-protected gold nanoparticle at 1.1 A resolution., Science. 318 (2007) 430–433.

[206] I.G. Hill, A. Kahn, J. Cornil, D. a. dos Santos, J.L. Brédas, Occupied and unoccupied electronic levels in organic π-conjugated molecules: comparison between experiment and theory, Chem. Phys. Lett. 317 (2000) 444–450.

[207] T. Matsushima, Y. Kinoshita, H. Murata, Formation of Ohmic hole injection by inserting an ultrathin layer of molybdenum trioxide between indium tin oxide and organic hole-transporting layers, Appl. Phys. Lett. 91 (2007) 253504.

[208] H. Lee, S.W. Cho, K. Han, P.E. Jeon, C.-N. Whang, K. Jeong, et al., The origin of the hole injection improvements at indium tin oxide/molybdenum trioxide/N,N[sup ']-bis(1-naphthyl)-N,N[sup ']-diphenyl-1,1[sup ']-biphenyl-4,4[sup ']-diamine interfaces, Appl. Phys. Lett. 93 (2008) 043308.

[209] S.L.M. van Mensfoort, V. Shabro, R.J. de Vries, R. a. J. Janssen, R. Coehoorn, Hole transport in the organic small molecule material α-NPD: evidence for the presence of correlated disorder, J. Appl. Phys. 107 (2010) 113710.

[210] G. Ligorio, M.V. Nardi, C. Christodoulou, I. Florea, N.-C. Monteiro, O. Ersen, et al., Charging and exciton-mediated decharging of metal nanoparticles in organic semiconductor matrices, Appl. Phys. Lett. 104 (2014) 163302.

[211] G. Horowitz, M.E. Hajlaoui, Mobility in Polycrystalline Oligothiophene Field-Effect Transistors Dependent on Grain Size, Adv. Mater. 12 (2000) 1046–1050.

[212] J. Billen, S. Steudel, R. Müller, J. Genoe, P. Heremans, A comprehensive model for bipolar electrical switching of CuTCNQ memories, Appl. Phys. Lett. 91 (2007) 263507.

[213] D. Ielmini, R. Bruchhaus, R. Waser, Thermochemical resistive switching: materials, mechanisms, and scaling projections, Phase Transitions. 84 (2011) 570–602.

[214] Z.S. Wang, F. Zeng, J. Yang, C. Chen, Y.C. Yang, F. Pan, Reproducible and controllable organic resistive memory based on Al/poly(3,4-ethylene-dioxythiophene):poly(styrenesulfonate)/Al structure, Appl. Phys. Lett. 97 (2010) 253301.

[215] X. Tian, L. Wang, J. Wei, S. Yang, W. Wang, Z. Xu, et al., Filament growth dynamics in solid electrolyte-based resistive memories revealed by in situ TEM, Nano Res. 7 (2014) 1065–1072.

[216] Y. Yang, P. Gao, S. Gaba, T. Chang, X. Pan, W. Lu, Observation of conducting filament growth in nanoscale resistive memories, Nat. Commun. 3 (2012) 732.

[217] S. Gao, C. Song, C. Chen, F. Zeng, F. Pan, Formation process of conducting filament in planar organic resistive memory, Appl. Phys. Lett. 102 (2013) 141606.

[218] L.D. Bozano, B.W. Kean, M. Beinhoff, K.R. Carter, P.M. Rice, J.C. Scott, Organic Materials and Thin-Film Structures for Cross-Point Memory Cells Based on Trapping in Metallic Nanoparticles, Adv. Funct. Mater. 15 (2005) 1933–1939.

[219] W.L. Kwan, B. Lei, Y. Shao, S. V. Prikhodko, N. Bodzin, Y. Yang, Direct observation of localized conduction pathways in photocross-linkable polymer memory, J. Appl. Phys. 105 (2009) 124516.

[220] F. Santoni, A. Gagliardi, M. Auf, D. Maur, A. Pecchia, S. Sax, et al., Modeling of filamentary conduction in organic thin film memories and comparison with experimental data, Org. Electron. (n.d.).

[221] X. Xia, X. Liu, M. Yi, Q. Fan, L. Wang, Q. Tai, et al., Enhancing nonvolatile write-once-read-many-times memory effects with SiO 2 nanoparticles sandwiched by poly(N -vinylcarbazole) layers, J. Phys. D. Appl. Phys. 45 (2012) 215101.

[222] M.J. Brett, M.M. Hawkeye, Materials science. New materials at a glance., Science. 319 (2008) 1192–3.

[223] Y. Zhou, T. Taima, T. Miyadera, T. Yamanari, M. Kitamura, K. Nakatsu, et al., Glancing Angle Deposition of Copper Iodide Nanocrystals for, (2012).

[224] M.M. Hawkeye, M.J. Brett, Glancing angle deposition: Fabrication, properties, and applications of micro- and nanostructured thin films, J. Vac. Sci. Technol. A Vacuum, Surfaces, Film. 25 (2007) 1317.

[225] M. Backholm, M. Foss, K. Nordlund, Roughness of glancing angle deposited titanium thin films: an experimental and computational study, Nanotechnology. 23 (2012) 385708.

[226] Z.M. Liao, C. Hou, H.Z. Zhang, D.S. Wang, D.P. Yu, Evolution of resistive switching over bias duration of single Ag 2 S nanowires, Appl. Phys. Lett. 96 (2010) 94–97.

[227] S.H. Jo, K.H. Kim, W. Lu, Programmable resistance switching in nanoscale two-terminal devices, Nano Lett. 9 (2009) 496–500.

[228] M. Zobeiri, N.G. Jahroudi, HVD Holographic Technology for Data Storage Disks, Int. J. Eng. Res. Dev. 10 (2014) 80–83.